University of Southampton

Faculty of Physical Science and Engineering

Zepler Institute for Photonics and Nanoelectronics

Optoelectronics Research Centre

Compact femtosecond chirped pulse amplification system based on thulium doped fibre

by

Zhengqi Ren

Thesis for the degree of Doctor of Philosophy

April 2021

University of Southampton

Abstract

Faculty of Physical Sciences and Engineering

Zepler Institute for Photonics and Nanoelectronics

Optoelectronics Research Centre

Thesis for the degree of Doctor of Philosophy

Compact femtosecond chirped pulse amplification system based on thulium doped fibre

by

Zhengqi Ren

High power and high energy ultra-short-pulse fibre lasers at 2 μm are an attractive option for use in many applications including free space optical communications, sensing, material processing and mid-IR generation. High energy applications in the 2 μm range in particular, such as for high harmonic generation and laser-driven electrons acceleration, would benefit from repetition-rate scaling. In this thesis, I focus on developing systems with conventional, flexible, fibre technology as this is an important research target that will have immediate practical application, including in material processing, precision surgery and mid-IR light generation. This thesis describes a systematic study of the development of 2 μm thulium-doped fibre laser systems based on chirped pulse amplification (CPA). It includes the development of the seed source, and the exploration of two types of amplification chains for germanate and silica thulium-doped-fibre, as these greatly increase their output power, compactness and potential for practical applications.

A carbon nanotube (CNT) based dissipative soliton mode-locked fibre laser which emitted a central wavelength of around 1960 nm with a bandwidth of 18 nm was created. Unfortunately, after a prolonged operation, the CNT deteriorated to the point that it could no longer produce a stable mode-lock pulse. To replace this damaged carbon nanotube, an artificial saturable

absorber based on a nonlinear polarisation rotation mechanism was used. A conventional soliton which pulsed at 1942 nm and had a spectrum that consisted of strong Kelly sidebands was also achieved, but it was deemed unsuitable as a seed for the intended CPA system. In addition, it was difficult for the dispersion fibre managed cavity to achieve mode-locking through nonlinear polarisation rotation. A commercial SESAM was then used but the oscillator generated constant noise-like pulses lasting a nanosecond each. These were not suitable to seed a CPA system and I were therefore forced to explore alternative solutions. Finally, using a new SESAM, a dissipative soliton mode-locked fibre laser at 1925 nm was investigated. The oscillator could generate self-started mode-locked pulses at a pulse energy of 2.5 nJ with a bandwidth of 40 nm at a 15.6 MHz repetition rate. Furthermore, the chirped pulses with a duration of 25 ps were able to be compressed to 240 fs. In summary, this mode-locked fibre laser was an ideal seed source and qualified for amplification in a future CPA system.

In the CPA part, both commercial silica and in-house fabricated germanate thulium doped fibre (TDF) were investigated for both the cladding and the core pumping scheme. For the TDF silica version, cladding pumping a 1.5 m TDF produced 297 fs compressed pulses with an average power of 21.5 W and a peak power of 4.2 MW. Core pumping a 29 cm TDF meanwhile, produced 285 fs pulses with an average power of 2.8 W and a peak power of 20 MW at a repetition rate of 0.39 MHz. Shortening the fibre length and increasing the mode area are two common methods to minimise the nonlinearity accumulation in the gain fibre. However, for simple fibres, the TDF silica used in the amplifier had the largest mode area and a higher doping concentration than commercial silica. Therefore, there was not enough room to scale pulse peak power for these types of fibres.

To overcome this limitation, two versions of the high doping TDF were developed, both of which were able to shorten the fibre length. The first investigation was the 1st generation of the thulium doped germanate fibre (TDGF1) with a lower doping concentration (3×10^{20} ions/cm^3). Cladding pumping of a 65 cm length of TDGF1 produced pulses with an average power of 14.1 W and a peak power of 2.55 MW. Core pumping a 19 cm TDGF1 meanwhile, produced pulses with an average power of 2.3 W and a peak power of 17 MW at the output of the CPA system. In terms of peak/average power, the TDGF1 version had comparable results with the silica fibre version. To achieve higher pulse energy/peak power therefore, the 2nd generation thulium doped germanate fibre (TDGF2) with a higher doping (8.5×10^{20} ions/cm^3) was developed to shorten the amplifier length. Core pumping of a 9.5 cm length of TDGF produced

pulses with an average power of 1.9 W and a peak power of 42 MW, which, in terms of peak power, beat the silica fibre's results. This confirms that the highly doped Tm^{3+} germanate glass single mode fibre can work as an alternative to silica-based fibre for the generation of 2 μm high energy/peak power pulses.

This thesis is not just limited to the generation of 2 μm high energy/peak power pulses through thulium doped fibre master oscillator power amplifier (MOPA) systems. In the final part, it also covers an exploration for an interesting oscillator with ultra-high energy/peak power output pulses in the germanate fibre oscillators.

Table of Contents

List of Figures

List of Tables

Research Thesis: Declaration of Authorship

Print name: Zhengqi Ren

Title of thesis: Compact femtosecond chirped pulse amplification system based on thulium doped fibre

I declare that this thesis and the work presented in it are my own and has been generated by me as the result of my own original research.

I confirm that:

1. This work was done wholly or mainly while in candidature for a research degree at this University;
2. Where any part of this thesis has previously been submitted for a degree or any other qualification at this University or any other institution, this has been clearly stated;
3. Where I have consulted the published work of others, this is always clearly attributed;
4. Where I have quoted from the work of others, the source is always given. With the exception of such quotations, this thesis is entirely my own work;
5. I have acknowledged all main sources of help;
6. Where the thesis is based on work done by myself jointly with others, I have made clear exactly what was done by others and what I have contributed myself;
7. Parts of this work have been published as the journal and conference publications listed in Appendix A.

Signature: ..... Date: 28/04/2021

Acknowledgements

For the completion of my PhD thesis, first and foremost, I would like to thank my supervisors, Prof. David J. Richardson and Dr. Shaif-ul Alam for their insightful guidance and kind support at all stages of my Ph.D. I learned how to become a scientific researcher from their profound knowledge and serious attitude. And this thesis would not have been possible without their consistent and illuminating instruction.

I would also like to express my heartfelt gratitude to all my colleagues at Optoelectronics Research Centre (ORC) and many other technicians who have generously provided help and time for my research in the past four years. Their direct and indirect help has benefited me a lot.

Special thanks should go to my friends and my family members for their loving considerations and great confidence in me all through these years. They always share my highs and lows. I feel much grateful and heartily owe my achievement to them.

Finally, I would like to acknowledge the support of the University of Southampton, United Kingdom and the China Scholarship Council, China. My heartfelt thanks for a giving me the chance to read for a PhD and supporting me throughout this project.

List of Abbreviations

ABS	acrylonitrile butadiene styrene
AC	autocorrelator
AR	anti-reflection
ASE	amplified spontaneous emission
CFBG	chirped fibre Bragg gratings
CIR	circulator
CMC	carboxymetyl cellulose
CNT	Carbon nanotube
CPA	chirped pulse amplification
CVBG	chirped volume Bragg gratings
CW	continuous wave
DCF	dispersion compensation fibre
DM	dichroic mirror
DS	dissipative soliton
EDFL	erbium doped fibre laser
FBG	fibre bragg grating
FFT	fast Fourier transform
FWHM	full width at half maximum
GVD	group velocity dispersion
HR	high reflection
HWP	half-wave plate
ISO	isolator
LD	laser diode

LMA	large-mode-area
MFA	mode field adapter
MFD	mode-field diameter
MI	modulation instability
ML	mode-locked
Mid-IR	mid-infrared
MO	Mamyshev oscillator
MOPA	master oscillator power amplifier
MQW	multiple quantum well
NDF	normal dispersion fibre
NLP	noise-like pulse
NLSE	nonlinear Schrödinger equation
NPE	nonlinear polarization evolution
NPR	nonlinear polarization rotation
OC	output coupler
OSNR	output signal to noise ratio
PBS	polarising beam splitter
PC	polycarbonate
PC	polarisation controller
PM	polarisation maintaining
PMMA	polymethylmethacrylate
PPKTP	periodically poled $KTiOPO_4$
PPKTA	periodically poled $KTiOAsO_4$
PPLN	periodically poled lithium niobate
QCL	quantum cascade laser

QWP	quarter-wave plate
RF	radio-frequency
SAs	saturable absorbers
SAM	saturable absorber mirror
SC	supercontinuum
SESAM	semiconductor saturable absorber mirrors
SMF	single mode fibre
SHG	second harmonic generation
SPM	self-phase modulation
SWNT	single-walled nanotubes
TBP	time bandwidth product
TDF	thulium-doped fibre
TDFA	thulium-doped fibre amplifier
TDGF	thulium doped germanate fibre
TDSF	thulium doped silica fibre
WDM	wavelength-division multiplexer

Chapter 1

Introduction

1.1 The topic area

1.1.1 Thulium doped fibre ultrafast pulses sources

The first ultrafast pulse fibre laser was demonstrated in 1990 [1]. Since then, ultrafast pulse fibre lasers have been subject to intensive studies working in various configurations and with different fibre types. Numerous mode-locking techniques have been developed and the generation of an ultrafast pulse has been achieved in a wide range of wavelength bands. Recently, fibre lasers that generate near 2 μm have attracted a great deal of attention due to the range of possible applications they offer. The emission spectrum of thulium-doped silica fibre extends from 1650 nm to 2150 nm, thereby providing nearly 500 nm of gain bandwidth, which is suitable for the generation of a few cycle pulses directly from the oscillator.

The CPA, invented by Strickland and Mourou, has been the most well-known and most reliable amplification technique used to generate high energy from a high peak power laser since 1985 [2]. It enabled the generation of pulses with petawatt (10^{15} W) peak power by using a Nova laser system at Lawrence Livermore National Laboratory which was based on the 1999 Ti:sapphire amplifier system [3]. CPA systems based on fibre amplifiers offer a high average power and excellent beam quality which benefit from the high gain and superior thermal handling capability of the fibre technology. In recent years, thulium-doped fibre-based CPA systems with around 2 μm wavebands have been rapidly developed to take advantage of the increasing mode area of fibre. In 2014, a CPA system with an average power of 152 W after pulse compression was created using a 3 m long, thulium-doped photonic crystal fibre (PCF) with a 35 μm mode field diameter (MFD) working as the power amplifier [4]. The system delivered 690 fs pulses with 31 μJ pulse energy with 4 MW peak power at a 49.1 MHz repetition rate (RPR). In the same year, a CPA system with higher pulse energy and peak power was also demonstrated using thulium-doped large-pitch fibre

with a larger MFD of 65 μm in the power amplifier [5]. This system produced 600 fs pulses with 120 μJ pulse energy, yielding a peak power of 200 MW at a RPR of 200 kHz. In 2016, a record peak power of 2 GW was demonstrated through a 1.15 m long thulium-doped PCF with an ultra large core diameter of 80 μm [6]. The compressed pulse had a duration of 200 fs and a pulse energy of 470 μJ but a relatively lower average power of 28.7 W due to its RPR of only 60 kHz. In terms of high average power, the record generation of pulses was a generation in in 2018 of 1060 W average power from a 6 m thulium-doped PCF with a core diameter of 50 μm [7]. After compression, the 13.2 μJ pulse energy with a pulse duration of 265 fs at an 80 MHz pulse repetition rate resulted in a peak power of 50 MW. In 2020, a CPA system based on a thulium-doped PCF (80 μm core diameter) produced pulses with an average power of more than 100 W. The GW-level peak power was also presented [8], yielding an average output power of 108 W at a repetition rate of 417 kHz with a pulse duration of 250 fs and a pulse peak power of 0.73 GW.

The state of the art high average/peak power thulium-doped fibre-based CPA systems mentioned above have rods fibres in the main amplifier. The usage of bulk optics however necessitates free-space propagation and alignment, which sacrifices the compactness and stability of the fibre laser systems, especially when used for industrial applications. The key developed compact thulium-doped fibre CPA systems are summarised in Table 1.1 and are based on the conventional thulium-doped fibre and those components that were broken down into fibres and used from 2013 to 2020. The first demonstration of peak powers from a thulium-doped fibre laser system that exceeded 1 MW was realised in 2013 [9]. The system was seeded with pulses of 150 fs in a Raman-soliton self-frequency shift amplifier, then stretched to ~160 ps using a chirped fibre Bragg grating and it was able to produce 300 fs pulses with 1 μJ energy at peak powers of 3 MW. Then, a dissipative mode-locked pulse was amplified to an average power of 7 W with an energy of 161 nJ and a pulse-width of 121 fs under a simple two amplifier stage. However, the related low pulse energy of the seed and the small mode field area of the fibre in the power amplifier limited the power and energy scaling [10]. By inserting a pulse-picker to reduce the RPR to 100 kHz, the pulse energy was scaled to 10.4 μJ with 11 MW peak power and a pulse-width of 530 fs while, due to RPR, the average power was limited to 1 W [14]. In 2020, a report on the generation of 16.4 MW and 2.8 ps pulses at a repetition rate of 100 kHz from a compact thulium-based fibre CPA system was demonstrated. The system utilised two chirped fibre Bragg gratings (CFBGs)

stretched seeded pulses to 1.8 ns and two chirped volume Bragg gratings (CVBGs) with four passes as the compressor. Despite experiencing high losses inside the system due to the CVBG's large amount of components and multi-passes, this was the highest output pulse energy recorded from a CVBG-based compressor at 2 μm wavelength [15].

Table. 1.1. A summary of compact thulium-doped fibre CPA systems from 2013-2020.

Reference and year	Amplifier stages	Stretched Pulse-width	Compressed Pulse-width	Average Power	Pulse Energy	Peak Power
[9], 2013	3	160 ps	300 fs	0.1 W	1 μJ	1.9 MW
[10], 2016	2	72 ps	121 fs	4.7 W	0.16 nJ	1.3 MW
[11], 2016	3	220 ps	900 fs	0.64 W	0.42 μJ	0.2 MW
[12], 2016	3	180 ps	241 fs	35.4 W	1 μJ	3 MW
[13], 2017	4	550 ps	2 ps	1.9 W	10.3 μJ	5.1 MW
[14], 2019	3	600 ps	530 fs	1 W	10.4 μJ	11 MW
[15], 2020	3	1.8 ns	2.8 ps	25 W	46 μJ	16.4 MW

1.1.2 Applications of the 2 μm ultra-fast pulses

2 μm lasers are potential candidates for use in high-precision surgery. Their most important characteristic is high absorption in water combined with minimal penetration depth for both soft and hard human tissues. The superficial mid-infrared tissue ablation effects that come from this, lead to submicron ablation rates which result in minimal damage around the exposed area. The coagulation effect with the 2 μm laser radiation is another significant aspect, which suppress bleeding during operations. Additionally, a femtosecond laser can achieve precision that is 2–3 times better than cell surgery using continuous wave (CW) irradiation, as well as being able to enable manipulation at arbitrary locations [16]. The femtosecond laser has been used in ocular surgeries, such as in corneal refractive surgery, due to its ultrafast pulses and decreased energy requirements for tissue destruction, which allow for a reduction in the unintended destruction of surrounding tissues [17-19]. Therefore, developing compact 2 μm femtosecond pulses is an attractive prospect in the area of bio-tissues and cells surgery.

Plastic is transparent in the visible wavelength range and has sufficient absorption, around 2 μm, to allow direct processing with relevant lasers working at a 2 μm wavelength range. For example, Fig.1.1 shows spectra for four different transparent plastics including cyclic olefin copolymer (COC), polycarbonate (PC), polymethylmethacrylate (PMMA) and acrylonitrile butadiene styrene (ABS). There are two obvious absorption peaks - around 1700 nm and 2150 nm [20].

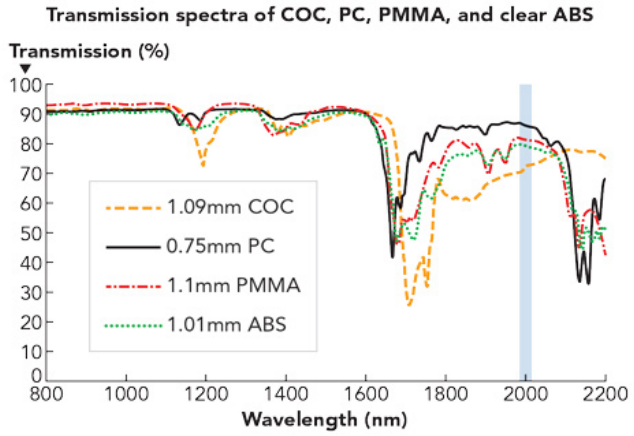

Fig. 1.1 Transmission spectra of four different transparent plastic samples [6]

Selective laser-induced etching (SLE) is a recently-developed approach that uses ultrashort laser pulses to locally modify the glass material in the laser focus and allows to inscribe complex 3D structures. This approach was successfully applied to process fused silica glass and to produce for precise 3D structures using femtosecond pulses at 1030 nm [21]. However, other glasses like borosilicate glass could not be machined using this waveband. Sotier et.al have demonstrated that SLE using 2 μm pulses with 540 fs duration is a promising tool to manufacture hollow 3D microstructures into borosilicate glass and fused silica [22]. Therefore, high power femtosecond lasers at 2 μm have the potential to process materials which are opaque in the visible spectral range but optically transparent at wavelengths of 2 μm.

Coherent mid-infrared supercontinuum (SC) light sources are an attractive option for use in many applications including optical coherence tomography, frequency metrology, nonlinear microscopy, molecular spectroscopy and non-destructive testing [23-27]. For the pump light, pulses with femtosecond pulse-width are preferable as they create coherent SC light sources [28,29]. Light sources at 2 μm range are able to obtain higher efficiency mid-infrared

supercontinuum generation than 1 μm and 1.5 μm sources. This is due to the lower propagation loss and the 2 μm wavelength is closer to zero dispersion in nonlinear soft glass fibres, including in fluoride fibres and chalcogenide fibres [30]. Therefore, these femtosecond sources at 2 μm range can work as a pump source for coherence SC generation in the mid-IR.

1.2 Motivations

Driven by many applications in surgery, plastic material processing and frequency conversion into the mid-infrared region, it is interesting to develop 2 μm high average/peak pulses sources. Thulium doped fibre MOPA systems can be a good candidate as such high power ultra-fast source operating in the 2 μm wavelength range. My target is to explore the thulium doped fibre CPA system combined with characteristics of compactness, robustness, good beam quality, stability, which can generate high average/peak power pulses.

The seed source plays one of the most significant roles in the whole CPA system, which can determine the system's compactness, stability, robustness, beam quality, stretched/compressed pulse-width, final power scaling. I investigate pulses characteristics of the thulium-doped fibre oscillators based on different mode-locking mechanisms and pulses shape strategies. Eventually, I choose a SESAM as the saturable absorber in the oscillator with generation of dissipative soliton pulses, which can satisfy the requirements of high compactness, stability, robustness, large stretched pulse-width ratio, narrow compressed pulse-width for the CPA system.

I then investigate the power amplification of the seed pulses in a commercially available 25-μm-core LMA thulium doped fibre, instead of using rod-type thulium doped PCFs with larger core size to avoid increasing systematic complexity and instability. The power amplification of my high-power CPA systems has two separate schemes including cladding pumping and core pumping. The cladding pump scheme is able to generate pulses with high average power owing to diodes technologies development and better temperature management. On the other hand, the core pumping scheme has much shorter length of the amplifier provides larger nonlinearity threshold can generate pulses with higher peak power.

To overcome the limitation of the commercially available largest core size of the thulium doped fibre mentioned above in the power amplifier in order to pursue pulses with higher

energy/peak power. I explore the development of the germanete fibre with higher thulium ions doping concentration to short the power amplifier further, which helps to decrease the nonlinearity so as to produce pulses with higher peak power. The first generation of thulium doped germanate fibre base system provides comparable results with commercially available largest core size silica fibre. Furthermore, the CPA system's results based on second generation of the fibre beat the commercial fibre one in terms of pulse energy and peak power.

In general, I develop the high average/peak power thulium doped fibre CPA system with characteristics of compactness, robustness, stability.

1.3 Thesis outline and novelty

This thesis is composed of 7 chapters.

Chapter 1 discusses the research motivation behind my PhD project, as well as the structure of the thesis itself.

Chapter 2 provides the background for thesis. Topics include the fundamentals of fibre lasers and amplifiers, numerical theory of pulses propagation in fibre, mode-locked fibre laser theory, thulium-doped fibre, and pulse stretchers and compressors.

Chapters 3-5 present the experimental work involved in the development of the 2 μm CPA system. Chapter 3 presents the investigation of an ideal seed sources for the following CPA chain, which would be very important to obtain high peak power for the CPA output pulses. Chapter 4 presents the most compact and practical CPA system with high output average/peak power and pulse energy based on conventional simple silica thulium doped fibre in literature. Chapter 5 presents a first CPA system by using a simple germanate thulium doped fibre, which had higher peak power and pulse energy compared with conventional silica material fibre.

Chapter 3 describes a CNT saturable absorber based dissipative soliton mode-locked fibre laser that has a range of around 1960 nm with a bandwidth of 18.6 nm and a pre-chirped pulse-width of 14.6 ps. Unfortunately, when used over a prolonged operation the CNT deteriorated. Then, a conventional soliton mode-locked fibre laser was demonstrated which pulsed at 1942 nm, had a spectral of strong Kelly sidebands and was based on nonlinear

polarisation rotation, however, it was deemed unsuitable as a seed for the intended CPA system. In addition, when the dispersion management fibre was inserted into the cavity, it became difficult to achieve mode-locking. Following this, a commercial SESAM was used but the oscillator constantly generated noise-like pulses lasting a nanosecond range.

Finally, by using the new SESAM, a dissipative soliton mode-locked fibre laser working at 1925 nm with a bandwidth of 40 nm was realised. The oscillator could generate self-started mode-locked single pulses at a pulse energy of 2.5 nJ and a 3 dB bandwidth of 40 nm at a repetition rate of 15.6 MHz, which was then able to be compressed to 240 fs. In addition, chirped pulses with a duration of 25 ps were beneficial for the reduction of nonlinear accumulations in the following segments of the CPA system. Such a pulse is qualified to be used for amplification in the future CPA system and will be used in chapters 4 and 5.

Chapter 4 demonstrates a high-peak-power, high energy silica thulium-doped fibre CPA system through both the cladding and core pumping schemes. Cladding pumping a 1.5 m thulium doped silica fibre (TDSF) produced 297 fs compressed pulses with an average power of 21.5 W and a peak power of 4.2 MW at a repetition rate of 15.7 MHz. The cladding pumping scheme which used components that had been fully broken down into fibres (except for a compressed grating pair) and just two amplification stages, achieved a highly practical and compact CPA system. Core pumping a 29 cm TDSF produced 285 fs pulses with an average power of 2.8 W and a peak power of 20 MW at a repetition rate of 0.39 MHz. Compared with the cladding pump scheme, in the core pump, a length of fibre that is 5 times shorter leads to a significant improvement in the pulses' peak power, from 4.2 MW to 20 MW (~ 5 times), but sacrifices compactness, cost and repetition rate (average power). These results were published in *Optics Express*.

Chapter 5 depicts a high-peak-power, high energy germanate thulium-doped fibre CPA system through both the 1st generation fibre (3×10^{20} ions/cm^3 doping) and 2nd generation fibre (8.5×10^{20} ions/cm^3 doping) schemes. These two generations of fibres were both investigated for the core and cladding pumping schemes. This was the first demonstration of the CPA system based on thulium doped germanate fibre.

For the 1st generation of TDGF, cladding pumping of a 65 cm length of TDGF produced pulses with an average power of 14.1 W and a peak power of 2.55 MW at the output of the CPA system. Core pumping a 19 cm TDGF produced pulses with an average power of 2.3 W

and a peak power of 17 MW. In terms of peak/average power, the 1st generation TDGF had comparable results with the TDSF based CPA system. Then, with the development of the 2nd generation of higher doping TDGF, the core pumping of a 9.5 cm length of TDGF produced pulses with an average power of 1.9 W and a peak power of 42 MW at the output of the CPA system. The result beat our TDSF based CPA in terms of peak power. Additionally, this was the highest peak power generated from a conventional, simple fibre system. These results were published in *Optics Letter*.

Chapter 6 presents high energy (157 nJ), broad spectral bandwidth (107 nm) pulses around 2 μm from a single cavity-Mamyshev oscillator based on 1st generation of home-fabricated germanate thulium doped fibre. The pulse energy is 40 times higher than the latest results because of the normal dispersion of the gain fibre for self-phase-modulation spectral broadening. Further pulse energy scaling was limited by shortage of the 2 μm coating optics.

Chapter 7 provides a concluding summary for the whole thesis and future work about the nonlinear compression and coherent supercontinuum generation based on previous CPA system.

Reference

[1] D. E. Spence, P. N. Kean, and W. Sibbett, “60-fsec pulse generation from a self mode-locked Ti:sapphire laser,” Opt. Lett. **16**(1), 42–44 (1991).

[2] D. Strickland and G. Mourou, “Compression of amplified chirped optical pulses,” Opt. Commun. **56**(3), 219−221 (1985).

[3] M. D. Perry, D. Pennington, B. C. Stuart, G. Tietbohl, J. A. Britten, C. Brown, S. Herman, B. Golick, M. Kartz, J. Miller, H. T. Powell, M. Vergino, and V. Yanovsky, “Petawatt laser pulse,” Opt. Lett. **24**(3), 160-162(1999).

[4] F. Stutzki, C. Gaida, M. Gebhardt, F. Jansen, A. Wienke, U. Zeitner, F. Fuchs, C. Jauregui, D. Wandt, D. Kracht, J. Limpert, and A. Tünnermann, "152W average power Tm-doped fiber CPA system," Opt. Lett. **39**(16), 4671-4674 (2014).

[5] C. Gaida, F. Stutzki, M. Gebhardt, F. Jansen, C. Jauregui, J. Limpert, and A. Tünnermann, "200 MW peak power from a Tm-doped fiber CPA system," in Advanced Solid State Lasers, OSA Technical Digest (online) (Optical Society of America, 2014), paper ATu5A.2.

[6] C. Gaida, M. Gebhardt, F. Stutzki, C. Jauregui, J. Limpert, and A. Tünnermann, "Thulium-doped fiber chirped-pulse amplification system with 2 GW of peak power," Opt. Lett. **41**(17), 4130-4133 (2016).

[7] C. Gaida, M. Gebhardt, T. Heuermann, F. Stutzki, C. Jauregui, and J. Limpert, "Ultrafast thulium fiber laser system emitting more than 1 kW of average power," Opt. Lett. **43**(23), 5853-5856 (2018).

[8] Z. Wang, T. Heuermann, M. Gebhardt, C. Gaida, C. Jauregui, and J. Limpert "108 W average power ultrashort pulses with GW-level peak power from a Tm-doped fiber CPA system", Proc. SPIE 11260, Fiber Lasers XVII: Technology and Systems, 112600K (21 February 2020)

[9] R. Andrew Sims, P. Kadwani, A. Lawrence Shah, and M. Richardson, "1 uJ, sub-500 fs chirped pulse amplification in a Tm-doped fiber system," Opt. Lett. **38**(2), 121-123 (2013).

[10] Fangzhou Tan, Hongxing Shi, Peng Wang, Jiang Liu, Pu Wang, "Chirped pulse amplification of a dissipative soliton thulium-doped fiber laser," Proc. SPIE 9728, Fiber Lasers XIII: Technology, Systems, and Applications, 97280Y (11 March 2016)

[11] D. Gaponov, L. Lavoute, S. Février, A. Hideur, N. Ducros, "2µm all-fiber dissipative soliton master oscillator power amplifier," Proc. SPIE 9728, Fiber Lasers XIII: Technology, Systems, and Applications, 972834 (11 March 2016);

[12] F. Tan, H. Shi, R. Sun, P. Wang, and P. Wang, "1 µJ, sub-300 fs pulse generation from a compact thulium-doped chirped pulse amplifier seeded by Raman shifted erbium-doped fiber laser," Opt. Express **24**(20), 22461-22468 (2016).

[13] D. Gaponov, L. Lavoute, N. Ducros, A. Hideur and S. Février, "10 µJ-Class compact thulium all-fibered CPA system," 2017 Conference on Lasers and Electro-Optics Europe & European Quantum Electronics Conference (CLEO/Europe-EQEC), Munich, pp. 1-1, (2017).

[14] D. Gaponov, L. Lavoute, N. Ducros, M. Paris, A. Hideur, and S. Février, "Compact thulium FCPA system delivering 11 MW, 530 fs pulses," in 2019 Conference on Lasers and Electro-Optics Europe and European Quantum Electronics Conference, OSA Technical Digest (Optical Society of America, 2019), paper cj_10_5.

[15] E. Lee, B. Sun, J. Luo, S. Singh, D. Choudhury, D. Yong, X. Yu, and Q. Wang, "Compact pulsed thulium-doped fiber laser for topographical patterning of hydrogels," Opto-Electronic Advances **3**, 190039 (2020).

[16] A. Vogel, J. Noack, G. Huttman, and G. Paltauf, “Mechanisms of femtosecond laser nanosurgery of cells and tissues,” Appl. Phys. B **81**, 1015–1047 (2005).

[17] A. Sugar, “Ultrafast (femtosecond) laser refractive surgery,” Curr Opin Ophthalmol. **13**(4), 246 (2002).

[18] H. Limin, K. Sheehy, and W. Culbertson, “Femtosecond laser-assisted cataract surgery,” Curr Opin Ophthalmol. **22**, 43-52 (2011).

[19] M. Moshirfar, D. S. Churgin, and Maylon Hsu, “Femtosecond Laser-Assisted Cataract Surgery: A Current Review,” EUR. J. Ophthalmol. **30**(3), 417-429 (2020).

[20] K. Scholle, S. Lamrini, P. Koopmann, and P. Fuhrberg, “2 μm Laser Sources and Their Possible Applications,” Frontiers in Guided Wave Optics and Optoelectronics, 2010, 674.
[21] J. Gottmann, M. Hermans, N. Repiev, and J. Ortmann, “Selective Laser-Induced Etching of 3D Precision Quartz Glass Components for Microfluidic Applications—Up-Scaling of Complexity and Speed,” Micromachines **8**(4), 110 (2017).
[22] F. Sotiera, W. K. Kipnusub, M. Hermansc, J. Gottmannc, S. Geigera, G. Marowskyd, K. R. Siefermannb, “A novel 2 μm Ultrashort Pulsed Laser Source for Selective Laser-Induced Etching of Glass” Lasers in Manufacturing Conference (2017).
[23] R. Su, M. Kirillin, E. Chang, E. Sergeeva, S. Yun, and L. Mattsson, "Perspectives of mid-infrared optical coherence tomography for inspection and micrometrology of industrial ceramics," Opt. Express **22**(13), 15804-15819 (2014).
[24] A. Schliesser, N. Picqué, and T. W. Hänsch, “Mid-infrared frequency combs,” Nat. Photonics **6**, 440–449 (2012).
[25] F. Cruz, D. Maser, T. Johnson, G. Ycas, A. Klose, F. Giorgetta, I. Coddington, and S. Diddams, "Mid-infrared optical frequency combs based on difference frequency generation for molecular spectroscopy," Opt. Express **23**(20), 26814-26824 (2015).
[26] H. Kano and H.-o. Hamaguchi, “Ultrabroadband (> 2500 cm-1) multiplex coherent anti-Stokes Raman scattering microspectroscopy using a supercontinuum generated from a photonic crystal fiber,” Appl. Phys. Lett. **86**(12), 12113 (2005).
[27] F. K. Tittel, D. Richter, and A. Fried, “Mid-infrared laser applications in spectroscopy,” in Solid-State Mid-Infrared Laser Sources, I.T. Sorokina and K.L. Vodopyanov, ed. (Springer, 2003).
[28] J. Dudley and S. Coen, "Coherence properties of supercontinuum spectra generated in photonic crystal and tapered optical fibers," Opt. Lett. **27**(13), 1180-1182 (2002).
[29] J. M. Dudley and S. Coen, "Supercontinuum generation in photonic crystal fiber," Rev. Mod. Phys. **78**, 1135 (2006).
[30] J. Price, T. M. Monro, H. Ebendorff-Heidepriem, F. Poletti, P. Horak, V. Finazzi, J. Leong, P. Petropoulos, J. C. Flanagan, G. Brambilla, X. Feng, and D. J. Richardson, “Mid-IR supercontinuum generation from nonsilica microstructured optical fibers,” IEEE J. Selected Topics in Quantum Electronics, **13**(3),738-749 (2007).
[31] P. Repgen, B. Schuhbauer, M. Hinkelmann, D. Wandt, A. Wienke, U. Morgner, J. Neumann, and D. Kracht, "Mode-locked pulses from a Thulium-doped fiber Mamyshev oscillator," Opt. Express **28**(9), 13837-13844 (2020).

Chapter 2

Background theory

2.1 Introduction

In this chapter, the background theory that supports the experimental work of this thesis will be introduced. This includes an introduction to fundamental fibre laser and amplifier theory, pulse propagation in fibres, mode-locked fibre lasers, thulium doped fibre and pulse stretchers and compressors.

2.2 Fibre laser and amplifier fundamental theory

2.2.1 Einstein A &B coefficients

In this section I introduce the Einstein A &B coefficients as a way of discussing the basic quantum principles of laser. Einstein coefficients are mathematical quantities which are a measure of the probability of absorption or emission of light by an atom or molecule. The Einstein A coefficients are related to the rate of spontaneous emission of light, and the Einstein B coefficients are related to the absorption and stimulated emission of light.

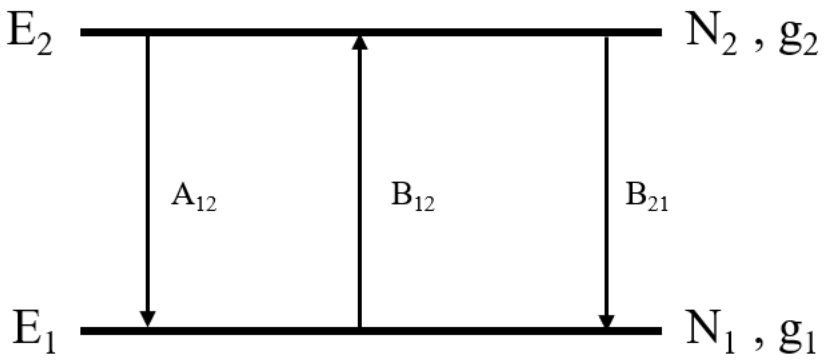

Fig.2.2.1 Two level system diagram

Consider a radiation field and a collection of two-level systems, in thermal equilibrium with each other as shown in Fig. 2.2.1. $N_{2,1}$ and $g_{2,1}$ are populations and degeneracies of the upper energy level (E_2) and lower energy level (E_1) respectively. A_{21}, B_{12} and B_{21} are Einstein's coefficients corresponding to spontaneous emission, absorption, and stimulated emission respectively. Here non-radiative transition between the two energy levels is neglected.

The distribution of atoms across the two energy levels will change depending on the absorption or emission of radiation. Einstein introduced three empirical coefficients to quantify the change of population in the two levels [1].

- **Absorption**: 'B_{12}' is the probability (per unit time) of the absorption of radiation, and it means that the population of the upper-level increases. The rate is clearly proportional to the population of atoms in the lower level and to the energy density 'u(v)' of radiation in the system. The rate of population increases in the excited state is given by:

$$\frac{\mathrm{d}N_2}{\mathrm{d}t} = B_{12}u(\nu)N_1 \qquad (2.1)$$

  Where 'B_{12}' is a constant of proportionality coefficient.

- **Spontaneous Emission:** the population of the upper level will decrease due to a spontaneous transition to the lower level with the emission of radiation. The rate of emission will depend on the population of the upper level. If 'A_{12}' is the probability with which an atom in the excited state will spontaneously decay to the ground state:

$$\frac{\mathrm{d}N_2}{\mathrm{d}t} = -A_{12}N_2 \qquad (2.2)$$

The equation above has the solution:

$$N_2(t) = N_2(0)e^{-\frac{t}{\tau}} \qquad (2.3)$$

where '$\tau=1/A_{12}$' gives the average of an atom in the excited level before the atom returns to the ground state. Therefore, the spontaneous emission depends on the lifetime of the atom

in the excited state. The process is statistical and the emitted quanta bear no phase relationship with one another, i.e., the emission is incoherent.

- **Stimulated Emission:** stimulated emission depends on the number of atoms in the excited level as well as on the energy density of the incident radiation. If 'B_{21}' is the transition probability per unit time per unit energy density of radiation, the rate of decrease of the population of the excited state is '$B_{21}u(v)N_2$'. The rate equation for the population of the upper level is:

$$\frac{dN_2}{dt} = B_{12}u(v)N_1 - [A_{21} + B_{21}u(v)]N_2 \qquad (2.4)$$

Since N_1+N_2 = constant:

$$\frac{\mathrm{d}N_2}{\mathrm{d}t} = -\frac{\mathrm{d}N_1}{\mathrm{d}t} \qquad (2.5)$$

The emitted quanta under the stimulated emission are coherent with the impressed field. The spontaneous emission, being incoherent, is a source of noise in the lasers. When equilibrium is reached, the levels' population remains constant, so that '$dN_2/dt=0$' and the rate of emission equals the rate of absorption, so that:

$$B_{12}u(v)N_1 = [A_{21} + B_{21}u(v)]N_2 \qquad (2.6)$$

Using the Boltzmann factor $'N_2/N_1 = \left(\frac{g_2}{g_1}\right) \exp(-h\nu/kT)'$ and by simplifying, we get:

$$u(v) = \frac{A_{21}\frac{g_2}{g_1}}{B_{12}e^{\frac{h\nu}{kT}} - B_{21}\frac{g_2}{g_1}} = \frac{\frac{A_{21}}{B_{21}}}{\frac{g_1}{g_2}e^{\frac{h\nu}{kT}}\frac{B_{12}}{B_{21}} - 1} \qquad (2.7)$$

If we regard the matter to be a blackbody and then compare the above expression for energy density and the corresponding energy density expression derived for the blackbody radiation with:

$$u(\nu) = \frac{8\pi h\nu^3}{c^3} \frac{1}{e^{\frac{h\nu}{kT}} - 1} \qquad (2.8)$$

We get:

$$\frac{A_{21}}{B_{21}} = \frac{8\pi h\nu^3}{c^3} \qquad (2.9) \qquad and \qquad \frac{B_{21}}{B_{12}} = \frac{g_1}{g_2} \qquad (2.10)$$

The last equation shows that with the absence of degeneracy, the probability of stimulated emission is equal to that of absorption. In view of this, two coefficients was replaced by a single coefficient termed as the – 'B' coefficient. The spontaneous emission coefficient will then be called the – 'A' coefficient. The ratio of spontaneous emission probability to the stimulated emission probability is now:

$$\frac{A}{Bu(\nu)} = e^{h\nu/kT} - 1 \qquad (2.11)$$

So, for low temperatures, when $'h\nu/kT \gg 1'$, spontaneous emission is much more probable than stimulated emission, and the latter may even be ignored. For high enough temperatures, stimulated emission probability can be significant, though for optical frequencies this requires a very high temperature. For microwave frequencies, the stimulated emission processes may be significant even when at room temperature.

2.2.2 Rate equation and population inversion

2.2.2.1 Two-level atomic system

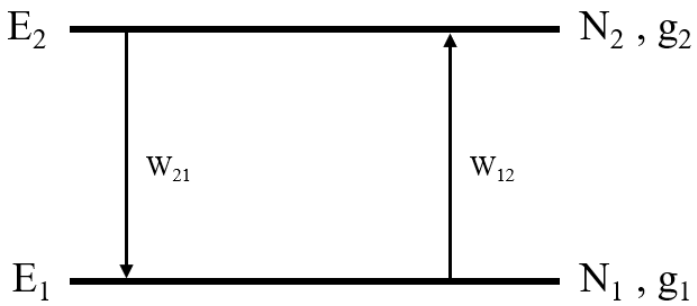

Fig. 2.2.2. Two level atomic system

Let us first examine the two-level atomic system. The pumping process provides the incident radiation that satisfies '$h\nu = E_2 - E_1$, $E_2 > E_1$'. W_{12} is defined as the possibility atoms have of jumping from E_1 to E_2 due to absorption, while W_{21} is defined as the possibility of atoms jumping from E_2 to E_1 because of stimulated emission. Finally, R_{12} and R_{21} are defined as the corresponding relaxation or decay rate (including both spontaneous radiation rate and non-radiation decay rate) [2]. Then, the rate equations for two-level atomic system are:

$$\frac{dN_1(t)}{dt} = -\frac{dN_2(t)}{t} = -[W_{12} + R_{12}]N_1(t) + [W_{21} + R_{21}]N_2(t) \qquad (2.12)$$

$$N_1(t) + N_2(t) = N \qquad (2.13)$$

$$\Delta N = N_1 - N_2 \qquad (2.14)$$

$$W_{12} + W_{21} \equiv 1/T_1 \qquad (2.15)$$

N is the total atom number, so '$\Delta N = N_1 - N_2$' is the population difference. 'T_1' is the population recovery time or energy relaxation time of the system. We also define 'N_{10}' and 'N_{20}' as the atom population at thermal equilibrium and so '$\Delta N_0 = N_{10} - N_{20}$' is the population difference at thermal equilibrium. Note also '$W_{12} = W_{21}$'. After some calculations:

$$\frac{d\Delta N(t)}{dt} = -2W_{12}\Delta N(t) - \frac{[\Delta N(t) - \Delta N_0]}{T1} \qquad (2.16)$$

At a steady state, when 'ΔN' does not change with time, we get:

$$\Delta N = \frac{\Delta N_0}{1 + 2W_{12} * T_1} \qquad (2.17)$$

'ΔN' is bigger than zero, while 'W_{12}' is closely related with the incident signal and the stronger the incident signal, the bigger the 'W_{12}, $W_{12} > 0$'. From the above equation we can see that for a two-level atomic system, the incident signal will make the population difference 'ΔN' approach zero when the signal is big enough, but surprisingly, no population inversion occurs. The best it can do is when at a steady state or at saturation, as the population difference becomes '0'. The conclusion is therefore, that in order to achieve a population inversion, we must use atomic systems with more than two related energy levels.

2.2.2.2 Three-level atomic system

As discussion above two levels system are not sufficient to achieve population inversion. We thus study here for the possibility of population inversion in the three level systems in this sub-section.

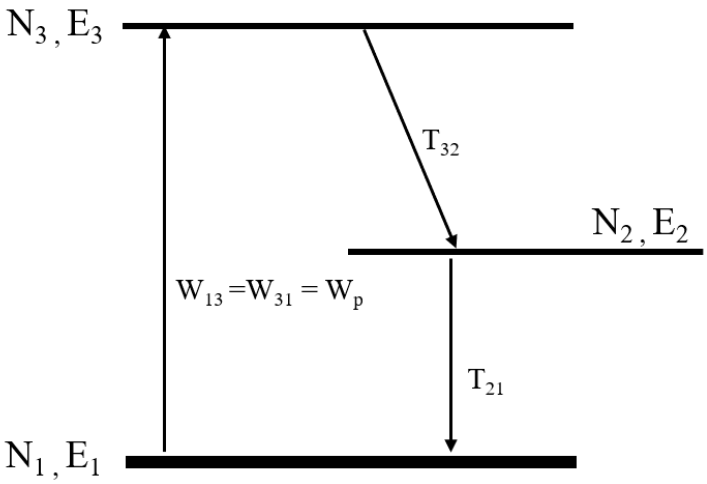

Fig. 2.2.3. Three level laser system

For the three-level laser system, 'E_1' is the ground state, and lasing is between 'E_2' and 'E_1'. Supposing the pumping process produces a stimulated transition probability between 'E_1' and 'E_3', then '$W_{13}=W_{31}=W_p$'. Atoms at 'E_3' have a fast decay time, shown as 'T_{32}', i.e., atoms at 'E_3' decay to 'E_2' in a very short time frame (T_{32}). Atoms at 'E_2' have a relatively slow transition time, shown as 'T_{21}', i.e., atoms at 'E_2' will take a longer time to change to 'E_1' than the atoms changing from 'E_3' to 'E_2'. In addition, as we have '$N=N_1+N_2+N_3$', we have rate equations for three level laser systems:

$$\frac{dN_3}{dt} = W_p(N_1 - N_3) - \frac{N_3}{T_{32}} \qquad (2.18)$$

$$\frac{dN_2}{dt} = \frac{N_3}{T_{32}} - \frac{N_2}{T_{21}} \qquad (2.19)$$

$$N = N_1 + N_2 + N_3 \qquad (2.20)$$

$$\beta \equiv \frac{N_3}{N_2} = \frac{T_{32}}{T_{21}} \qquad (2.21)$$

At a steady state, the population difference between E_2 and E_1 is:

$$\frac{N_2 - N_1}{N} = \frac{(1-\beta)W_p T_{21} - 1}{(1+2\beta)W_p T_{21} + 1} \qquad (2.22)$$

From the above, we can see that in order for population inversion to occur, i.e., for 'N_2-N_1>0', the pumping rate, shown as 'W_p', must satisfy: 'W_p*T_{21}>1/(1-b)'. If we assume the atoms at 'E_3' immediately decay to 'E_2', then 'β =0', which means that at a steady state, we have:

$$\frac{N_2 - N_1}{N} \approx \frac{W_p T_{21} - 1}{W_p T_{21} + 1} \qquad (2.23)$$

We can conclude that the population inversion is possible for a three level atomic system under the condition of $T_{32} << T_{21}$ and the pumping rate must be bigger than a positive threshold value. Because N_1 is the ground level, N_1 is always very big in the beginning. Population inversion starts after half of the ground level atoms being pumped to the E_2 level hence the three-level laser system is not very efficient.

2.2.2.3 Four-level atomic system

Now we discuss what advantages the four-level laser systems have over three-level systems above. The Fig. 2.2.4 below shows the four level laser model.

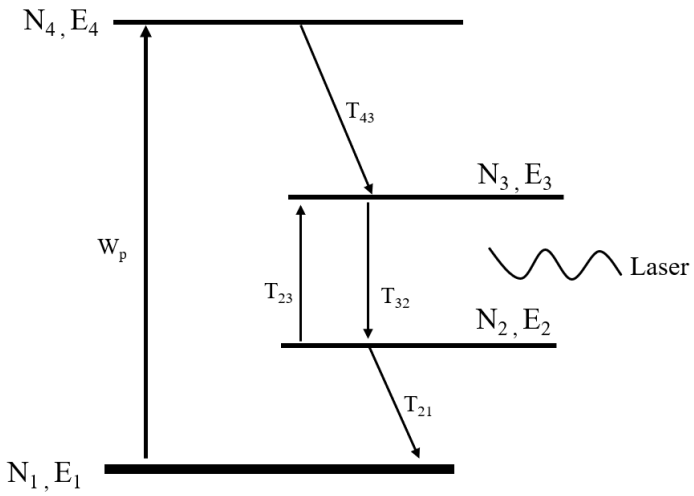

Fig. 2.2.4. Four level laser system

Assume E_1, N_1 at the ground level, pumping process raise the atoms from E_1 to E_4 with pumping rate of W_p. Atoms at E_4 have fast decay to E_3, decay time is T_{43}. Lasing happens between E_3 and E_2, the transmission time is T_{32}. Atoms at E_2 then decay very fast to E_1, the decay time is T_{21}. Assume the total atoms: $N=N_1+N_2+N_3+N_4$, then we have rate equations for four-level laser systems:

$$\frac{dN_4}{dt} = W_p(N_1 - N_4) - \frac{N_4}{T_{43}} \qquad (2.24)$$

$$\frac{dN_3}{dt} = \frac{N_4}{T_{32}} - \frac{N_3}{T_{32}} \qquad (2.25)$$

$$\frac{dN_2}{dt} = \frac{N_3}{T_{32}} - \frac{N_2}{T_{21}} \qquad (2.26)$$

$$\beta \equiv \frac{N_2}{N_3} = \frac{T_{21}}{T_{32}} \qquad (2.27)$$

For simplification, we assume T_{43} is short enough that the pumped atoms to E_4 immediately decay to E_3, N_4 is nearly 0. Also atoms at E_2 decay so fast that we can say N_2 is nearly zero. We examine population inversion between N_3 and N_2 here:

$$\frac{N_3 - N_2}{N} = \frac{(1-\beta)W_p T_{32}}{(1+\beta)W_p T_{32} + 1} \qquad (2.28)$$

Since $\beta \approx 0$ for a four-level system, N_3-N_2 is readily bigger than zero. There is almost no threshold for W_p to generate population conversion. Fig.2.2.5 shows a plot of the population inversion on the four and three level laser transition versus the normallized pumping rare. The advantage of four-level laser system is very clear which has much lower threshold compared with three-level laser system.

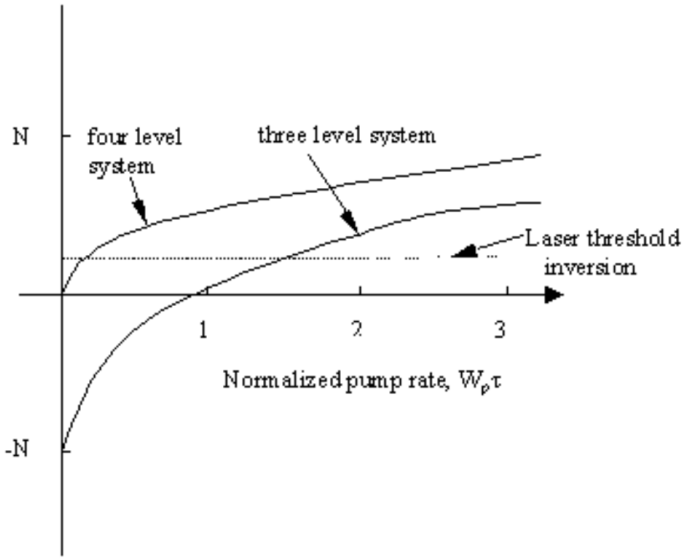

Fig. 2.2.5. Laser population inversion versus normalized pumping rate for idealized four-level and three-level laser systems [4].

Up to now I have discussed population inversion conditions by analyzing the pumping rate equations. I make some simplifications to make the material easily understood. The actual detailed rate equations are far more complex than we see here, I suggest the interested readers refer books on principles of lasers for [5].

2.2.3 Gain saturation and amplifier gain

Clearly, gain cannot continue indefinitely. For each photon added to the field, one atom is removed from the upper laser level and one is added to the lower level. Hence, population inversion reduces, which in turn, reduces gain. There is a competition between the pumping and stimulated emission rate. Pumping builds up the population of the upper level until the threshold is reached and the stimulated emission starts. Assume 'S' is a simple rate equation for the population of the upper level. Let it be the number density of photons per unit time. In a gain medium '$S = S_0 e^{\int g dx}$'. The population of the upper level is given by [3]:

$$\frac{dN_u}{dt} = R_u - \frac{N_u}{\tau} - \sigma N_u S(A) \qquad (2.24)$$

Where 'R_u' is the pumping rate to the upper level, 'τ' is the natural lifetime of the excited atoms and 'σ' is the gain cross section. In the absence of a stimulated emission, the population in the steady state is given by:

$$N_u^0 = R_u \tau \qquad (2.25)$$

The population reaches the steady state in an exponential fashion:

$$N_u(t) = R_u \tau \left(1 - e^{-\frac{t}{\tau}}\right) \qquad (2.26)$$

In the presence of light, the steady state solution to equation (A) is obtained by equating the right-hand side of (A) to zero. The steady state population of the upper level is given by:

$$N_u = \frac{N_u^0}{1 + \sigma \tau S} \quad (2.27)$$

We may rewrite the above as:

$$N_u = \frac{N_u^0}{1 + S/S_{\text{sat}}} \equiv \frac{N_u^0}{1 + \frac{I}{I_{\text{sat}}}} \qquad (2.28)$$

where 'I_{sat}' is the saturation intensity, which is equal to the intensity with which the gain is reduced by a factor of 2.

When dealing with three-energy-level systems or quasi-three-energy-level systems (as in the case of most widely used fibre lasers, such as (Yb^{3+}, Er^{3+} and Tm^{3+}) one needs to take into account the reabsorption losses of laser radiation at the oscillation wavelength. This section provides a detailed description of the gains and losses in fibre amplifiers. First, consider the critical pump power required to achieve a gain coefficient of zero at a particular point in the fibre. This is given by [4]:

$$P_{\text{pcr}} = A h v_p \frac{1}{\tau} \frac{\sigma_{\text{al}}}{\left(\sigma_{\text{el}} \sigma_{\text{ap}} - \sigma_{\text{ep}} \sigma_{\text{al}}\right)} \qquad (2.29)$$

where 'A' is the core area cross-section, 'h' is the Planck's constant, 'υ_p' is the pump laser frequency, 'τ' is the upper-level lifetime, 'σ' is the cross-section of the quantum transition, and 'e', 'a', 'p', and 'l' respectively denote the emission, absorption, pump, and laser wavelengths (i.e., rap stands for the absorption cross-section at the pumping wavelength).

This analysis assumes that the only loss mechanism in the fibre doped with laser-active ions is related to the absorption transition of the laser-active centre, and that any other sources of loss-like scattering are absent. However, modern optical fibres demonstrate measurable scattering loss. Typical loss in fibres, especially those used for telecommunication applications (i.e., undoped), are on the order of 0.2 dB/km for doped fibres, and depending on the wavelength of the laser operation and the gain fibre under consideration, the loss can vary from 0.01–0.1 dB/m. The pump saturation power of the optical centre's absorption transition can be expressed as:

$$P_s = \frac{h\nu_p A}{(\sigma_{\text{ep}} + \sigma_{\text{ap}})\tau\phi_p} \qquad (2.30)$$

where 'ϕ_p' is the pumping quantum efficiency. The small-signal (unsaturated) gain for the whole length of the fibre amplifier is given by:

$$G_0 = g_0 L = \frac{\phi_p(\sigma_{\text{el}} + \sigma_{\text{al}})\tau P_a}{Ah\nu_p} - N\sigma_{\text{al}}L \qquad (2.31)$$

In an approximation of the constant inversion along the fibre length, the absolute gain factor of the fibre amplifier of the length 'L' is therefore:

$$G = \frac{P(L)}{P(0)} = \exp[G_0] \qquad (2.32)$$

where 'P_a' is the absorbed pump power, 'N' is the laser-active centre concentration, and 'L' is the gain medium length. Note that the expression '$N\sigma_{\text{al}}L$' indicates total absorption loss throughout the whole length of the gain fibre at laser oscillation wavelength. In the general case of the varied inversion along the gain fibre, the absolute gain factor should be integrated along the whole fibre length:

$$G = \exp\left[\int_0^L g_0(z)dz\right] \qquad (2.33)$$

For a high pumping level when the gain coefficient 'g_0' cannot be considered, a small value saturated gain coefficient 'g' can be expressed as follows:

$$g = \frac{g_0}{1 + I/I_s} \qquad (2.34)$$

where 'I' is the amplified light intensity and 'I_s' is a so-called gain saturation parameter defined as the intensity of the amplifying beam in an active medium where the small-signal (unsaturated) gain coefficient 'g_0' is reduced by 50 % (i.e., half). In turn, the gain saturation parameter with good approximation can be defined as the following general formula:

$$I_s = \frac{h\nu_L}{(\sigma_{\mathrm{el}} + \sigma_{\mathrm{ea}})\tau} = \frac{h\nu_L}{\sigma_{\mathrm{el}}\tau Q} \qquad (2.35)$$

where '$Q = 1 + \sigma_{\mathrm{ea}}/\sigma_{\mathrm{el}}$', and Q = 2 for three-energy-level systems (i.e., when $\sigma_{\mathrm{ea}} \approx \sigma_{\mathrm{el}}$). The stored energy in the four-level solid-state laser amplifier can be defined by the following expression [5]:

$$E_{\mathrm{st}} = h\nu_L NV = g_0 I_s V \qquad (2.36)$$

where 'V' is the amplifier gain volume and 'N' is the concentration of laser-active centres created during the pumping process. The single-pass gain in fibre amplifiers, expressed in units of dB, can be calculated using the following formula:

$$g(\lambda) = 10\log\left(\frac{I}{I_0}\right) = 10\log\, e^{\int_0^l g(z)\mathrm{d}z} = 10\log\left\{exp\left[\frac{\phi_p(\sigma_{el} + \sigma_{al})\tau P_a}{Ah\nu_p} - N\sigma_{al}l\right]\right\} \qquad (2.37)$$

2.2.4 Tm-doped fibre

2.2.4.1 Energy level of thulium ions

Tm-doped silica fibre is generally used to amplify signals at 2 μm waveband. Fig.2.5.1 (left) shows the energy diagram for Tm^{3+} ions including four manifolds as well as its Stark levels for Tm^{3+} doped crystals or silicate glass fibres. As seen in Fig.2.5.1 (right), the $^3F_4 \rightarrow {}^3H_6$ transition peaks near 1850 nm and produces an extremely wide, featureless emission band that provides a broad tuning range for lasers and a wide optical bandwidth for amplifiers. Similarly, Fig.2.5.1 (red) shows that the $^3H_6 \rightarrow {}^3F_4$ absorption band is broad due to the larger number of Stark components in the Tm^{3+} manifolds and the slightly larger splitting. Silica fibre lasers have been operated at wavelengths ranging from 1700 [6] to 2056 nm [7]. It can be seen that the lower laser level (here $^3H_6$) is so close to the ground state that a significant population in that level occurs in thermal equilibrium when at the operating temperature.

Therefore, the unpumped gain medium causes some reabsorption loss at the laser wavelength, especially for the short-wavelength which is closer to ground level than the longer wavelength.

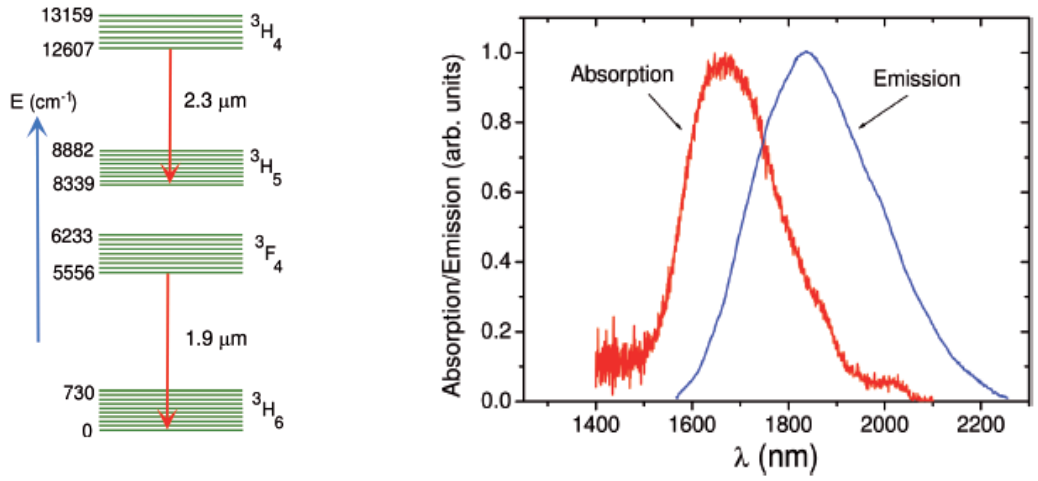

Fig. 2.2.6. Energy level schematic of Tm-Tm energy transfer and absorption & emission spectra from $^3F_4$ to $^3H_5$ [8].

The $^3H_4$ to $^3H_5$ transition, which corresponds to 2.3 μm emission, was only reported for the fluorozirconate glass fibre laser [9], and there was no report showing silica glass fibre lasers using these energy levels. This is due to the ultra-short lifetime of the $^3H_4$ energy level in silica glass and the relative branching ratio from $^3H_5$. For this reason, most of the energy transfer for the Tm^{3+} ions involved a $^3F_4$ to $^3H_6$ transition with a stimulated emission of around 1.9 μm. The energy gap between the $^3F_4$ and $^3H_6$ levels was only 4820 cm^{-1} and such a narrow gap meant that the radiative and non-radiative transition rates were of a similar magnitude. The energy level lifetime of $^3F_4$ was calculated to be 335 μs including the non-radiative decay [10]. Additionally, according to several reports [8,11] the energy level lifetime of $^3F_4$ was measured to be around 420 μs and 200 μs by Hanna D. C. in [12]. Therefore, thulium doped fibre lasers usually have high laser thresholds.

2.2.4.2 Pump scheme

Pump wavelength band

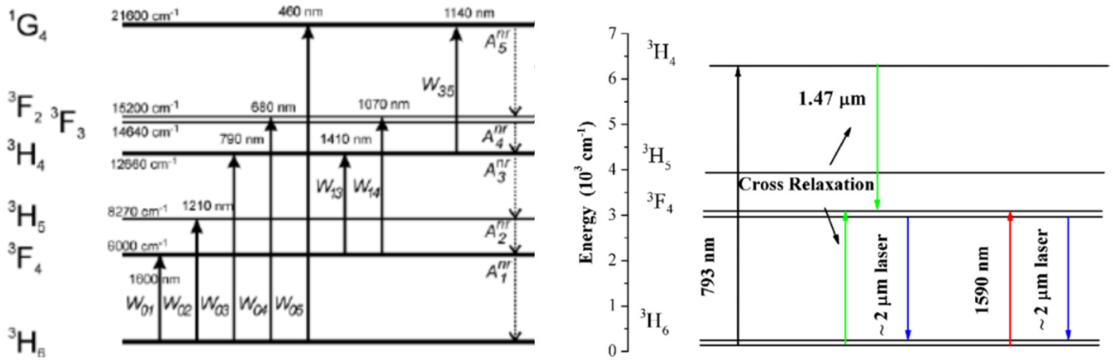

Fig. 2.2.7. Energy level schematic of thulium ions energy transfer [13,14].

To obtain the best efficiency for directly pumped lasers and amplifiers through thulium doped fibres, pump bands that overlap excited states absorption (ESA) bands should be avoided. The ESA will raise the threshold pump power and reduce the slope efficiency, while it can also cause a laser to operate at a wavelength that is somewhat offset from that with the highest emission cross sections. This is because the population of the upper laser level leads not only to amplification by stimulated emission, but also to absorption processes for the pump or laser radiation where laser ions are excited to a higher-lying energy level. Fig. 2.5.2 (left) suggests that for gain transitions that originate on the $^3F_4$, the $^3F_4 \rightarrow {}^3F_2$, and $^3F_3$ (1050- to 1120-nm) ESA transitions may interfere with pumping the $^3H_5$ when at about 1190 nm. The $^3F_4 \rightarrow {}^1G_4$ (635-nm) ESA transition however, may have an effect on pumping through the $^3F_2$ and $^3F_3$ states which are at 660-685 nm [15]. Due to a strong ESA, such band pumping leads to slope efficiencies below 30% [16].

As shown in Fig.2.5.2 (right), the pumping wavelengths on $^3H_6 \rightarrow {}^3H_4$ and $^3H_6 \rightarrow {}^3F_4$ are most commonly used through 793 nm and 1600 nm respectively. The 793 nm pumping wavelength presents a significant benefit in that the quantum efficiency can surpass 100% and theoretically even reach 200%. This comes from the process of cross-relaxation (CR). Ground state ($^3H_6$) ions are pumped into the $^3H_4$ level and a cross-relaxation process (green line in Fig. 2.5.2 (right)) populates the other ground ions into the upper laser $^3F_4$ level for the energy transfer process of $^3H_4 \rightarrow {}^3F_4$. Then, finally there will be two ions in the energy $^3F_4$ level. Therefore, the amplification efficiency can be over a quantum defect; in [17, 18], it

was reported that above 60% was achieved (quantum efficiency>150%) in Tm^{3+}-doped fibre lasers. Furthermore, pumping at a wavelength band under the developed high-power erbium-ytterbium co-doped fibre laser (EYDFL) at around 1600 nm is cost-effective. It also has additional advantages, such as having high Stokes efficiency (0.75 – 0.87) and a low quantum defect [19], which are beneficial in achieving high efficiency and low thermal management issues.

Furthermore, several proposed investigations use the cascaded tandem pumping technique and show its high power and highly efficient operation in the 2-μm wavelength region [20-22]. This kind of pumping scheme uses a 1942 nm Tm^{3+} fibre laser as the pump source with a co- (counter-) propagating configuration. The 2020 nm Tm^{3+} fibre laser meanwhile, generates an output power of 34.68 W with an 84.4% optical-to-optical efficiency and 91.7% slope efficiency, with respect to launched pump power [20].

Core and cladding pumping

Core pumping and cladding pumping are two types of optical pumping schemes in the fiber lasers or amplifiers. Fig. 2.2.8 schematically explains these two pumping schemes. The signal light propagates in the core and only the core is rare-earth-doped for both core pumping and cladding pumping, while the difference is about pumping light. In the core-pumping scheme, the pumping light source is single mode and launched to the single mode core to amplify the signal, and the amplified signal is also single mode. In the cladding-pumping scheme, the pumping light source is multimoded and launched to the entire cladding (referred to as the first cladding). The first cladding is further surrounded by the second cladding with a lower refractive index (normally the coating as the second cladding).

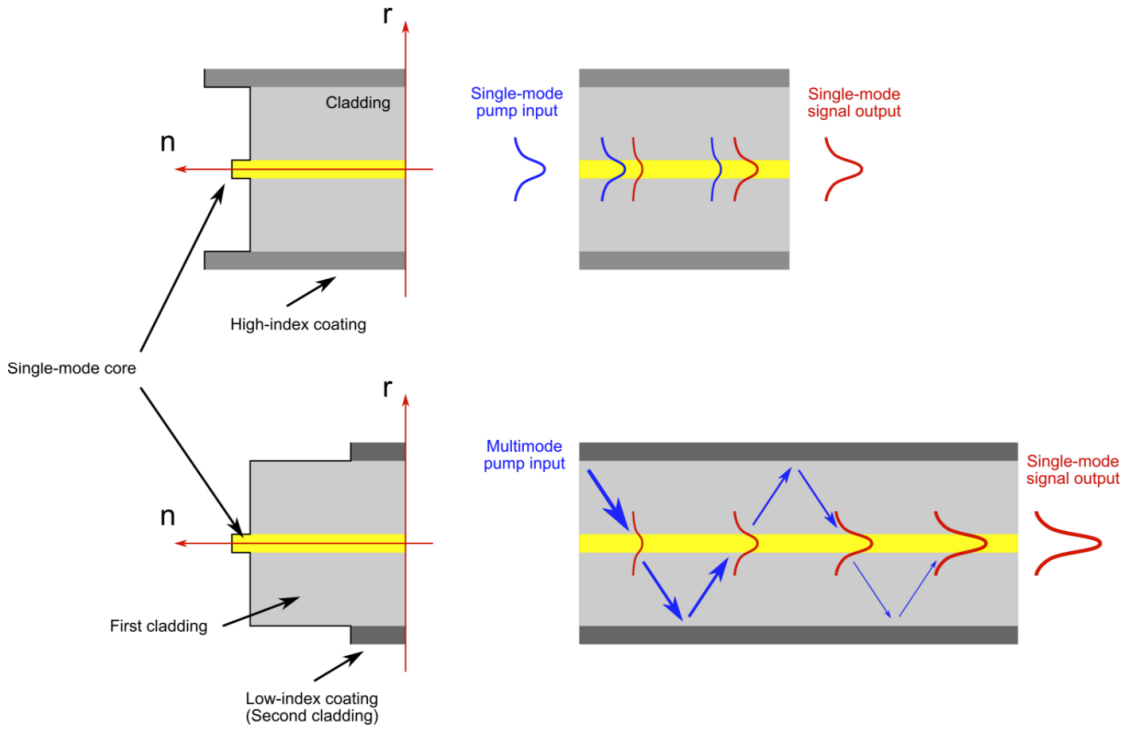

Fig. 2.2.8 Core-pumping and cladding-pumping schemes for rare earth doped fibre [23].

Pump absorption is much higher in the core-pumped configuration (As the table. 2.6.1 shown) due to the large overlap between the pump and signal, which helps to reduce the active fibre length so as to amplifier length. High-gain amplification is achievable with this approach because of high population inversion. However, the core-pump scheme has a notable drawback that applicable pump power is limited by the smaller fibre core so commercial single-mode pump diodes normally just have hundreds mW level output power. This is possible to build a single mode fibre laser as a core-pumped source over tens of Watt level, while the extremely high cost and systematic complexity limit this way compared with cheap chip diodes pump. Therefore, the core-pumping approach is more suitable for building preamplifiers with lower power requirement and some of situation which the short amplifier length is significant.

Table. 2.6.1. Absorption for core and cladding pumping scheme of thulium-doped fibres used in this thesis.

Fibre types	Pumping scheme	Absorption (dB/m)
OFS TmDF200	Core pump at 1560nm	20

Nufern PLMA-TDF-25P/400-HE	Cladding pump at 793nm	6
	Core pump at 1560nm	500
Home fabricated 1st generation of Germanate TDF	Cladding pump at 793nm	20
	Core pump at 1560nm	300
Home fabricated 2nd generation of Germanate TDF	Cladding pump at 793nm	50
	Core pump at 1560nm	500

Double-clad pumping is nearly the only one possible scheme for very high output power laser generation in fiber technology. A double-clad fibre has a doped core which guides the signal light and an inner cladding surrounded by a layer of low-index coating which enables pump light propagation in the inner cladding. Therefore, high power multimode pump diodes can be used owing to the large dimension of the inner cladding, whereas the signal light can maintain single-mode operation and thus good beam quality. The inner cladding has a significantly larger area (compared with that of the core) and typically a much higher numerical aperture, so that it can support a large number of propagation modes, allowing the efficient launch of the output through high-power multimode laser diodes (reach at ~hundreds Watt). However, pump absorption in double-clad fibre is much less efficient than that in a core-pumped fibre (as table. 2.6.1 shown) because the pump light has small overlap area with the core. There is another important issue when cladding pumping scheme is employed for conventional centered core fibre. Some of the pump rays launched to the first cladding does not cross the core due to the very high degree of symmetry in the fiber structure, and as a result, the pump is not efficiently absorbed. This can be improved by breaking the circular symmetry in the fibre structure, for examples as Fig. 2.2.9 shown, panda type of stress-applying cladding Nufern PLMA-TDF-25P/400-HE fibre (left) and the home fabricated germanate thulium doped fibre (right) with hexagonal cladding which are used in the experiment.

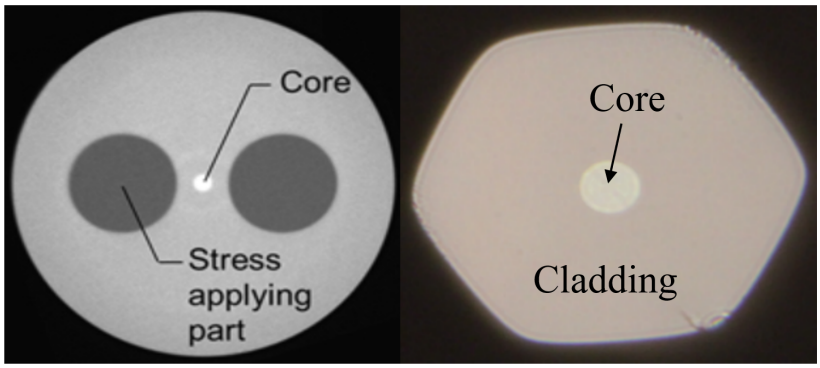

Fig. 2.2.9. Two designs of double-clad fibers. (left) The applying stress panda PM fibre. (right) The home fabricated hexagonal cladding double cladding fibre.

2.3 Pulse propagation in fibres

2.3.1 Nonlinear pulse propagation

The basic nonlinear pulse propagation in a fibre is described by the Nonlinear Schrödinger equation (NLSE) and can be represented by a relatively simple equation [24]:

$$\frac{\partial A}{\partial z}+\frac{\alpha}{2}A+\frac{i\beta_2}{2}\frac{\delta^2 A}{\delta T^2}-\frac{\beta_3}{6}\frac{\delta^3 A}{\delta T^3}=\ i\gamma(|A|^2A+\frac{i}{\omega_0}\frac{\partial}{\partial T}(|A|^2A)-T_RA\frac{\partial|A|^2}{\partial T}) \qquad (2.38)$$

where 'A' represents the pulses envelope variation with a distance 'z' at time 't'. 'β_2' and 'β_3' are group velocity dispersion (GVD) and the third order dispersion respectively. 'α' is the fibre linear loss and 'γ' is the fibre nonlinear parameter.

In order to simplify the NLSE, let us assume a relatively broad pulse width (e.g., T≥5ps). In this case, the last two terms '$\frac{i}{\omega_0}\frac{\partial}{\partial T}(|A|^2A)$ and $-T_RA\frac{\partial|A|^2}{\partial T}$' in eq.2.38 can be ignored because the parameters $\frac{1}{\omega_0 T}$ and $\frac{T_R}{T}$ are very small (≤0.0001). On the other hand, unless the wavelength of operation is very close to the zero-dispersion wavelength, the third order dispersion term '$\frac{\beta_3}{6}\frac{\delta^3 A}{\delta T^3}$' is also very small. In the end, we obtain the simplest NLSE because of the third-order nonlinearity which is represented by:

$$\frac{\partial A}{\partial z}+\frac{\alpha}{2}A+\frac{i\beta_2}{2}\frac{\delta^2 A}{\delta T^2}=i\gamma(|A|^2A) \qquad (2.39)$$

Briefly, there are three terms in the basic NLSE (eq. 2.39) including the loss term ($\frac{\alpha}{2}A$), the GVD term ($\frac{i\beta_2}{2}\frac{\delta^2 A}{\delta T^2}$) and the nonlinear term (SPM) ($i\gamma(|A|^2 A)$). In order to include the higher order nonlinearity terms, NLSE eq.2.39 needs to be modified [24].

The nonlinear parameter (γ) in equation 2.38 and equation 2.39 is defined as:

$$\gamma = \frac{\omega n_2}{c A_{eff}} \qquad (2.40)$$

and the effective mode area (A_{eff}) is defined as:

$$A_{eff} = \frac{(\iint_{-\infty}^{\infty} |F(x,y)|^2 \, dx \, dy)^2}{\iint_{-\infty}^{\infty} |F(x,y)|^4 \, dx \, dy} \qquad (2.41)$$

n_2 is nonlinear when it has a unit of m^2/W, and so is γ when it has a unit of W^{-1}/m. It is useful to introduce the following two length terms:

$$L_D = \frac{{T_0}^2}{|\beta_2|} \qquad (2.42)$$

$$L_{NL} = \frac{1}{\gamma P_0} \qquad (2.43)$$

The dispersion length (L_D) and nonlinear length (L_{NL}) in Eqn. 2.42 and 2.43 describe how far the pulse needs to travel before either or both of these effects begin to dominate in the propagation. There are several conditions that can be drawn from the relationships between L (propagation length), L_D and L_{NL}: when both L_D and L_{NL} are much smaller than L, neither GVD nor SPM play a significant role on the pulse propagation in the fibres; when L_D is much smaller than L_{NL} meanwhile, the GVD effect becomes dominant, and vice versa.

Thulium doped fibres have a measured GVD parameter of ~ 0.02 ps^2/m at 1.9 μm so the dispersion length L_D is estimated to be >500 km for ~100 ps pulses through eqn. 2.42. The impact of dispersion on TDFAs with "metre-scale" device lengths is neglectable. Nonlinear

parameters for different fibres used in this thesis are calculated and summarised in table 2.3.1, using Eqn. 2.40 and $n_2 = 3.55\times10^{-20}\ m^2\cdot W^{-1}$ for silica fibre, $n_2 = 5.5\times10^{-20}\ m^2\cdot W^{-1}$ for germanate fibre.

Table. 2.3.1. Estimated nonlinear parameters for different thulium doped fibres used in this thesis.

Fibre types	MFD (μm)	A_{eff} (μm^2)	γ ($W^{-1}\cdot km^{-1}$)
OFS TmDF200	6	28	4.1
SM28	8.6	58	1.97
Nufern UHNA4	4	12.5	9.18
Nufern PLMA-TDF-25P/400-HE	22	380	0.3
Home fabricated germanate TDF	18	254	0.69

2.3.2 Group velocity dispersion

If the nonlinearity and loss terms in Eqn. 2.39 can be ignored then it can be written as:

$$i\frac{\partial A}{\partial z} = \frac{\beta_2}{2}\frac{\delta^2 A}{\delta T^2} \qquad (2.44)$$

Assuming $U(z,T)$ is the normalised optical field, the solution for Eqn.2.44 in the frequency domain [through Fourier transform of $(\widetilde{U}(z,\omega))$] is given by:

$$\widetilde{U}(z,\omega) = \widetilde{U}(0,\omega)\exp\left(\frac{i}{2}\beta_2\omega^2 z\right) \qquad (2.45)$$

Eqn.2.45 shows that no new frequency terms appear apart from the changing of the phase based on the original frequency components. Considering the start pulse is the Gaussian-shape with function:

$$U(0,T) = \exp(-\frac{T^2}{2{T_0}^2}) \qquad (2.46)$$

where T_0 is defined as the pulse width, however, full width at half maximum (FWHM) is generally used to express the pulse width, and for a Gaussian pulse these two terms are related by $T_{FWHM} \approx 1.665 * T_0$. Therefore, the variation in pulse amplitude with propagation distances can be expressed as:

$$U(z,T) = \frac{T_0}{\sqrt{{T_0}^2 - i\beta_2 z}} e^{\left[-\frac{T^2}{2({T_0}^2 - i\beta_2 z)}\right]} \qquad (2.47)$$

While the phase variation with propagation distance is represented as:

$$\phi(z,T) = -\frac{sgn(\beta_2)\left(\frac{Z}{L_D}\right)}{1+\left(\frac{Z}{L_D}\right)^2}\frac{T^2}{2{T_0}^2} + \frac{1}{2}\tan^{-1}\left(sgn(\beta_2)\left(\frac{Z}{L_D}\right)\right) \qquad (2.48)$$

The sgn(β_2) is the sign of the dispersion parameter β_2, e.g., for single-mode fibre at 2 μm, β_2 is negative. Similarly, the change in central frequency (chirp) can be obtained from eq.2.48, while the figure below (Fig.2.3.1) plots the frequency chirp as a function of z/LD as well as the dispersion parameter β_2:

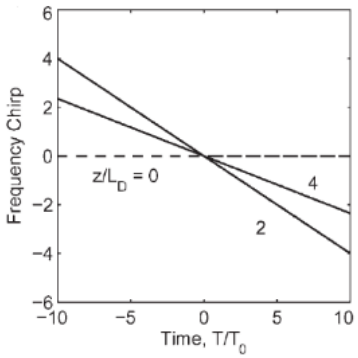

Fig. 2.3.1. Frequency chirp δω as functions of T/T0 for a Gaussian pulse at z=0, $2L_D$ and $4L_D$ [24].

2.3.3 Self-phase modulation

If the nonlinear effects (SPM) become dominant, and if the GVD term can be ignored then is simplified as:

$$\frac{\partial A}{\partial z} = \frac{ie^{-\alpha z}}{L_{NL}}|A|^2 A \qquad (2.49)$$

The general solution of eq.2.49 (using normalised optical field $U(z,T)$) is given by:

$$U(L,T) = U(0,T)\exp\left[i\phi_{NL}(L,T)\right] \qquad (2.50)$$

with a nonlinear phase shift:

$$\phi_{NL}(L,T) = |U(0,T)|^2 (L_{eff}/L_{NL}) \qquad (2.51)$$

$$L_{eff} = \frac{[1-e^{-\alpha L}]}{\alpha} \qquad (2.52)$$

where L_{eff} is the effective fibre length of fibre length L and depends on the fibre linear losses α. For the Gaussian pulse, the frequency chirp ($\delta\omega$) is given by eq.2.53.

$$\delta\omega(T) = -\frac{\partial\phi_{NL}}{\partial T} = \frac{2}{T_0}\frac{L_{eff}}{L_{NL}}\frac{T}{T_0}\exp\left|-\left(\frac{T}{T_0}\right)^2\right| \qquad (2.53)$$

For a Gaussian beam with a beam radius 'w' in a medium with length 'L', the phase change per unit optical power is described by the proportionality constant 'γ_{SPM}' in the unit of 'rad/W'. This means that the phase change per unit power is:

$$\gamma_{SPM} = \frac{4n_2 L}{\lambda w^2} \qquad (2.54)$$

Therefore, the maximal nonlinear phase changes due to SPM in the pulse centre can be described as:

$$\Delta\varphi_{NL,max} = \gamma_{SPM} \cdot P_{peak} \qquad (2.55)$$

Assume that an unchirped Gaussian pulse is injected into an TDFA for amplification to pulse energy of 1 μJ. Nonlinear phase shift for different TDFAs and input pulse-width are calculated and summarised in table 2.3.2, using table 2.3.1 and Eqn. 2.55. The calculated theoretically results show the following three indications:

a): The amplifier nonlinear phase shift decreases linearly (900π → 3π) as the pulse-width increasement (0.5ps → 150ps). Hence, stretch the pulse-width before the power amplifier to reduce the nonlinearity in the CPA system is able to achieve high pulse energy compared with directly amplification.

b): The amplifier nonlinear phase shift decreases (40π → 3π) as the fibre mode-filed area increasement (6μm → 22μm). The usage of LMA fibre in the power amplifier is desirable for pursing high energy pulse.

c): By using highly doping thulium doped fibre to short amplifier length (1m → 0.1m) can help to reduce the nonlinear phase shift (3π → 1π), this encourage us to develop the highly doping rare-earth fibre to reduce nonlinearity in pulse amplification once the limitation of stretched ratio and fibre's mode-filed area appear.

Table. 2.3.2. Estimated nonlinear parameters for different thulium doped fibres used in this thesis.

TDFA fibre	MFD (μm)	Pulse width (ps)	Effective active fibre length (m)	γ_{spm} (mrad/W)	Nonlinear phase shift
OFS TmDF200	6	150	1	6	40 π
Nufern PLMA-TDF-25P/400-HE	22	0.5	1	0.45	900 π
		150	1	0.45	3 π
Home fabricated highly doping germanate TDF	18	150	0.1	0.15	1 π

2.3.4 Modulation instability

As a result of an interplay between the nonlinear and dispersive effects, many nonlinear systems exhibit an instability that leads to the modulation of the steady state. This

phenomenon was studied during the 1960s and is referred to as the modulation instability [25,26]. In an optical fibres context, modulation instability requires anomalous dispersion and manifests itself as breakup of the CW or quasi-CW radiation into a train of ultrashort pulses. This section discusses modulation instability in optical fibres as an introduction to soliton theory. Let us start once more with the NLS equation without fibre loss:

$$i\frac{\partial A}{\partial z} = \frac{\beta_2}{2}\frac{\partial^2 A}{\partial T^2} - \gamma|A|^2 A \qquad (2.56)$$

'A (z, T)' represents the amplitude of the field envelope, 'β_2' is the GVD parameter, and the nonlinear parameter 'γ' is responsible for SPM. In the case of CW radiation, the amplitude 'A' is independent of 'T' at the input end of the fibre at z = 0. Assuming that 'A (z, T)' remains time independent during propagation inside the fibre, Eq. (2.56) is readily solved to obtain the steady-state solution:

$$\bar{A} = \sqrt{P_0}\exp(i\phi_{NL}) \qquad (2.57)$$

where 'P_0' is the incident power and '$\phi_{NL} = \gamma P_0 z$' is the nonlinear phase shift induced by SPM. Equation (2.57) implies that CW light should propagate unchanged through the fibre, except for acquiring a power-dependent phase shift (and for a reduction in power when in the presence of fibre losses). Before reaching this conclusion however, we must ask whether the steady-state solution (2.57) is stable enough against small perturbations. To answer this question we slightly perturb the steady state, in so much that:

$$A = \left(\sqrt{P_0} + a\right)\exp(i\phi_{NL}) \qquad (2.58)$$

and then examine the evolution of the perturbation 'a (z,T)' using a linear stability analysis. Substituting Eq. (2.58) by Eq. (2.56) and linearising in 'a', we obtain:

$$i\frac{\partial a}{\partial z} = \frac{\beta_2}{2}\frac{\partial^2 a}{\partial T^2} - \gamma P_0(a + a^*) \qquad (2.59)$$

This linear equation can be easily solved in the frequency domain. However, because of the a^* term, the Fourier components at frequencies 'Ω' and '$-\Omega$' are coupled. Thus, we should consider its solution in the following form:

$$a(z,T) = a_1 \exp[\mathrm{i}(Kz - \Omega T)] + a_2 \exp[-i(Kz - \Omega T)] \qquad (2.60)$$

where 'K' and 'Ω' are the wave number and the frequency of perturbation, respectively. Equations (2.59) and (2.60) provide a set of two homogeneous equations for 'a1' and 'a2'. This set only has a nontrivial solution when 'K' and 'Ω' satisfy the following dispersion relation:

$$K = \pm\frac{1}{2}|\beta_2\Omega|[\Omega^2 + \mathrm{sgn}\,(\beta_2)\Omega_c^2]^{1/2} \qquad (2.61)$$

Where depending on the sign of β_2, sgn(β_2) = ±1.

$$\Omega_c^2 = \frac{4\gamma P_0}{|\beta_2|} = \frac{4}{|\beta_2|L_{NL}} \qquad (2.62)$$

2.4 CPA system and components

2.4.1 Chirped pulse amplification

Chirped-pulse–amplification (CPA) temporally stretches an optical pulse before amplification and recompresses it to avoid detrimental nonlinear effects. For a typical CPA system structure as shown in Fig. 2.4.1, an ultra-short pulse from a mode-locked laser is stretched by a dispersive element, gets amplified and then re-compressed by the opposite dispersion. The dispersive elements are usually a grating-based pulse stretcher and compressor. he stretched pulse has a time-varying instantaneous frequency that is mainly determined by the pulse stretcher, thus the name chirped pulse. The onset of nonlinear effects imposes a limit on optical power, so the pulse energy extractable from the amplifier is linearly proportional to the pulse duration, and the achievable peak power after recompression also increases by the ratio at which the pulse duration increases.

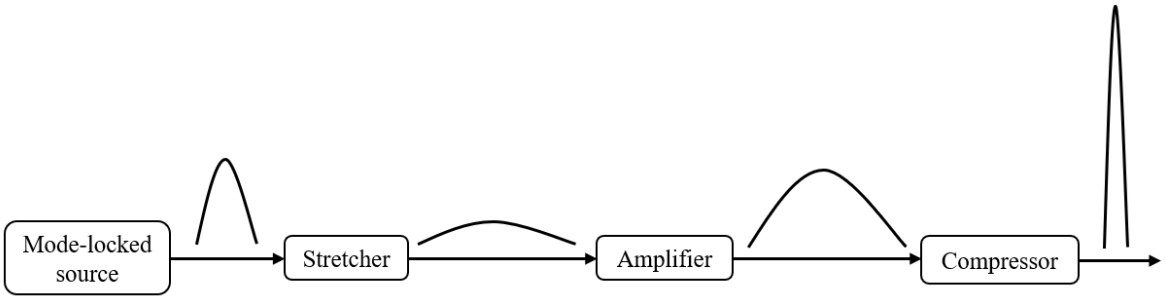

Fig. 2.4.1. Illustration of chirped pulse amplification system.

The CPA approach has been adopted by universities and research facilities all around the world since its first demonstration [27]. It has enabled production of optical pulses with petawatt (10^{15} W) peak power. A petawatt system was proposed [28] and first demonstrated on the Nova laser system at Lawrence Livermore National Laboratory [29]. The Nova petawatt laser employed a Ti:sapphire mode-locked oscillator as its seed and a Ti:sapphire regenerative amplifier in its front end. It produced 660 J of pulse energy using Nd:glass power amplifiers, which is required for amplification to kilojoule level. The Vulcan laser at the Rutherford Appleton Laboratory's Central Laser Facility delivers 500-fs compressed pulses with 500 J of pulse energy [30]. The highest peak power reported to date from a Ti:sapphire CPA system is produced by Shanghai Institute of Optics and Fine Mechanics, Chinese Academy of Sciences [31]. This system delivers 52 J of pulse energy in a 26 fs compressed pulse, achieving a peak power of 2 PW.

Compared with glass system above, CPA systems based on fibre amplifiers technology have also been developed that take advantage of increasing mode areas for active fibers. Fibre amplifiers are more limited by onset of detrimental nonlinear effects because of the tight spatial confinement of the optical signal and relatively long propagation distance in the material. However, they can provide higher average power because of their superior thermal handling capability. Furthermore, fibre system offer excellent beam quality and possibility of usage in the industrial area due to high stability and compactness. A fiber CPA system with higher pulse energy and peak power has been demonstrated [32]. This system produces 480-fs pulses with 2.2 mJ pulse energy, yielding a peak power of 3.8 GW. The power amplifier in the system is a 1.3-m long Yb-doped, photonic-crystal fiber with a 105-μm mode-field diameter. The large mode size reduces the intensity of the propagating pulse, which reduces accumulation nonlinear phase for the high peak power operation. The

stretcher and compressor in the fiber CPA systems above are grating based. The first all-fiber CPA system has been demonstrated using chirped-fiber-Bragg grating to stretch and compress the pulse [33].

2.4.2 Optical fibre

2.4.2.1 Large mode area (LMA) single mode fibre

The obvious way to increase the CPA system output energy and reduce the nonlinearity in the power fibre amplifier is to increase the fibre mode area. So, the large-mode-area (LMA) fibres are key elements in modern high power fibre lasers. The simplest LMA fibre is conventional multimode step-index fibre. Since multimode step-index fibres support multiple transverse guided modes, the beam quality of the output beam is worse than that from standard single-mode fibres. To obtain better beam quality, many LMA fibres designs have been developed.

For a step index core, the effective mode area can be enlarged by increasing the core size. For single mode fiber, the core refractive index has to be reduced when the core size is increased in order to maintain the single mode operation. The V must satisfy the following condition and below than value of 2.4 to support single mode:

$$V = \frac{2\pi}{\lambda} \cdot a \cdot NA \qquad (2.63)$$

where λ is the vacuum wavelength, α is the radius of the fiber core, and $NA = \sqrt{n_{core}^2 - n_{cladding}^2}$ is the numerical aperture.

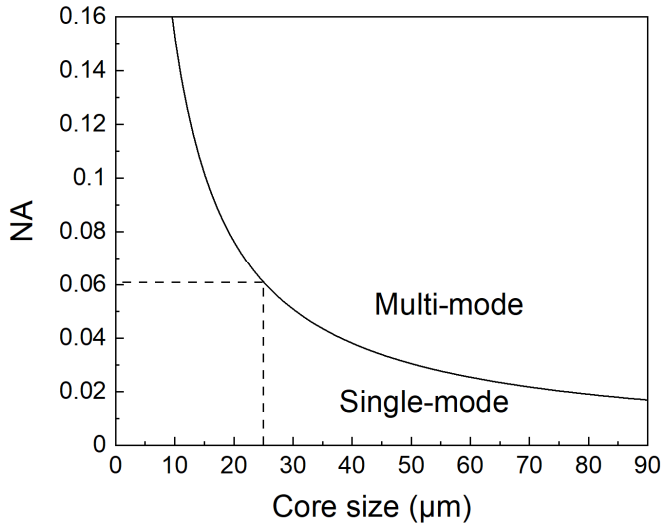

Fig. 2.4.2 Numerical aperture as a function of core diameter for the cutoff wavelength of 2 μm.

Fig. 2.4.2 plots the core numerical aperture as a function of core diameter for the cutoff wavelength of 2 μm by eq. 2.63. In this figure, single mode fiber operation can be achieved in the parameter region below the cutoff curve, while multimode fiber operation happens in the parameter region above the curve. When the core diameter increases, the core NA has to drop in order to keep the fiber single-mode operation. For example, for the fibre with core diameter of 25 μm, the NA should be equal to or below 0.06. The home fabricated germanate thulium doped fibre used in this thesis with core diameter of 20 μm and NA of 0.07 has V number of 2.2 which satisfy single mode operation. However, for the core diameter of 30 μm, the core NA should be less than or equal to 0.05. The low NA requirement for LMA fiber imposes practical limits on fiber manufacturing and bending performance. Especially for rare-earth-doped fibers, relatively high concentrations of additional dopants are often required and these dopants often increase the numerical aperture. Even if the refractive index contrast can be reduced in some way, the precision of refractive index control may be decreased, and this affects the ability to realize very large mode areas. Fiber core NA lower than 0.05 is difficult to achieve in step-index fiber.

One design on the gain-doping profile is gain filtered fibres, where the dopants are distributed partially in the core with smaller radius or with nonrectangular shape [34]. Single-mode operation can be achieved by denying the gain toward the edge of the core where most of the higher-order modes (HOMs) power is contained. Ring-shape refractive index fibre combines refractive index design and gain profile design, which consists of a

low-NA centre core region and an outer ring with a raised index [35]. The outer ring gives an increased spot size for the HOMs and increases their susceptibility to bend loss. Only the low-NA centre region is doped to achieve gain filtering for the HOMs.

Another approach is utilizing different modal bending loss is coiled multimode step index fibers [36]. The HOMs have higher bending loss than the fundamental mode. The coiling radius is chosen to provide high loss for the HOMs and negligible loss for the fundamental mode, such that HOMs will be filtered out and the fundamental mode will be guided. In other words, when a fiber is under bending conditions, the bend losses of the higher order modes increase more rapidly than the fundamental mode. By choosing a proper design and a bend radius, it is possible to achieve sufficient differential bend losses between the higher order modes and the fundamental mode while maintaining the bend loss of the fundamental mode below an acceptable low level. In this way, the higher modes are effectively attenuated, and the fibre behaves just like a single mode fiber. The fibre of Nufern PLMA-TDF-25P/400-HE used in this thesis is based on this approach.

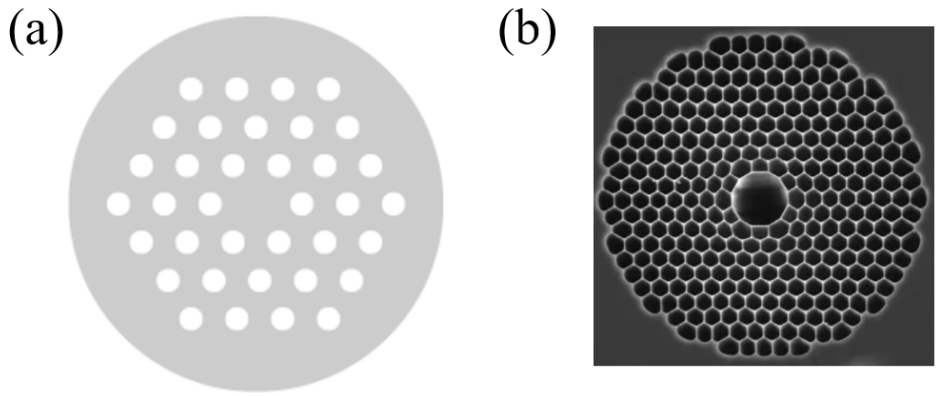

Fig. 2.4.3 (a) General solid-core photonic crystal fiber design. (b) Microscope picture of the end of a hollow-core fiber [37].

Photonic crystal fibres (PCF), also called micro-structured fibres, are a subset of LMA fibres with various designs. The common feature of PCF is the periodic structure in the cladding and an imperfection in the center as the core, which can be solid (as Fig.2.4.3 (a) shown), liquid, or air. PCF can be further divided into several subcategories. Some PCF essentially operates by following the total internal reflection (TIR) in conventional fibres. The light in the fibre is guided in the high index core surrounded by cladding, which are embedded with low index air holes. This arrangement gives better control of the effective cladding index, resulting in NA as low as 0.02 rather than the limitation of NA 0.05 in the conventional step

index fibre. Photonic band-gap fibres are PCF utilizing the photonic band-gap effect [38]. The light in the fiber can be guided in the low index core (air), surrounded and confined by periodic high-index structures which act as two dimensional Bragg mirrors. The latter mechanism even allows guidance in a hollow core (Fig.2.4.3 (b)), such that most of the power propagates in the central hole (hollow-core fibers). Such air-guiding hollow-core photonic crystal fibers (or air core bandgap fibers) can have a very low nonlinearity and a high damage threshold.

2.4.2.2 Polarization maintaining (PM) fibre

As the grating base compressor are normally polarized light dependent and polarized light required, the PM fibre is used in the CPA system. In an ordinary non-polarization maintaining single mode fibre, two degenerate orthogonal polarization modes (vertical and horizontal polarization) can exist. Under ideal conditions (perfect circular symmetry), the two modes have the same phase velocity and would not couple to each other. However, tiny amount of random birefringence caused by circular symmetry breaking during the manufacturing process or bending in the fibre, will result in the crosstalk between these two polarization modes. A PM fiber guides two optical modes with orthogonal polarizations, and minimizes transfer between them in the presence of external perturbations, such as bend, twist or pressure across the fiber. When a linearly polarized signal is launched along one of the guided modes, the polarization state is maintained at the fiber output. The fundamental mechanism of the polarization maintaining property is a high birefringence built into the PM fiber. For regular fiber without high birefringence, external perturbations disturb the polarization state of the propagating signal by introducing random birefringence along the fiber. The internal birefringence of the PM fiber is much higher than that caused by external perturbations, which makes the latter negligible and the propagating signal insensitive to the environment.

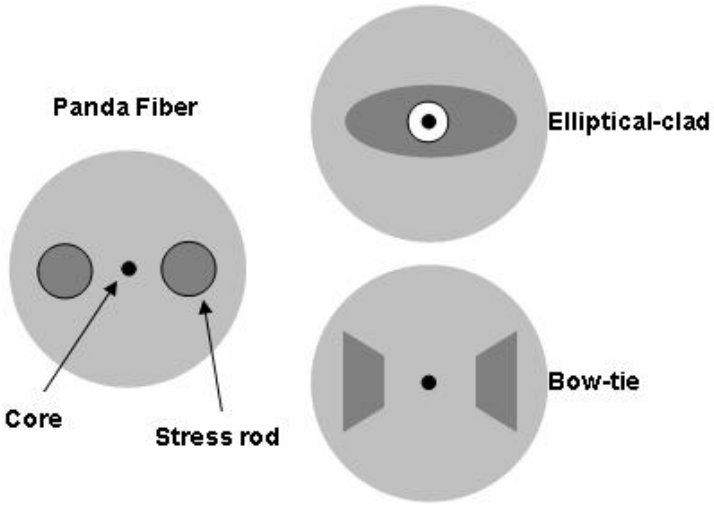

Fig.2.4.4 Cross sections of three types of PM fiber [39].

Several different designs are used to create birefringence in a fiber [40]. The fibre may be geometrically asymmetric or have a refractive index profile which is asymmetric such as the design using an elliptical cladding as shown in the Fig.2.4.4. Alternatively, stress permanently induced in the fiber will produce stress birefringence. This may be accomplished using rods of another material included within the cladding. Several different shapes of rod are used, and the resulting fiber is sold under brand names such as "PANDA" and "Bow-tie". The Nufern PLMA-TDF-25P/400-HE used in this thesis is PM fibre based on “PANDA” rod approach.

2.4.3 Stretcher and compressor

In a typical CPA system, an ultra-short seed pulse is stretched in time by a positive dispersion line (stretcher), while the amplified chirped pulse is compressed by a matching negative dispersion line (compressor). This section introduces existing common technologies for the optical pulse stretcher and compressor, including grating pair, dispersive fibre, chirped fibre and volume Bragg grating, and then draws comparisons between them.

2.4.3.1 Grating pairs

Grating pairs are one of the most commonly used techniques applied to work as the stretcher or compressor in a typical CPA system. There are two major types of gratings, including conventional reflection grating and fused silica transmission grating. Compared to the conventional reflection grating with metallic coating, which limit the grating’s optical

performance and power handling, fused silica transmission grating has lower magnitudes absorption for intense energy pulses and better thermal stability [41].

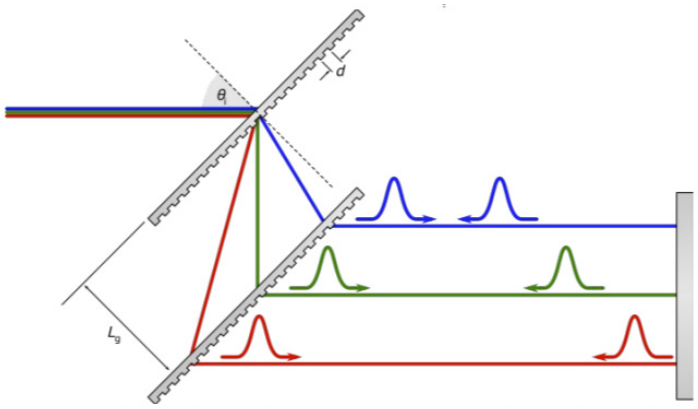

Fig. 2.4.5. The schematic of the Treacy stretcher or compressor [41].

A grating pair in its simplest structure is as shown in Fig.2.4.5. Also known as the Treacy configuration, it can produce adjustable negative dispersions due to the different wavelengths experienced through difference optical paths [42]. At the output of a grating pair, there is a reflector (e.g., roof mirror) to retroreflect the light back into the grating pair, and thus it can additionally generate double the amount of negative dispersion.

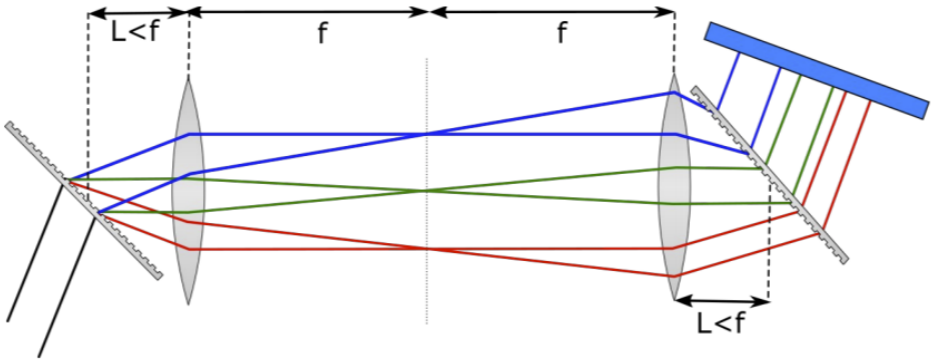

Fig. 2.4.6. The schematic of the Martinez stretcher or compressor [41].

As previously mentioned, this simple Treacy configuration can only yield negative dispersion. Another grating pair layout with a more complicated structure however, is able to produce positive dispersion (in Fig. 2.4.6). The most commonly used arrangement for this is the so-called Martinez-arrangement where two lenses are placed between the two gratings. The two lenses form a telescope with a magnification factor M = 1, when L = f. By adjusting the distances L < f, this layout allows for the introduction of “negative” separations between

the gratings, and thus achieves positive dispersion. The chromatic dispersion introduced by a grating pair, as above, is given using the following equation:

$$\frac{d^2\phi}{d\omega^2} = -\frac{m^2\lambda^3 L_g}{2\pi c^2 \Lambda^2} \cdot \left[1 - \left(-m\frac{\lambda}{\Lambda} - \sin\theta_i\right)^2\right]^{-\frac{3}{2}} \qquad (2.64)$$

where 'm' is the diffraction order (usually -1), 'λ' is the centre wavelength, 'L_g' is the distance between the two parallel gratings (corresponds to the negative distance L in the Martinez-arrangement; in the case where the distance is L>f, this setup is the equivalent of the Treacy grating configuration), 'Λ' is the period of the grating, and 'θ_i' is the angle of incidence on the first grating.

2.4.3.2 Dispersive fibre

Chromatic dispersion results from a limited spectral bandwidth of the injected pulse into the fibre due to different spectral components of the pulse spectrum propagating along the fibre with different speeds: 'v=c/n(ω)', which is the frequency dependence of the refractive index n(ω). Because of the light speed difference between different spectral components, the propagating pulse eventually spreads in time and the pulse broadens. Eq. 2.65 gives the value of change of the original pulse's '$\Delta\tau$' width:

$$\Delta\tau = D\Delta\omega L \qquad (2.65)$$

where 'D' is chromatic dispersion specified with a unit of 'ps/(nm km)' and the other parameter of 'β_2' is named as the group velocity dispersion related to 'D' with a basic unit of s^2/m: $D = -(2\pi c/\lambda^2)\beta_2$. '$\Delta\omega$' is the spectral width.

Most of the common commercial silica-based fibres have an anomalous dispersion at a 2 μm wavelength band, e.g., β_2=-0.067 ps^2/m for SM28 fibre. Therefore, in this section I summarise several commercial fibres that have a normal dispersion at around a 2 μm wavelength range. These are in table 2.4.1.

Table. 2.4.1. Measured dispersion of fibres in the literatures.

Fibre types	β_2 (ps^2/m) at 1.9 μm	β_3 (ps^3/m) at 1.9 μm

UHNA1	0.036 [43 58] 0.038 [44] 0.047 [45]	NA
UHNA3	0.12 [44]	0 at 2020 nm [44]
UHNA4	0.093 [46] 0.09 [47]	$1.536*10^{-4}$ [46] $3.3*10^{-5}$ [47]
UHNA7	0.046 [44]	$-1.2 * 10^{-4}$ [44]
PM2000	0.09 [44]	0 at 2130 nm [44]

2.4.3.3 Chirped fibre& volume Bragg grating

In this section, the schematic and basic principles of chirped fibre Bragg grating (CFBG) and chirped volume Bragg grating (CVBG) are simply described. Due to their high performance and small size, these two components are widely used in compact, robust CPA systems as the stretcher and compressor. As we all know, the refractive index periodically changes its material leads to adapt to the reflection of light in a narrow range of wavelengths, as is shown by the equation for the Bragg condition in 2.66:

$$\lambda = 2n_{\text{eff}}\Lambda \qquad (2.66)$$

where Λ is the grating period, λ is the vacuum wavelength, and 'n_{eff}' is the effective refractive index of light in the material. Fig.2.4.7 shows the configuration of a CFBG (left) and CVBG (right). Both of these create the periodic disparity in the refractive index, and each segment then reflects or reproduces the exact corresponding wavelength of the light signal and then transmits all the others signals. Therefore, each reflected spectral fraction has a different optical propagation path so as to generate dispersion.

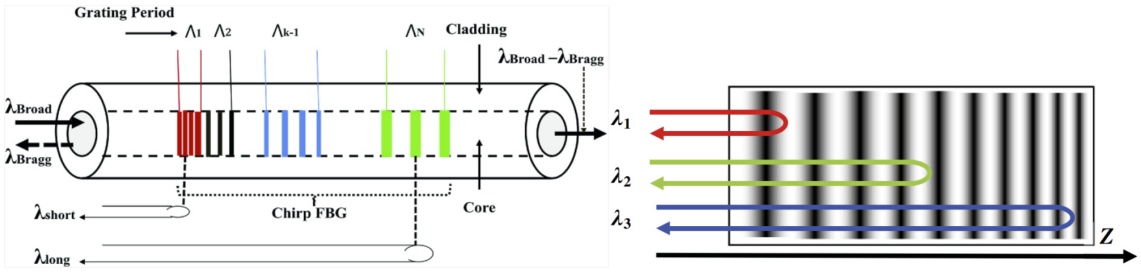

Fig.2.4.7. The configuration of the CFBG (left) and CVBG (right) [48,49]

2.4.3.4 Characterization of stretcher and compressor

In this section, a summary of the above mentioned four most common stretchers and compressors are presented. A significant advancement in the development of CPA systems was made using CFBGs. The approach dramatically increased the robustness and compactness of CPA systems due to its improved fibre technology, when compared with the grating pair or volume grating. Also, CFBGs with ultra-short length dispersive fibres have advantages in their stability as well as having a lower nonlinearity accumulation than when using the conventional hundreds of metres of dispersive fibres. However, the CFBGs with a fixed working wavelength and GVD value require customised design and limit the usage scenarios, especially in the preliminary experimentally research area. The dispersive fibre and CFBG are a type of fibre-based technology that have strong light intensity in the core. However, there are limitations on the peak power achievable with pulse compressors due to the nonlinear effects and laser-induced damage on the fibres, hence, both of dispersive fibre and CFBG normally work as the stretcher when at the low peak power operation region. A conventional compressor is based on a grating pair placed with one at some distance from the other, including the amount of large size bulk optics. Therefore, a grating pair compressor is not only environmentally sensitive but also occupies space. A typical CVBG allows for a decrease in the size and weight of the compressors by several orders of magnitude as the device is monolithic, which in turn helps to enhance the compactness and robustness of the CPA systems. Similar to the CFBG, the CVBG with a fixed/designed working wavelength and GVD value limit the flexibility for some preliminary research areas. In addition, the narrow bandwidth of the current CVBG technology limits the compressed pulse-width to longer than 100 fs [49]. Table 2.4.2 typically characterises the above mentioned four types of dispersion management devices.

Table. 2.4.2. Typical characterizations for four types of dispersion management devices

	Dispersive fibre	CFBG	Grating pair	CVBG
Typical size for 0.5 ns stretching time	~km level of coilled fibre	~cm level of fibre	~100 cm^2 level of size and several meters of free space distance	~cm level of glass with beam size aperture (up to 10mm).
Transmission efficiency	~50% (assume fibre with 3dB/km transmission loss)	80%~90%	60~70%	80%~90%

Working bandwidth	＞500nm	Customised and fixed (~50nm)	~200 nm	Customised and fixed (~50nm)
Achievable beam diameter	~μm level	~μm level	~mm level	~mm level

In this thesis, for stretcher I used tens meters of dispersive fibres (Nufern UHNA4&7) due to the good wavelength band compatibility and low cost compared with the customized CFBG. Obviously, the dispersive fibres are much compact and robust compared with the conventional grating pair based stretcher. For compressor, a grating pair was used because of the waveband flexibility and availability compared with the customized CVBG.

2.5 Summary

In this chapter, I have explained the background of the fibre laser and of the amplifier fundamental theory including the energy level and the pump scheme used for thulium doped fibre, pulse propagation in fibres including chromatic dispersion, self-phase modulation and modulation instability. Following this, the mode-locking mechanism, three types of dispersion managed pulses and saturable absorbers are introduced. These will thus be explored in the next chapters on the mode-locked pulses generation. After that, CPA system mechanism and keys components will be described including LMA and PM fibres, stretcher and compressor.

Reference

[1] O. Svelto, "Principles of Lasers", Springer US, (2010).

[2] J. R. Simpson, " Optical and electronic properties of rate earth ions in galsses" in Rare-earth-doped fiber lasers and amplifiers (2nd Edition) Marcel Dekker, Inc., (2001).

[3] V. Ter-Mikirtychev "Fundamentals of Fiber Lasers and Fiber Amplifiers", Springer, Cham, (2014).

[4] A. E. Siegman, "Lasers", Univ Science Books (1986).

[5] C.R. Giles, E. Desurvire, "Propagation of signal and noise in concatenated erbium-doped fiber optical amplifiers", IEEE J. Lightwave Technol. Lett. **9**(2), 147–154, (1991).

[6] W.L. Barnes, and J.E. Townsend, "Highly tunable and efficient diode pumped operation of Tm3+ doped fibre lasers," Electron. Lett. **26**(11), 746–747 (1990).

[7] J. Li, Z. Sun, H. Luo, Z. Yan, K. Zhou, Y. Liu, and L. Zhang, "Wide wavelength selectable all-fiber thulium doped fiber laser between 1925 nm and 2200 nm," Opt. Express **22**(5), 5387-5399 (2014).

[8] B. Mellish, "File:Self-phase-modulation.png - Wikimedia Commons", Commons.wikimedia.org, 2005. [Online]. Available: https://commons.wikimedia.org/wiki/File:Self-phase-modulation.png. [Accessed: 10- Aug- 2016].

[9] F. Haxsen, A. Ruehl, M. Engelbrecht, D. Wandt, U. Morgner and D. Kracht, "Stretched-pulse operation of a thulium-doped fiber laser", Opt. Express, **16**(25), 20471 (2008).

[10] B. Walsh and N. Barnes, "Comparison of Tm: ZBLAN and Tm: silica fiber lasers; Spectroscopy and tunable pulsed laser operation around 1.9 μm", Applied Physics B **78**, 325-333 (2004).

[11] G. Agrawal, Nonlinear fiber optics. Amsterdam: Elsevier / Academic Press, (2007).

[12] D.C. Hanna, R.M. Percival, R.G. Smart, A.C. Tropper, "Efficient and tunable operation of a Tm-doped fibre laser," Opt. Commun. **75**(3-4), 283-286 (1990).

[13] P. Peterka, I. Kasik, A. Dhar, B. Dussardier, and W. Blanc, "Theoretical modeling of fiber laser at 810 nm based on thulium-doped silica fibers with enhanced 3H4 level lifetime," Opt. Express **19**(3), 2773-2781 (2011).

[14] N. M. Sharif, N. M. Yusoff, F. Ahmad, S. W. Harun and H. Ahmad, "Investigation of nitrogen doped graphene as saturable absorber in Thulium-Doped Fiber Laser," 2015 1st International Conference on Telematics and Future Generation Networks, 2015, 103-106.

[15] W. Miniscalco, "Optical and Electronic Properties of Rare Earth Ions in Glasses."Materials Science, (2001).

[16] Y. H. Tsang, D. J. Coleman, T. A. King, "High power 1.9 μm Tm3+-silica fibre laser pumped at 1.09 μm by a Yb3+-silica fibre laser," Opt. Commun. **231**(1-6), 357-364 (2004).

[17] N.Y. Voo, J. S. Sahu and M. Ibsen, "345mW 1836nm single frequency DFB fiber laser MOPA," IEEE Photonics Technol. Lett. **17**(12). 2550-2552 (2005).

[18] J. Xu, M. Prabhu, J. Lu, K. Ueda, and D. Xing, "Efficient double-clad thulium-doped fiber laser with a ring cavity," Appl. Opt. **40**(12), 1983-1988 (2001).

[19] D. Shen, J. Sahu, and W. Clarkson, "High-power widely tunable Tm:fibre lasers pumped by an Er,Yb co-doped fibre laser at 1.6μm," Opt. Express **14**(13), 6084-6090 (2006).

[20] Y. Wang, J. Yang, C. Huang, Y. Luo, S. Wang, Y. Tang, and J. Xu, "High power tandem-pumped thulium-doped fiber laser," Opt. Express **23**(4), 2991-2998 (2015).

[21] P. Zhou, H. Xiao, J. Leng, J. Xu, Z. Chen, H. Zhang, and Z. Liu, "High-power fiber lasers based on tandem pumping," J. Opt. Soc. Am. B **34**(3), A29-A36 (2017).

[22] F. Liu, P. Liu, X. Feng, C. Wang, Z. Yan, and Z. Zhang, "Tandem-pumped, tunable thulium-doped fiber laser in 2.1 μm wavelength region," Opt. Express, **27**(6), 8283-8290 (2019).

[23] https://www.fiberlabs-inc.com/glossary/core-pumping-and-cladding-pumping/

[24] G. Agrawal, "Nonlinear fiber optics", Amsterdam: Elsevier / Academic Press, (2007).

[25] G. Whitham, "Non-linear dispersion of water waves," Journal of Fluid Mechanics **27,** 399-412 (1967).

[26] T. Taniuti and H. Washimi, "Self-Trapping and Instability of Hydromagnetic Waves Along

the Magnetic Field in a Cold Plasma," Phys. Rev. Lett. **21**, 209 (1968).
[27] D. Strickland and G. Mourou, "Compression of amplified chirped optical pulses," Opt. Commun. **56**(3), 219−221 (1985).
[28] P. Maine, D. Strickland, P. Bado, M. Pessot and G. Mourou, "Generation of ultrahigh peak power pulses by Chirped Pulse Amplification," IEEE J. Quantum Electron, **24**(2), 398-403 (1988).
[29] M. D. Perry, D. Pennington, B. C. Stuart, G. Tietbohl, J. A. Britten, C. Brown, S. Herman, B. Golick, M. Kartz, J. Miller, H. T. Powell, M. Vergino, and V. Yanovsky, "Petawatt laser pulse," Opt. Lett. **24**(3), 160-162(1999).
[30] C. N. Danson, P. A. Brummitt, R. J. Clarke, J. L. Collier, B. Fell, A. J. Frackiewicz, S. Hancock, S. Hawkes, C. Hernandez-Gomez, P. Holligan, M. H. R. Hutchinson, A. Kidd, W. J. Lester, I. O. Musgrave, D. Neely, D. R. Neville, P. A. Norreys, D. A. Pepler, C. J. Reason, W. Shaikh, T. B. Winstone, R.W.W.Wyatt, and B. E.Wyborn, " Vulcan Petawatt-an ultra-high-intensity interaction facility," Nucl. Fusion **44**, 239 (2004).
[31] Y. Chu, X. Liang, L. Yu, Y. Xu, Lu. Xu, L. Ma, X. Lu, Y. Liu, Y. Leng, R. Li, and Z. Xu, "High-contrast 2.0 Petawatt Ti:sapphire laser system," Opt. Express **21**(24), 29231- 29239 (2013).
[32] T. Eidam, J. Rothhardt, F. Stutzki, F. Jansen, S. Hädrich, H. Carstens, C. Jauregui, J. Limpert and A. Tünnermann, "Fiber chirped-pulse amplification system emitting 3.8 GW peak power," Opt. Express **19**(1), 255-260 (2011).
[33] A. Galvanauskas, M. E. fermann, D. Harter, K. Sugden and I. Bennion, "All fiber femotosecond pulse amplification circuit using chirped Bragg gratings," Appl. Phys. Lett. **66**(9), 1053-1055 (1995).
[34] J. R. Marciante, "Gain Filtering for Single-Spatial-Mode Operation of Large-Mode Area Fiber Amplifiers," IEEE J. Sel. Topics in Quantum Electron. **15**(1), 30-36 (2009).
[35] J. A. Alvarez-Chavez, H. L. Offerhaus, J. Nilsson, P. W. Turner, W. A. Clarkson, and D. J. Richardson, "High-energy, high-power ytterbium-doped Q-switched fiber laser," Opt. Lett. **25**(1), 37-39 (2000).
[36] P. Koplow, D. A. V. Kliner, and L. Goldberg, "Single-mode operation of a coiled multimode fiber amplifier," Opt. Lett. **25**(7), 442-444 (2000).
[37] https://www.rp-photonics.com/photonic_crystal_fibers.html
[38] R. F. Cregan, B. J. Mangan, J. C. Knight, T. A. Birks, P. St. J. Russell, P. J. Roberts, and D. C. Allan, "Single-mode photonic band gap guidance of light in air," Science **285**(5433), 1537 (1999).
[39] http://opticfibertech.com/products/polarization-components/pm-fiber.
[40] A. Carter, and B, Samson, "PANDA-style fibers move beyond telecom," Laser Focus World, (2004).
[41] https://ibsen.com/wp-content/uploads/White-paper-Pulse-stretching-and-compressing-using-grating-pairs_v1.pdf
[42] E. B. Treacy, "Optical pulse compression with diffraction gratings," IEEE J. QuantumElectron. **5**(9), 454 (1969).
[43] F. Haxsen, D. Wandt, U. Morgner, J. Neumann, and D. Kracht, "Monotonically chirped pulse evolution in an ultrashort pulse thulium-doped fiber laser," Opt. Lett. **37**(6), 1014–1016 (2012).
[44] P. Ciąćka, A. Rampur, A. Heidt, T. Feurer, and M. Klimczak, "Dispersion measurement of ultra-high numerical aperture fibers covering thulium, holmium, and erbium emission wavelengths," J. Opt. Soc. Am. B, **35**(6), 1301-1307 (2018).
[45] A. Wienke, F. Haxsen, D. Wandt, U. Morgner, J. Neumann, and D. Kracht, "Ultrafast, stretched-pulse thulium-doped fiber laser with a fiber-based dispersion management," Opt. Lett. **37**(13), 2466–2468 (2012).
[46] Q. Wang, T. Chen, M. Li, B. Zhang, Y. Lu, and K. P. Chen, "All-fiber ultrafast thulium-doped fiber ring laser with dissipative soliton and noise-like output in normal dispersion by single-wall carbon nanotubes," Appl. Phys. Lett. **103**(1), 011103 (2013).
[47] Y. Tang, A. Chong, and F. W. Wise, "Generation of 8 nJ pulses from a normal-dispersion thulium fiber laser," Opt. Lett. **40**(10), 2361–2364 (2015).

[48] D. Meena, M.L. Meena, “Design and Analysis of Novel Dispersion Compensating Model with Chirp Fiber Bragg Grating for Long-Haul Transmission System,” Optical and Wireless Technologies. Springer, Singapore, 29–36 (2020).

[49] L. Glebov, V. Smirnov, E. Rotari, I. Cohanoschi, L. Glebova, O. Smolski, J. Lumeau, C. Lantigua, and A. Glebov, “Volume-chirped Bragg gratings: monolithic components for stretching and compression of ultrashort laser pulses,” Opt. Eng. **53**(5), 051514 (2014).

Chapter 3

Tm-doped mode-locked fibre laser for CPA system

3.1 Introduction

Mode-lock techniques are commonly used to generate stable picosecond or femtosecond pulses as the seed source in the CPA systems. Therefore, in this chapter, my target is to develop a Tm-doped mode-locked (ML) fibre laser for the high performance 2 μm Tm-CPA systems. I include a statement of the parametric performance for the idea ML pulse source below:

a) Pulse width is needed to be tens of picosecond in order reduce the nonlinearity in the dozens of meters dispersive fibres for the stretcher after the ML source in the CPA system. Also, such pre-stretched pulses can help to short the length of dispersive fibre under the same level of stretched ratio.

b) Spectral 3dB bandwidth should be larger than 20 nm in order to obtain compressed pulse-width of sub-300 fs (assume Gauss-shape) and then to achieve high peak power.

c) High pulse energy at least to be ~nJ level in order to reduce the number of pre-amplifier stages.

d) The seed ML source should be self-starting, long-term stable operation and full fibre-rized to satisfy the system stability, compactness for industrial utilization.

Cavity dispersion management is of critical importance for ultrashort pulse generation. In general, a fibre cavity with negative dispersion can generate soliton pulses, due to the balance of negative dispersion and self-phase modulation. Soliton duration is typically determined

by the cavity dispersion such that $\tau \propto |GDD|^{1/2}$ [1]. Pulses as short as 58 fs at 1.9 μm have been obtained by designing a short fiber cavity with only −0.017 ps^2 GDD [2]. However, bulk optics is employed in this cavity, eliminating the advantage offered by the all-fibre configuration. To date, the shortest soliton duration reported from an all-fibre Tm-doped oscillator is 190 fs [3], however, with a limited (20 pJ) pulse energy. An effective way to generate shorter pulses with moderate pulse energy is to utilize intracavity dispersion management that typically set total cavity slightly normal [4].

Dispersion management technology has been employed in many reports on all-fiber, ultrashort Tm-doped oscillators [4-9]. For example, Sobon et al. used the NPR technique to directly generate dissipative solitons with >100 nm bandwidth [5]. Ref. [6] used a chirped Bragg fiber grating to manage dispersion, both soliton and dissipative soliton regimes can be achieved in a semiconductor saturable absorber mirror (SESAM)-based Tm oscillator. Ref. [7] reported the highest single pulse energy (4.9 nJ) from an Tm-doped all-fibre laser cavity at dissipative soliton regime by SESAM. To date, the shortest pulse directly generated from an all-fibre Tm-doped oscillator is 140 fs, mode-locked by SESAM [8]. Not only the mentioned above SESAM material based saturable absorber, another effective technique to achieve the mode-locking is to use carbon nanotube (CNT). Dissipative soliton in normal dispersion produced by CNT had pulse-width of 2.3 ps and energy of 0.45 nJ [9]. Ref. [4] report an oscillator operates in slightly normal cavity dispersion at 0.055 ps^2 and delivered 152 fs pulses with 52.8 nm bandwidth and 0.19 nJ pulse energy from Tm-doped all-fibre laser based on CNT.

In this chapter, I describe the development of the dissipative soliton mode-locked fibre laser based on a carbon nanotube. The oscillator produced stable 21 ps pulses at a repetition frequency of 9.09 MHz with a 3 dB spectral bandwidth of 18.6 nm. The results obtained through numerical modelling agreed well with the experimental findings and this could therefore be a good candidate for the intended CPA system. Unfortunately, the CNT used in the oscillator deteriorated over time and was unable to produce self-starting and stable mode-lock pulses.

Section 3.3 describes a mode-locked laser based on nonlinear polarisation rotation which generated 1945 nm, 5.5 nm bandwidth and 850 fs conventional soliton pulse. The pulses with strong Kelly sidebands were not suitable for the future CPA system however. In

addition, with the insertion of dispersion compensation fibres for the generation of dispersion-managed pulses it became difficult to start mode-locking in the NPR mechanism.

Section 3.4 and section 3.5 use commercial SESAM inside the cavity in order to generate dispersion-managed pulses as an intended seed source for the future CPA system. In section 3.4 the oscillator could only generate noise-like soliton pulses that lasted a nanosecond, which were not suitable for the CPA system. After replacing the SESAM with a new and different one and then optimising the cavity, I obtained a self-started dissipative soliton pulse at a central wavelength of 1925 nm and a 3 dB bandwidth of 40 nm at a repetition rate of 15.6 MHz. Benefitting from a broad bandwidth (40 nm), the pulses from the oscillator were able to be compressed through a grating pair to 280 fs. This pulse was thus deemed to be qualified to work as a seed source for amplification in the future CPA system.

Section 3.5 summarises this chapter and gives a concluding remark. The work described in this chapter has previously been published as part of Chapter 4.

3.2 Theory of the mode-locked fibre laser

3.2.1 Mechanism

Considering a laser oscillating on a fairly large number of longitudinal modes. Under normal conditions, the phase of these modes will have arbitrary values and in continuous wave operation, the intensity will demonstrate a random time behaviour. If we now assume that the lasing modes have equivalent or practically identical amplitudes, and by some means are made to oscillate with a fixed phase difference then such a laser can be called as mode locked laser, and the procedure by which the modes are made to operate in this manner is mode locking.

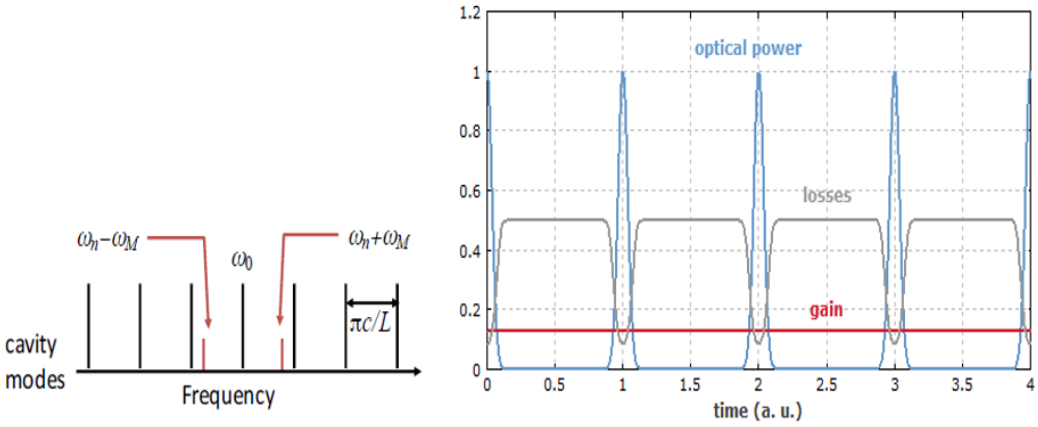

Fig. 3.2.1. Laser modes structure (left) and temporal evolution of optical power and losses in a passively mode-locked laser with a fast saturable absorber (right) [9].

Considering this in the frequency domain as shown in Fig. 3.2.1 (left), if a mode has optical frequency ω_0 and is amplitude-modulated, the resulting signal will have sidebands at optical frequencies $\omega_0-\omega_M$ and $\omega_0+\omega_M$. If we make sure that the modulated spacing is the same as the cavity-mode spacing, the central mode and the adjacent modes will be phase-locked together thus generating mode locked pulses.

In the time domain, a cavity can be considered of having a saturable absorber (SA) which exhibits an intensity-dependent transmission, which means that light will be selectively transmitted based on its intensity. For example, when an optical pulse incident upon a SA, the SA's transmission increases where the pulse intensity is higher thus reducing the cavity losses and sustain a short optical pulse. As shown in Fig. 3.2.1 (right), for the high intensity light, the laser gain can be sufficient for compensating the losses for the circulating pulse, while losses can be significantly higher for low intensity light resulting in an increasingly shorter optical pulses after each round trip [10].

3.2.2 Saturable absorber

Saturable absorbers have the nonlinear property of transmitting higher intensity light more than lower intensity light, which have transmission curve of:

$$T(I) = 1 - \Delta T \cdot \exp\left(\frac{-I}{I_{sat}}\right) - \alpha_{ns} \qquad (3.1)$$

where T(I) is the transmission, ΔT is the modulation depth, I is the input pulse energy, I_{sat} is the saturation energy, and α_{ns} is the non-saturable loss. The Fig. 3.2.2 gives a plot of calculated transmission function for the saturable absorber used in this thesis (Batop SAM-1960-54-10ps: ΔT=30%, I_{sat}=35 μJ/cm^2, α_{ns}=24%) by using eq. 3.1.

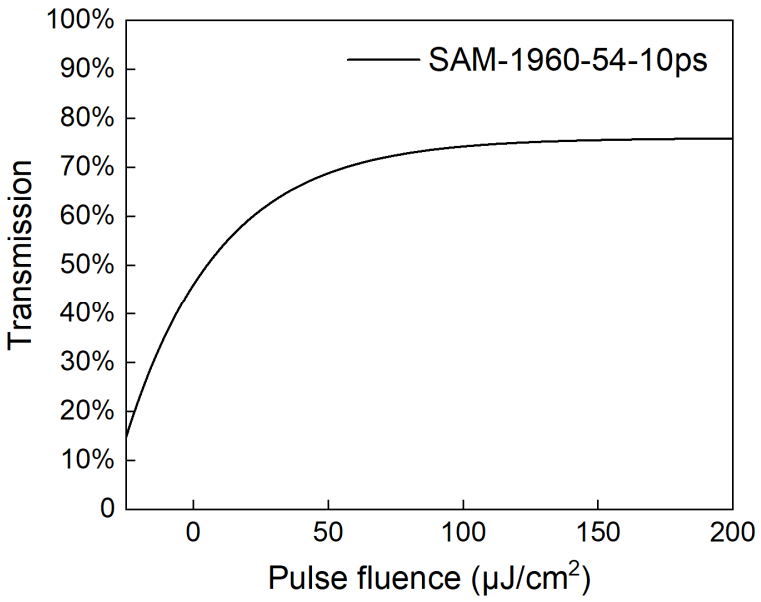

Fig.3.2.2. Calculated transmission curve of the Batop SAM-1960-54-10ps used in this thesis.

The saturable absorber helps to select the pulse from the noisy background and gradually build up the pulse through many round trips SA promotes pulse formation by preferentially transmitting higher intensity light, enabling high intensity fluctuations to be boosted above the background noise level. Thus, a short pulse could produce a modulation of loss because the high intensity at the peak of the pulse saturates the absorber more strongly than its low intensity wings as shown in the Fig. 3.2.3.

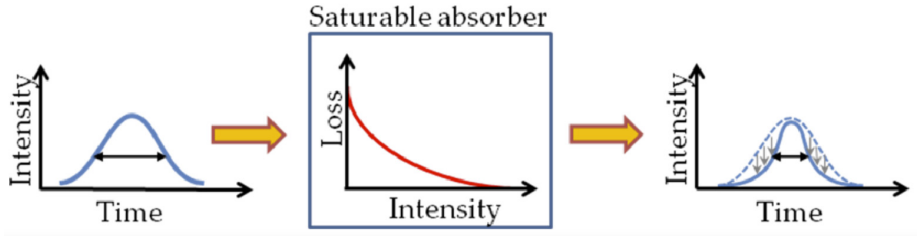

Fig. 3.2.3. Typical pulse shaping through the saturable absorber [11].

Saturable absorbers are critically important for passively mode-locked lasers. There are two categories of SAs used in lasers, the material-based SAs and the articial SAs. The former include semiconductor saturable absorber mirrors, carbon nanotubes and some other 2-dimensional materials. The articial SAs include Kerr-lens, nonlinear polarization rotation and nonlinear amplifying loop mirror. In the following subsections, I mainly introduce typical three types SAs which are used in this thesis – nonlinear polarization rotation, semiconductor saturable absorber mirrors and carbon nanotubes.

3.2.2.1 Nonlinear Polarization Rotation (NPR)

The nonlinear polarization rotation (NPR) mode locking technique is one of the general methods for mode-locked fibre laser and it was first used for fibre lasers in 1992 by Optoelectronics Research Centre (ORC) in Southampton [12,13]. For the NPR, because the nonlinear effects in term of self-phase modulation (SPM) and cross-phase modulation (XPM) effects, the electric fields of different intensity of pluses will have different nonlinear phase shifts.

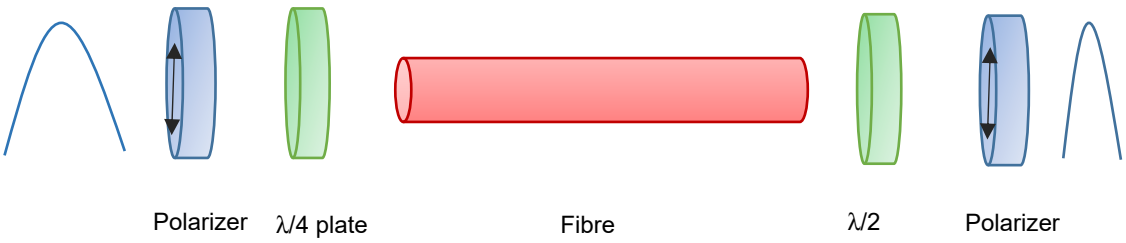

Fig.3.2.4 The basic structure of the NPR.

As the Fig.3.2.4 showing the principle of the NPR. The pulse through the first polarizer becomes to be a linear polarized light. Then, the linear polarized light will become into ellipse polarized light after the quarter wave plate. In the optical fibre, the ellipse polarized light can be divided into two mutually perpendicular linear polarized light, assuming they are A_x and A_y light. When the two linear polarized beams of A_x and A_y transmission in the fibre, because the nonlinear effects from SPM and XPM phenomenon, the A_x and A_y polarization direction are accumulated different nonlinear phase shift. At the output end, the pulse is the synthesis of A_x and A_y which has different accumulated nonlinear phase shift. Through regulating the half wave plates at the end of fibre, achieving the different power of pulse has difference loss when through the second polarizer. Finally, this will be worked as a fast artificial saturable absorber for intensity nonlinear modulation.

3.2.2.2 Semiconductor saturable absorber mirror (SESAM)

A typical semiconductor saturable absorber structure is shown in Fig. 3.2.5. A semiconductor heterostruture (here AlAs/GaAs) is grown on a GaAs-Wafer (20-40 pairs). The layer thicknesses are chosen to be quarter wave at the centre wavelength at which the laser operates. These structures act as quarter-wave Bragg mirror. On top of the Bragg mirror, a half-wave thick layer of the low index material (here AlAs) is grown, which has a field-maximum in its centre. At the field maximum, either a bulk layer of a compound semiconductor or a single-or multiple Quantum Well (MQW) structure is embedded, which acts as a saturable absorber for the operating wavelength of the laser [14].

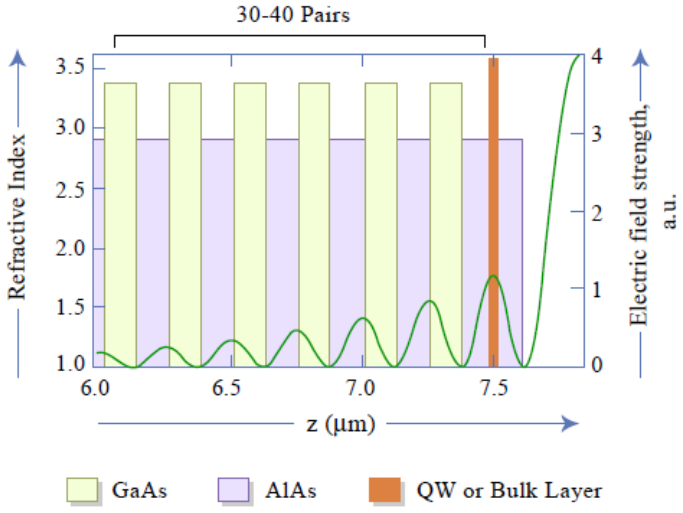

Fig. 3.2.5. Typical structure of the SESAM [2].

SESAM has been developed for many years and are widely used in fiber lasers system (Yb, Er, Tm). There are commercially available with different modulation depths and fast response times. Batop is one of the SESAM companies where details and reviews of SESAM could be found in their website. SESAMs have the advantage of simple implementation, but they are relative expensive and subject to damage at high powers and with extended use. In addition, it has fixed modulation depth and therefore will allow limited accessible modes.

3.2.2.3 Carbon nanotubes (CNTs)

Single-walled nanotubes (SWNTs) is a simple, cost-effective alternative saturable absorber [12], where the operating wavelength is controlled by the diameter of the nanotubes.

Wideband tunable range is possible utilizing a SWNT with a large diameter distribution. Whereas at some specific wavelengths, where SWNTs are not in resonance could not be useful and may even produce detrimental losses [15]. Recently, SAs based on single-walled carbon nanotubes (SWCNTs) are widely used to realise mode-lock pulses [16,17]. The advantages of CNT amongst others is a relatively simple fabrication process, short recovery time (smaller than 1 picosecond) and ideal modulation depths. Several SWCNT SAs have been reported for mode locked lasers at wavelength regions of 1 μm, 1.55 μm [18] and 1.9 μm [19]. Also, during the manufacturing process, the working characteristics of a CNT absorber can be set because SWCNTs' absorption parameters are decided by the diameter and details of the structure [20].

CNT absorbers can be used either in transmission or reflection modes and thus find applications both in ring and linear cavity structures. Generally, CNTs have been embedded into polymers and therefore the selection of polymers plays significant role for the characteristics of SAs. The CNTs combined with the polymer material can then be used on the surface of optical fibres or a quartz glass substrate for the generation of mode locked ring cavity laser [20]. Recently, a single step dry transfer thermo-compression method which helps to place SWCNTs on a polymer film has been proved. Compared with the conventional wet deposition methods, this method is more effective. However, polymer is an undesirable host material for CNTs since it possesses relatively lower damage threshold and higher optical absorption. Therefore, in order to work at high power and in the mid-IR region, it is appropriate to find new techniques to develop CNT absorbers rather than rely on polymer.

A technique using carboxymetyl cellulose (CMC) to be a host polymer for carbon nanotubes was reported [19]. It benefits from a surfactant with a high nanotube dispersion and forming a film after the drying up of suspension. Carbon nanotubes integrated through the arc-discharge method shift absorption band to longer wavelengths (e.g. mid-IR region) than those nanotubes integrated by other techniques, such as the laser ablation and the high-pressure decomposition of CO gas.

Depending on the diameter of the nanotube, they can work as saturable absorbers at a large range of wavelengths. There are many ways to a fiber formatted make SWCNT SAs in a fiber format, including depositing the carbon nanotubes on the end of the fiber and or around

a tapered fiber. The technology of making a robust, high power SWCNT is still under development. SWCNTs can not tolerate long time operation due to optical bleaching and its physical strength is another challenge. The Table. 3.2.1 gives information that the evaluation of three types of SAs in the laser operation used in this thesis.

Table. 3.2.1. Typical features of three types of saturable absorber.

Saturable absorber	Modulation depth	relaxation time	Insertion loss	Operation bandwidth	Damage threshold
NPR	Up to 50%	0 ps	0.5 dB	1 μm	2 J/cm^2
SESAM	Up to 50%	1~15 ps	3 dB	< 0.2 μm	1 mJ/cm^2
CNT	Up to 10%	< 1 ps	3 dB	0.7 ~ 2.4 μm	0.1 mJ/cm^2

3.2.3 Mode-locking pulses generation

3.2.3.1 Soliton fibre lasers

The term soliton was proposed in 1965, and it reflects particles with solitary wave properties that remain intact even after colliding with each other [21]. In the context of optical fibre, it was first proposed to use soliton for optical communication in 1973 [22]. Solitons are NLSE solutions used to simulate conservative systems (loss/no gain), such as pulse propagation in passive optical fibres. In 1984, Mollenauer proved the first soliton laser through experiments using anomalous dispersion fibres [23]. Up to now, the soliton mode (Fig. 3.2.6) is the most common pulse formation through the mode-locked fibre lasers. Generally, the temporal and spectral profile of an ultra-short pulse changes because of chirps caused by nonlinear effects (Self phase modulation) and group velocity dispersion (GVD). However, under special condition, the phase shift caused by self-phase modulation (SPM) and anomalous dispersion in fibre laser can be exactly balanced between each other so as to remain stable pulses shape for a long propagation distance.

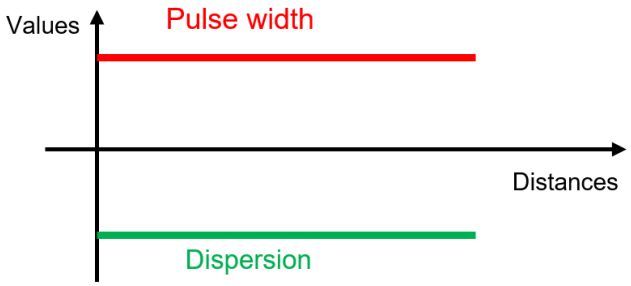

Fig. 3.2.6. Soliton pulse evolutions with distance.

The soliton pulses have $sech^2$ shape which can be expressed by Fig. 3.2.7, which result from a fundamental balance between the linear dispersion and the cubic nonlinearity:

$$\mathrm{P(t)} = P_p \, sech^2\left(\frac{t}{\tau}\right) \qquad (3.2.2)$$

Where 'P_p' is peak power and 'τ' is soliton pulse duration. And for the transform limited soliton pulse, the time–bandwidth product ($\tau\Delta\nu$) is about '0.315'.

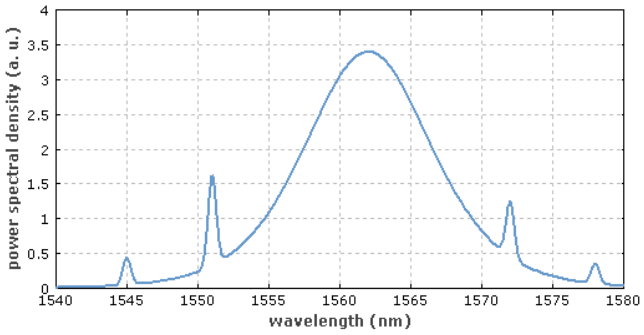

Fig. 3.2.7. Optical spectrum of the output of a soliton fibre laser, exhibiting Kelly sidebands [25].

For soliton pulses in the fibre, the nonlinear phase shift in one round-trip is determined by the pulse energy and width, which means that in order to form a stable soliton pulse, the pulses maximal energy is limited for a fixed pulse width, this is because nonlinear phase shifts have a range for stable soliton pulse generation [24]. Another limitation for mode-locked fibre laser is the Kelly sidebands (Fig. 3.2.7) which is very often in the fibre lasers [25]. Kelly sidebands comes from the soliton pulses' energy coupled into the concomitant discrete waves in resonance. If the power of discrete waves attaches at the lasing threshold value, it would deplete the gain of the laser so as to subsequently making mode locking to

be unstable [26]. In conjunction with the soliton area theorem, this also limits pulse energies, leading to typical performances of ~100 pJ and ~200 fs.

3.2.3.2 Dispersion management fibre lasers

A dispersion-management soliton is also called a stretched pulse. The stretched pulse fibre laser gets its name because as it circulates in the cavity the pulse is temporarily stretched and then compressed twice. As shown in Fig. 3.2.8, normal and anomalous dispersion is embedded through the dispersion compensation fibre (DCF) and normal single mode fibres (SMFs) in order to periodically stretch and compress the pulse width. Therefore, the average pulse width is much larger, by at least one order of magnitudes, than the soliton mode in one round trip. As previously mentioned, this characteristic can reduce the peak power of the pulses and thus decrease the nonlinear phase shift by a higher pulse intensity. Finally, this means that the cavity could offer a higher pulse energy, offering roughly more than 10 times the energy than the soliton pulses when under stable operation [27, 28]. Dissimilarly to soliton fibre lasers, the output spectrum can be broader than the gain spectrum, and due to decreased phase-match coupling, the stretched-pulse spectral does not have sidebands. There was also a master equation for the operation of the dispersion managed soliton [29]. I addition, it should be noted that the pulse produced by the dispersion-managed laser is the solution of the master equation and is usually more consistent with the Gaussian shape.

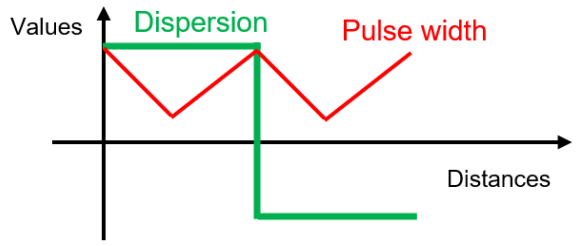

Fig. 3.2.8. Dispersion management pulse evolutions with distances.

Temporal breathing reduces the roundtrip nonlinearity compared to a static solution of the same energy, allowing more energetic pulses than a comparable soliton laser. The dispersion map suppresses sideband generation and resonant instabilities. Output pulses may be somewhat up- or down-chirped, depending on the placement of the output coupler, but may be dechirped to <100 fs outside the cavity with energies of ~2 nJ.

3.2.3.3 Dissipative soliton fibre lasers

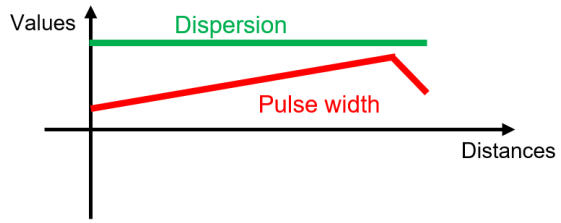

Fig. 3.2.9. Dissipative soliton pulse evolutions with distances.

Dissipative soliton (DS) fibre lasers (Fig. 3.2.9) are seen as an alternative oscillator that could be used to overcome the limitations on the duration and energy of the conventional soliton (CS). The formation of DS in laser oscillators demands two more balanced terms than CS, including gain and loss, as shown in Fig. 3.2.10 [30]. This name for the dissipative soliton comes from the fact that, when compared with CS mode-locking – which has dispersion and nonlinearity items –, the gain and loss (dissipative process) play an important role in mode-locking. In general, DS fibre lasers require an all-normal dispersion cavity or net normal dispersion cavity. This is difficult for a longer wavelength however, as it is hard to fabricate the normal dispersion fibres at a long wavelength. Therefore, in most cases, the actual DS fibre lasers work with dissipative dispersion - managed (DDM) soliton fibre laser [31].

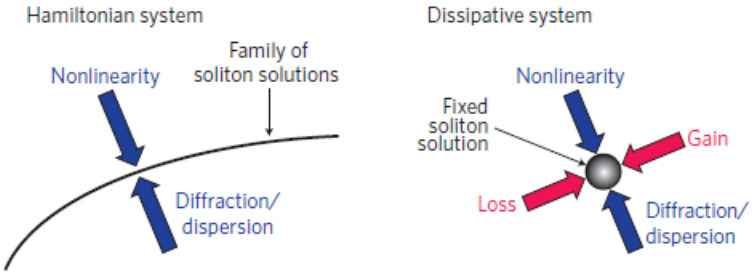

Fig. 3.2.10. Qualitative differences between the solitons in Hamiltonian and dissipative systems [28].

The analytical solution of the cubic-quintic Ginzburg-Landau equation (CQGLE) can model a pulse formation of the dissipative soliton resonance (DSR) by using [32,33]:

$$U_z = gU + \left(\frac{1}{\Omega} - \mathrm{i}\frac{D}{2}\right)U_{tt} + (\alpha + \mathrm{i}y)|U|^2U + \gamma|U|^4\,U \qquad (3.2.3)$$

where ‘U’ is the electric field envelope, ‘z’ is the propagation coordinate, ‘t’ is the retarded time, ‘D’ is the GVD, ‘g’ is the net gain and loss, ‘Ω’ is related to the filter bandwidth, ‘α’ is a cubic saturable absorber term, ‘δ’ is the quintic saturable absorber term, and ‘γ’ refers to the cubic refractive nonlinearity of the medium.

During pulse shaping in normal-dispersion fibre lasers the output spectrum shows features of steep spectral edges and a flat top profile, which is attributed to the spectral filtering of highly-chirped pulses [32,34]. So long as there is an upper energy limit for the dissipative soliton with maximal accumulated phase shift of 10π, with the increase of pump power, the pulse width can be arbitrarily broad while still maintaining its amplitude constant [35].

3.2.3.4 Noise like pulse

The first description of noise-like pulse (NLP) in a passive mode-locking fibre laser started to appear in the literature in early 1990s [36], and a detailed investigation of their characteristics was first carried out in 1997 [37]. Around that time, fibre-based NLPs started to receive a considerable amount of research attention because of their distinctive, extraordinary features contrasted with ordinarily mode-locked laser pulses. The early results reported mainly on the various typical characteristics of NLPs for different cavity configurations, including anomalous and normal dispersion regimes, and also focused on describing the interrelationship between the specific NLP characteristics and the corresponding cavity configurations.

Tang et al. have numerically shown that in the case of a laser cavity with net anomalous dispersion, the formation of NLPs is caused by the combined effect of soliton collapse and positive cavity feedback [38]. On the other hand, there have been far fewer reports on the generation of NLPs in cavities exploiting novel material-based SAs, e.g., semiconductor, carbon nanotube, or graphene SAs [39]. For example, in ref [39] a single-wall carbon nanotube was utilized as a SA in a ring cavity configuration with large net normal dispersion (NND), generating DSs or NLPs. In particular, the NLPs were generated when the cavity operated with high pump powers, i.e., the SA was oversaturated and could not provide sufficient pulse stabilization [40]. In addition, it should be noted that the linear loss for this cavity configuration was also relatively high due to the inclusion of a 3-dB output coupler in the cavity. Increments in the intra-cavity gain, e.g., increasing pulse energy, can lead to oversaturation of the SA or to excessive nonlinear phase shifts. Any of these two situations

may as well disturb the stability of the pulse, either by allowing the growth of dispersive waves or background noises to break into the opening time window of the SA or by forcing the pulse to split via too strong SPM [40].

The noise-like pulse (NLP) is observed typically in relatively long or highly pumped fibre laser cavities for a different types of lasers in terms of cavity structures, dispersion regimes and operating wavelengths. Such pulses have properties e.g. high energy, wide optical bandwidth and short coherence time, hence make them useful for several important applications including supercontinuum generation, sensing, micromachining and so on. Average powers up to the watt range directly at the laser output are readily achievable. Using an all-fiber master oscillator power amplifier (MOPA) configuration, NLP energies of a few tens of micro-jouls and peak powers up to one third of a megawatt have been achieved recently. Despite the complexity and variability of their fine structure, generally the NLPs display a very simple and stable overall behaviour. In particular, a stable, wide and smooth, structureless optical spectrum and a double-scaled autocorrelation, with a narrow coherence peak riding a wide pedestal are the identifying signatures of this regime. In addition, the energy of the bunch and its total duration are also relatively stable for given cavity settings. The Table. 3.2.2 gives information that the typical characterizations for four types of mode-locked pulses mentioned above.

Table. 3.2.2. Typical characterizations for four types of mode-locked pulses

	Pulse energy	Output pulse-width	Achievable compressed pulse-width
Soliton	~0.1 nJ	~ps or sub-ps level	~ps or sub-ps level
Dispersion-Managed Soliton	Up to 2 nJ	~ps level	~100 fs
Dissipative Soliton	Up to 20 nJ	~10 ps level	~200 fs
Noise-like pulse	~μJ level	~1 ns level	~1 ns level

3.3 Numerical simulation

I performed numerical simulations of the oscillator using the commercial software of "RP FIBER POWER" with split-step-Fourier algorithm before the experiment to help to investigate the basic cavity design. The simulation software includes the Kerr nonlinearity and second order dispersion with actual fibre parameters and spectroscopy. However, there is only one polarization direction during light propagation in the fibre hence the influence of polarization cannot be considered. Also, the saturated absorbers (SAs) which will be used in the mode-locked lasers cannot be sufficiently simulated in terms of modulation depth. This is because the parameters can be set for SAs are saturated power, recover time and saturated transmission for pulses in the RP Fiber Power. The oscillator is seeded with a preset initial pulse (picosecond or femtosecond), but for given cavity parameters the simulations always converge to the same solution.

The simulation configuration of the oscillator is schematically illustrated in Fig. 3.3.1 using the accurate fibre parameters shown in Table 3.3.1. The laser operates in the slightly net-normal-dispersion regime to generate dissipative soliton pulses in order to satisfy the CPA seed source requirement in the section of the 3.1. A ring oscillator allows more design freedom to control the propagation compared to a linear oscillator. The single mode fiber (SMF), DCF and Tm-doped fibre complete the dispersion map. The use of spectral filters is important in the simulation to form dissipative soliton.

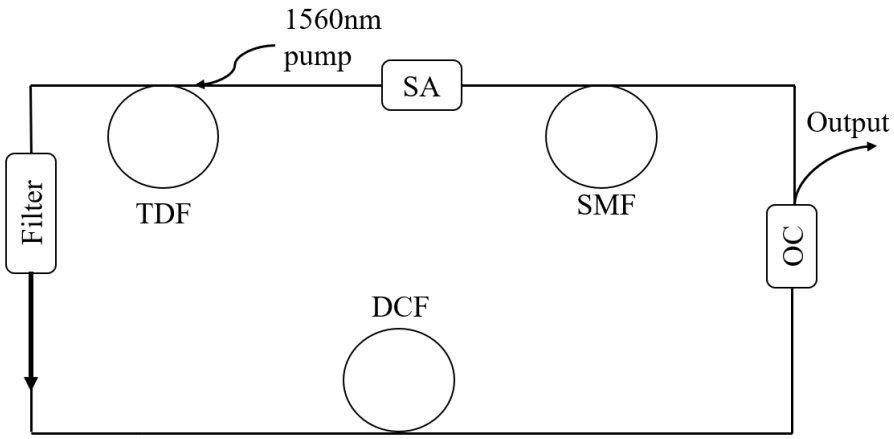

Fig.3.3.1 Modeling cavity structure for mode-locked fibre laser. SMF:single mode fibre; TDF: thulium doped fibre; SA: saturable absorber; DCF: dispersion compensation fibre; OC: output coupler.

Table. 3.3.1. Components' parameters used in modeling.

Segments	Length (m)	BW (nm)	WL (nm)	GVD (ps^2/m)	MFD (μm)	Loss (ratio)
SA			1960			0.4
Filter (Gaussian)		50	1960			
SMF	8			-0.067	9	
TDF	3			-0.02	5	
DCF	7.7			0.09	5	
OC						0.6

The cavity has net dispersion of 0.097 ps^2. A typical and stable dissipative solution with pulse energy of 1 nJ is obtained when available pump power (140 mW) is set and its pulsing and spectral evolutions are shown in Fig. 3.3.2. The pulse dynamic evolution indicates that the the joint effects of normal group velocity dispersion (GVD) and nonlinearity (NL) in DCF, the pulse propagates with its duration increasing monotonically. The broadened pulse is then compressed by the SMF and TDF segments with anomalous GVD. The 3dB spectral bandwidth of the pulse with steep edges as shown in Fig.3.3.2(right) is nearly constant around 19.6 nm during its circling in the cavity. The modeling results (Fig.3.3.3.) predicted the oscillator output spectral bandwidth increase as the cavity net dispersion is slight positive and close to zero, which agree with the experimental results in [41]. This can be explained by the lower value of the net dispersion with shorter intra-cavity pulse-width has stronger nonlinearity (SPM) so as to form spectral broadening. The result provides an indication that in order to obtain pulses with broaden spectral bandwidth which have shorter transform-limited pulse-width, the cavity should be located in slightly normal dispersion closed to zero region. The following experiments of the cavity building were performed with guidance from this simulation in terms of fiber length, net dispersion value region, output coupler position etc.

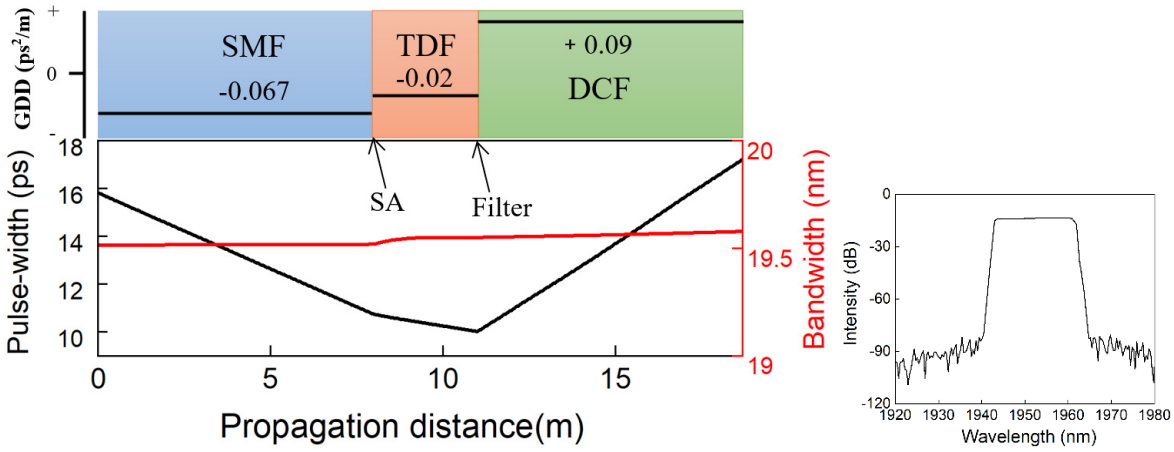

Fig.3.3.2. Intracavity dynamic of pulse duration (black line) and spectral bandwidth (red line) evolution. right: Spectrum of the modeling dissipative soliton output pulses.

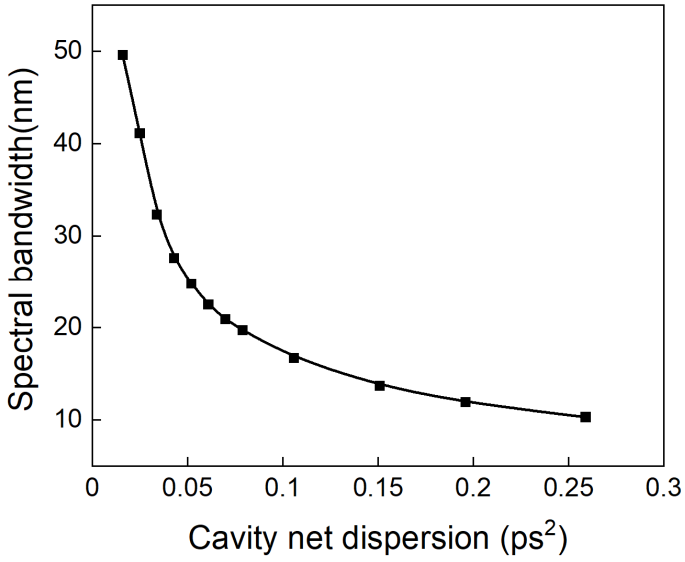

Fig.3.3.3. The simulated dissipative soliton spectral bandwidth as the normal net cavity dispersion increase.

3.4 Mode-locked fibre laser based on NPR

Among varieties of mode-locking techniques, firstly I explore the NPR as an artificial saturable absorber to build Tm-doped mode-locked fibre laser. The target of the sub-section is to demonstrate weather such simple, high physical strength mode-locking technique is able to play a role of the ideal seed source in a high performance CPA system. Initially, I investigate the simple, conventional soliton cavity with anomalous dispersion to verify the possibility of NPR technique for mode-locking generation. After that, a dispersion-

management of the cavity will be explored by insertion of dispersion compensation fibres based on anomalous dispersion soliton cavity.

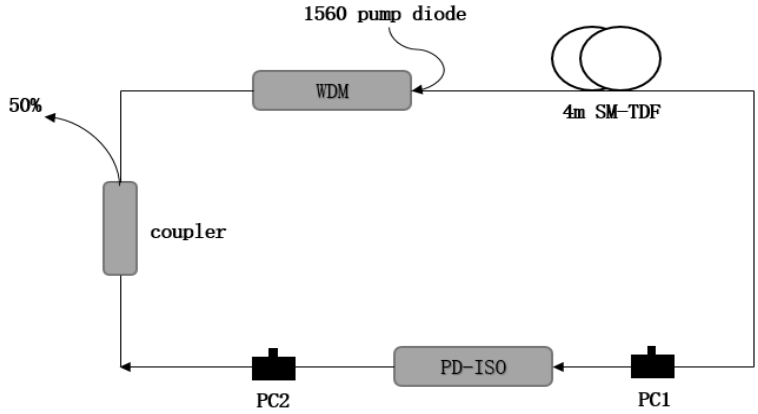

Fig. 3.4.1. Schematic of the mode-locked fibre laser based on NPR. SM-TDF:single mode thulium doped fibre; WDM: wavelength division multiplexing; PC: polarization controller; PD-ISO: polarization dependent isolator.

The schematic of the mode-locked all-fibre ring laser based on NPR technique is shown in Fig.3.4.1. A 4 m of OFS thulium doped fibres (OFS Tmdf200) and sections of SM-28 fibre forms the ring cavity. The 1550 nm/1960 nm wavelength division multiplexing (WDM) is used to launch the output of a 1560 nm pump laser diode into the laser cavity. Unidirectional operation and polarization selectivity are provided by the polarization-dependent isolator (PD-ISO) The PM isolator is designed to block the fast axis and only pass light along the slow axis. Two PCs are employed to adjust the polarization states of the circulating light in the cavity. The output is taken by a 50% fibre pigtailed coupler. The total cavity length and net dispersion is 8.3 m and -0.37 ps^2 respectively. For the measurements of pulse characteristics, I used an Agilent digital storage Oscilloscope with 200 MHz bandwidth to observe the rough stability of the mode-locked pulse and the pulse repetition rate. For the pulse spectra, I utilized Yokogawa AQ6375B long wavelength Optical Spectrum Analyzer. In order to measure pulsewidth, an A.P.E autocorrelator (Pulse-Check) is used. The single mode pump laser diode is temperature stabilized to ensure the stability of mode-locking operation.

The mode-locking threshold was about 102 mW. When the pump power was increased above threshold and by properly adjusting the PCs, the fibre laser could be mode-locked easily. If the orientations of the PCs are not disturbed, the self-started mode locking operation

could be attained by simply increasing the pump power to above threshold. Once mode-locked, the mode locking state could be sustained even if the launched pump power decreased to about 90 mW.

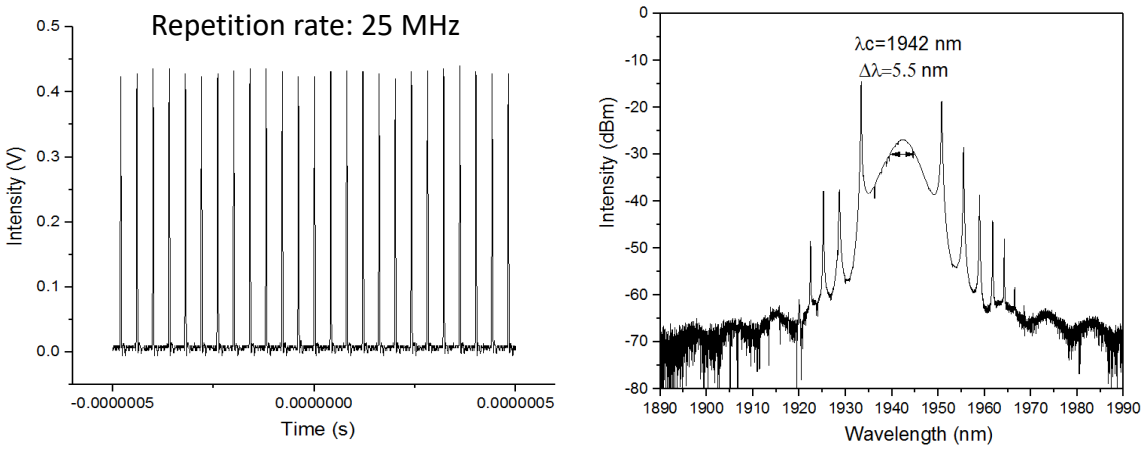

Fig. 3.4.2. (left) Oscillator scope trace of the soliton pulses by NPR. (right) Spectrum of the soliton pulse by NPR.

The typical mode locking pulse-train is illustrated in Fig. 3.4.2 (left) when the pump power is 100 mW. The fundamental pulse repetition rate of the fibre laser was 25 MHz corresponding to a cavity round trip time of about 40 ns that match well with the cavity length. Fig. 3.4.2 (right) shows the spectrum of the conventional soliton pulse with symmetrical Kelly sidebands with a calculated anomalous dispersion of -0.38 ps^2. The output pulse with 3 mW average output power and 120 W peak power has a central wavelength of 1942 and a bandwidth of $\Delta\lambda$=5.5 nm. Fig. 3.4.3 illustrates the autocorrelation trace of the mode-locked pulse. The pulse duration is measured to be 0.85 ps corresponding to a time-bandwidth product of 0.37 which is slightly higher than the Hyperbolic-secant pulse (0.315). This difference may have caused by the 1.5 meters of SM-28 fibre used after the output coupler. The peaks of the Kelly sidebands are higher than that main peak of the mode-lock laser. This may result in the Kelly sidebands to be amplified more than the desired peak compromising the performance of the CPA system. I verify that the NPR technique based on fiber PM-isolator can be used to generate soliton mode-locked pulses and the next step is to investigate the performance of the dispersion management cavity by inserting DCF based on previous conventional soliton oscillator.

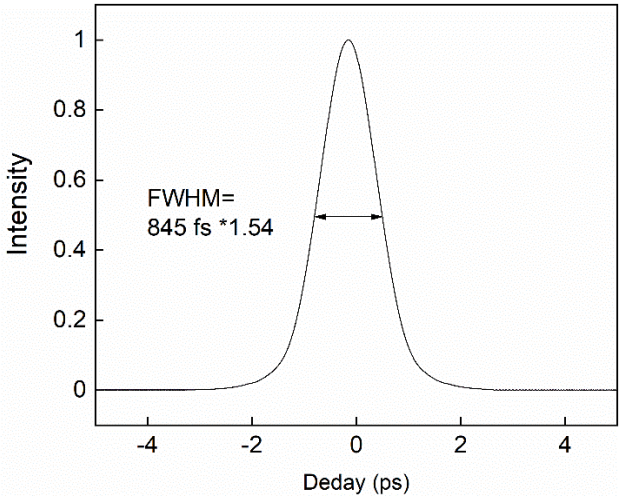

Fig. 3.4.3. Measured autocorrelator trace of the soliton pulse by NPR.

However, it proved difficult to achieve mode-locking pulses generation when several meters of dispersion compensation fibres were inserted into the cavity. I think this is because the filter function of the PM-isolator is too narrow to stabilize and form mode-locking generation for the chirped pulses circulation when add DCF. Therefore, it was necessary to utilize material saturable absorbers e.g. CNT and SESAM to build a stable dispersion management mode-locked as a seed for the intended CPA system.

3.5 Mode-locked fibre laser based on CNT

As mentioned in the previous section, the mode-locked conventional soliton pulses that were based on the PM-isolator NPR mechanism were not considered an ideal seed for the following CPA system. In the sub-section, an in-house built dissipative soliton mode-locked fibre laser at 2 μm using carbon nanotubes (CNTs) as a saturable absorber is introduced, which has gained lots of attention because of several advantages such as low cost, broader operation wavelength, easier fabrication process, rapid recovery time and so on.

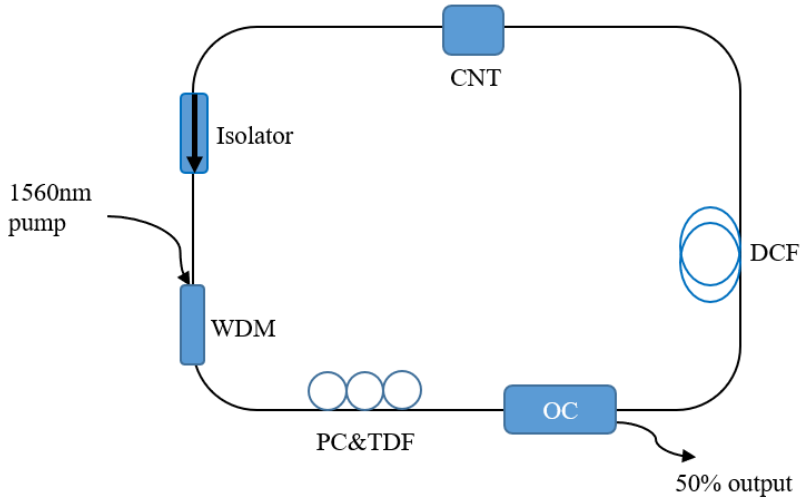

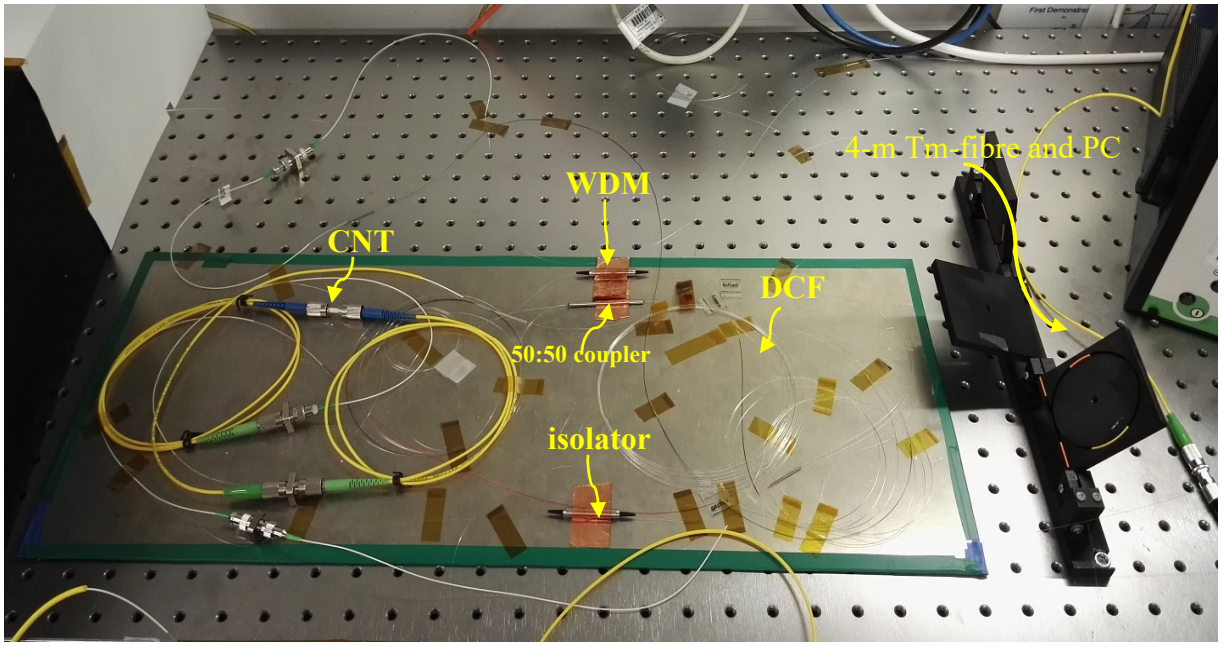

Fig. 3.5.1. Cavity structure for CNT based mode-locked fibre laser. TDF: thulium doped fibre; WDM: wavelength-division multiplexer; PC: polarisation controller; OC: output coupler; DCF: dispersion compensation fibre; CNT: carbon nanotube.

Fig. 3.5.1 illustrates the ring cavity of the Tm-doped mode-locked fibre laser using a CNT as a saturable absorber. The CNT polymer film is provided and cooperated by [42] has a strong absorption around 1960 nm as shown in Fig. 3.5.2. The highest absorption of CNT with polymer is about 50% at 1960 nm. Given its absorption profile, the CNT is able to act as a filter to help the stability of mode locking. The film is sandwiched between two FC-UPC optical fibre connectors to operate in the transmission regime. 1560nm pump radiation is coupled into a section of single-mode Tm-doped fibre through a 1560/1960 nm wavelength division multiplexed (WDM) coupler. A section of gain fibre is used to build a

polarization controller (PC) by forming an equivalent λ/4 plate, a λ/2 plate and a λ/4 plate which helps to stabilize the mode locking operation. Fifty percent of the power in the cavity is coupled out through a 1960 nm 50/50 coupler. A 10 m of dispersion compensation fibre (DCF) is inserted to manage the total group velocity dispersion (GVD) of the cavity to be net positive dispersion thus generating dissipative soliton.

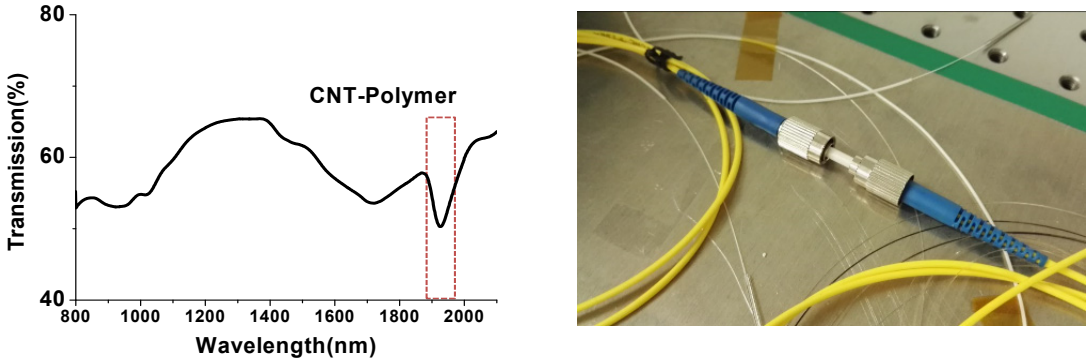

Fig. 3.5.2 Optical transmission spectrum of the CNT [42] incorporated CMC film and its image in the cavity.

Dispersion parameters of the fibres used in the cavity are given below as well as the equipment used to monitor the mode-locked pulses. Dispersions of the single mode fibre (SMF) (Corning, SM-28), DCF (Nufern, UHNA4) and the thulium-doped silica fibre (TDF) are -0.067 ps^2/m, 0.09 ps^2/m and -0.02 ps^2/m respectively at 1960 nm. The thulium doped fibre (OFS, TmDF200) has a peak absorption of 200 dB/m at 790 nm, mode field diameter of 5.0 μm at 1700 nm and the cut-off wavelength of 1350 nm.

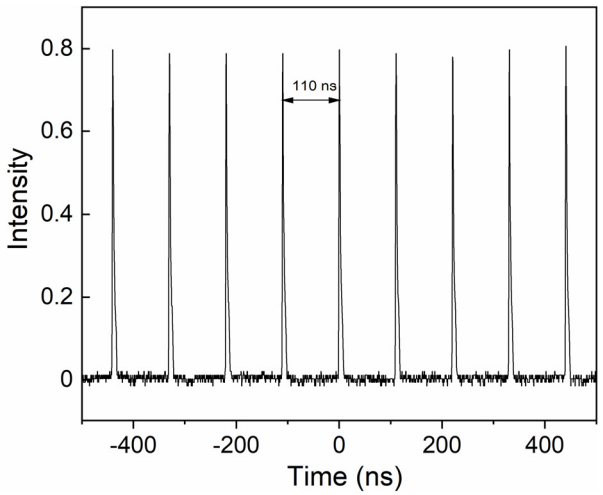

Fig. 3.5.3. Output pulse train with a repetition rate of 9.09 MHz.

When the pump power is ~102 mW, the laser operates in continuous wave (CW) mode. When the pump power is increased to 111 mW, the CW operation disappeared and pulses started to form. When the pump power increased to 150 mW, self-started mode lock pulses are observed. Fig. 3.5.3 shows the output pulse trains with repetition rate of 9.09 MHz which corresponds to the cavity round trip time. The pulse-to-pulse amplitude instability is an artefact of the measurement system and goes away when one or two pairs of pulses are captured.

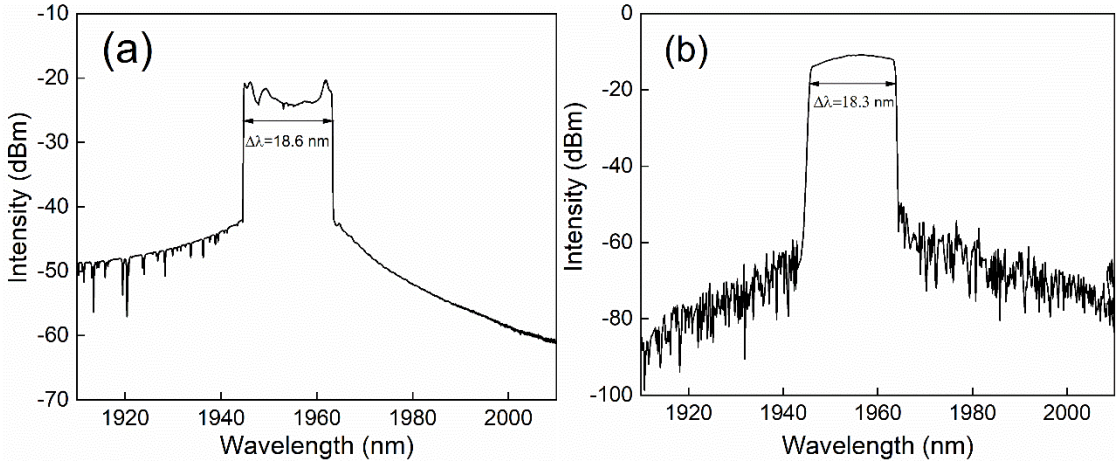

Fig. 3.5.4. (a) Experimental dissipative soliton seeded pulse spectrum with bandwidth 18.6 nm. (b) Simulated dissipative soliton pulse spectrum with bandwidth 18.3 nm.

Fig. 3.5.4. (a) illustrates the dissipative soliton (DS) pulse spectrum when the net cavity dispersion is 0.2 ps^2. Self-started mode locking operation is observed when the pump power was set to 150 mW. The output pulse with 6 mW average output power, pulse energy of 0.66 nJ and 30 W peak power has a central wavelength of 1960 nm. It's steep falling edges clearly indicates that the mode-locked output pulses are DS in nature [43 -45]. Fig. 3.5.4. (b) shows the simulated spectral profile of DS mode with 'RP Fiber Power' with a bandwidth $\Delta\lambda$=18.3 nm. Spectral shape and wavelength range of the simulation result is similar but with more smooth and flatter profile as compared to the experimental results. This is believe to be due to the lack of exact filter function of the CNTs at 1960 nm and disregarding the influence of polarization.

Fig. 3.5.5 (a) illustrates the time trace measured by A.P.E autocorrelator, the FWHM (Full width at half maximum) pulse-width is about 21 ps and the pulse-width is 14.6 if assume Gaussian profile, therefore the calculated time-bandwidth product is 30.5 which means that the output pulse of the mode-locked laser is hugely chirped and can be useful as seed for a

CPA system to decrease the nonlinearity accumulation in the following amplifier. Fig. 3.5.5 (b) shows the simulated pulse profile of the mode-locked laser which is similar in shape and width to that of the measured optical pulse.

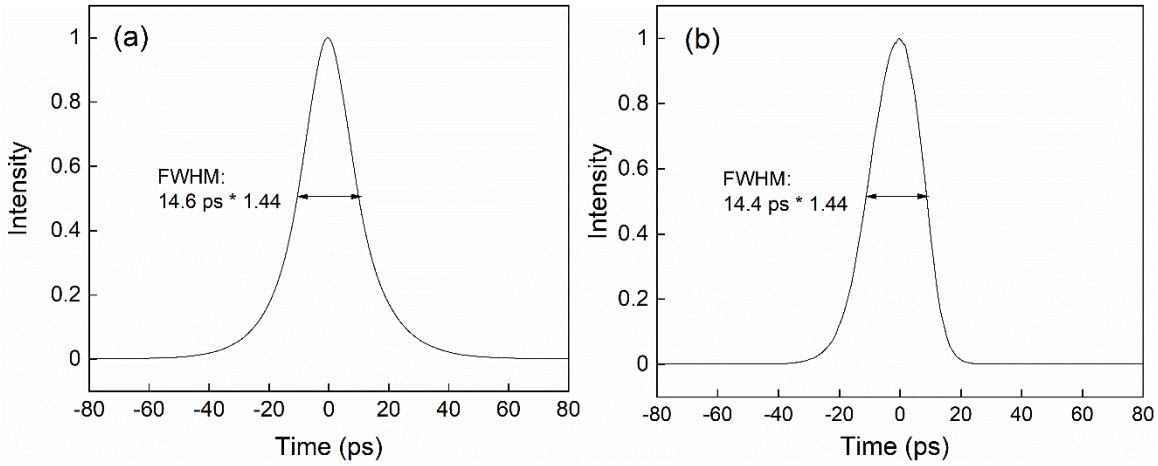

Fig. 3.5.5. (a) Measured autocorrelation trace of the mode-locked laser. (b) Simulated temporal profile of the pulse.

In conclusion, a dissipative soliton mode-lock laser is demonstrated by using a CNT saturable absorber in a ring cavity. The laser produced stable 21 ps pulses at a repetition frequency of 9.09 MHz with a 3 dB spectral bandwidth of 18.6 nm. This pulse can be a good candidate for the intended CPA system.

Unfortunately, the CNT used in the seed laser deteriorated over time (see Fig. 3.5.6) and is unable to produce self-starting and stable mode-lock pulses. The reason of this CNT-polymer damage is relatively low tolerance to optical damage due to the low heat resistance of the polymers, in which CNT was burned by the high optical power during experiment. Therefore, it was necessary to source alternative mature commercially material saturable absorber - SESAM to build a stable mode-locked laser suitable as a seed for the intended CPA system. The next sub-section will explore pulses' characteristics for the mode-locked fibre laser based on SESAM.

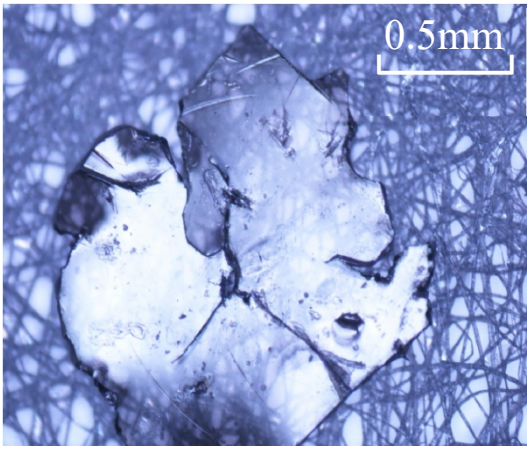

Fig. 3.5.6. The damage (the hole and crack in the middle) under microscope of the CNT with carboxymetyl cellulose

3.6. Mode-locked fibre laser based on SESAM

3.6.1 SESAM1 (low modulation depth)

As the CNT based mode-locked fibre laser presented in the last sub-section was not able to work due to damage of the CNT surface, I explored the other material base mode-locker - semiconductor saturable absorber mirror (SESAM) to produce mode-locked pulses. Thus, I chose a commercial SESAM from Batop in this sub-section. I focused on the experimental realisation of a stable dissipative soliton mode-locked fibre laser with a broad bandwidth and a short transform-limited pulse-width by using a ring cavity configuration.

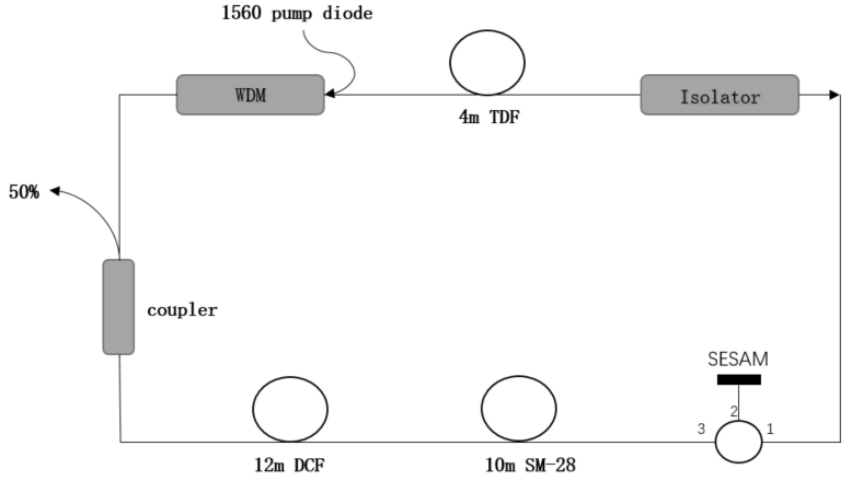

Fig. 3.6.1. The configuration of the mode-locked fibre laser based on SESAM1.

The layout of the laser is shown in Fig. 3.6.1. The ring cavity of the oscillator consists of a 4 m long thulium doped single-clad fibre (OFS-TmDF200) with a mode-field diameter (MFD) of 5 μm at 1700 nm and a numerical aperture (NA) of 0.26 which is core-pumped via a 1550/1960 nm wavelength-division multiplexer (WDM) by an commercial laser diode operating at a wavelength of 1560 nm. Mode-locking is initiated and stabilized by a commercially available semiconductor saturable absorber mirror (SESAM) with a modulation depth of 10% and a saturation energy of 35 μJ/cm^2 (Batop, SAM-1960-18-10ps). It is worth to mention that the parameters of the SESAM were provided by Batop officially. A 50/50-fused fibre coupler is used as an output coupler. The total length of fibre component pigtails used in the cavity is amounted to 4 m. A 10 m of SM-28 fibre and 12 m of dispersion compensation fibres (UHNA4) were inserted to manage the overall dispersion of the cavity and to form stable and self-starting mode-locked pulse. It is to be noted here that mode-locking was not possible when the total passive fibre length in the cavity was less than 20 meters. The net cavity dispersion is anomalous in nature with second order dispersion of -0.16 ps^2 enabling fundamental soliton operation with a repetition rate of 6.87 MHz.

Fig. 3.6.2 shows the spectrum of the mode-locked pulses with increasing pump power. The central wavelength of the laser is 1960nm with a 3 dB bandwidth of 7 nm. The bandwidth of this noise-like soliton pulses remains the same when the pump power raised from 115 mW to 225 mW.

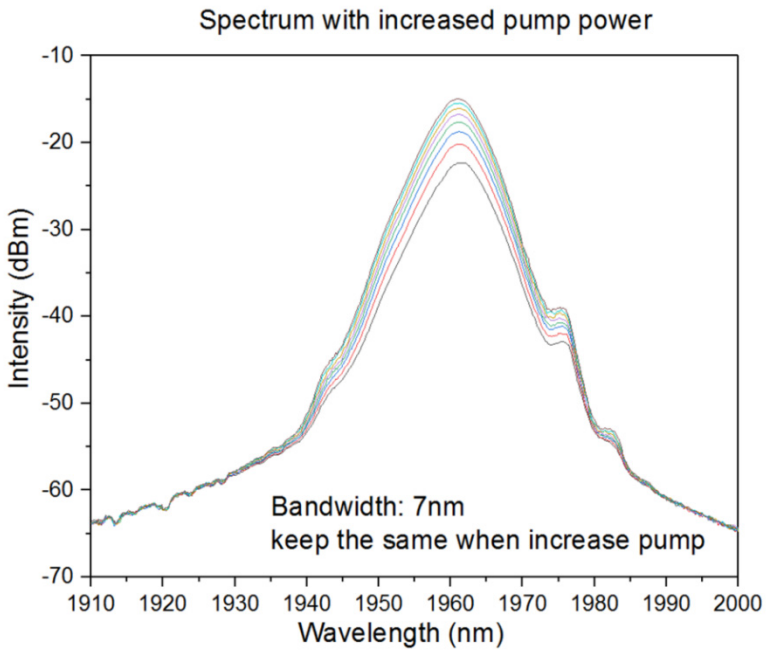

Fig. 3.6.2. The spectrum with increased pump power from 115 mW to 225 mW.

Fig. 3.6.3. (left) shows the pulse-width and the squared pulse shape of the noise-like pulse measured by CSA (20 GHz) and a fast photodetector (7 GHz). When the pump was set at 154.9 mW, the pulse-width is measured to be 240 picosecond (blue line). The pulse-width increased gradually with the increasing pump power and becomes 2.12 nanosecond at a pump power of 225 mW (orange line).

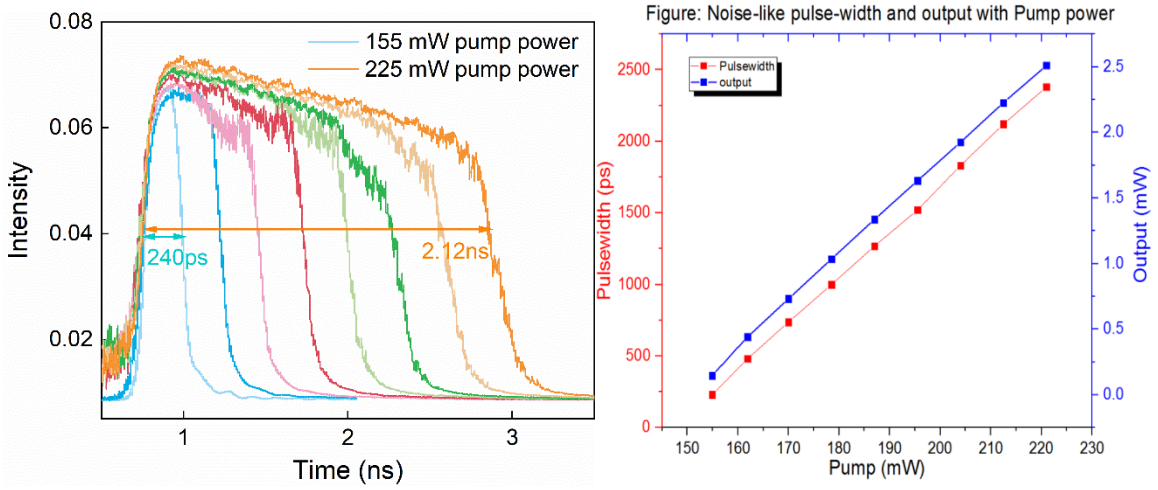

Fig. 3.6.3. (left) The pulse-width with increased pump power from 155 mW to 225 mW. (right) Noise-like pulse-width and output power with increased pump power from 155 mW to 225 mW.

The pulse-width and the output power as a function of pump power are illustrated in Fig. 3.6.3. (right). It can be seen that the pulse-width and the output power increase linearly with pump power which also reaffirms the generation of noise-like soliton pulse.

In conclusion, utilizing a long fibre ring cavity based on this SESAM1 noise-like soliton pulse was generated, the noise-like operation could be caused by the limited modulation depth (10%) [46]. The width of the noise-like pulses increased from 0.24 ns to 2.12 ns as the pump power increased from 115 mW to 225 mW while the average output power increased linearly from 0.3 mW to 2.5 mW. However, such noise-like pulse source is not suitable as a seed for chirped pulse amplification so I investigated an alternative SESAM with larger modulation depth to generate idea mode-lock pulses, the details of which will be presented in the next sub-section.

3.6.2 SESAM2 (high modulation depth)

To address the issue of a noise-like soliton pulse generation which is limited by modulation depth (10%) of the SESAM1 and build an ideal seed for the intended CPA system. I replaced the previous SESAM (Batop, SAM-1960-18-10ps) with a new SESAM (SAM-1960-54-10ps) which has 30% modulation depth (from Batop).

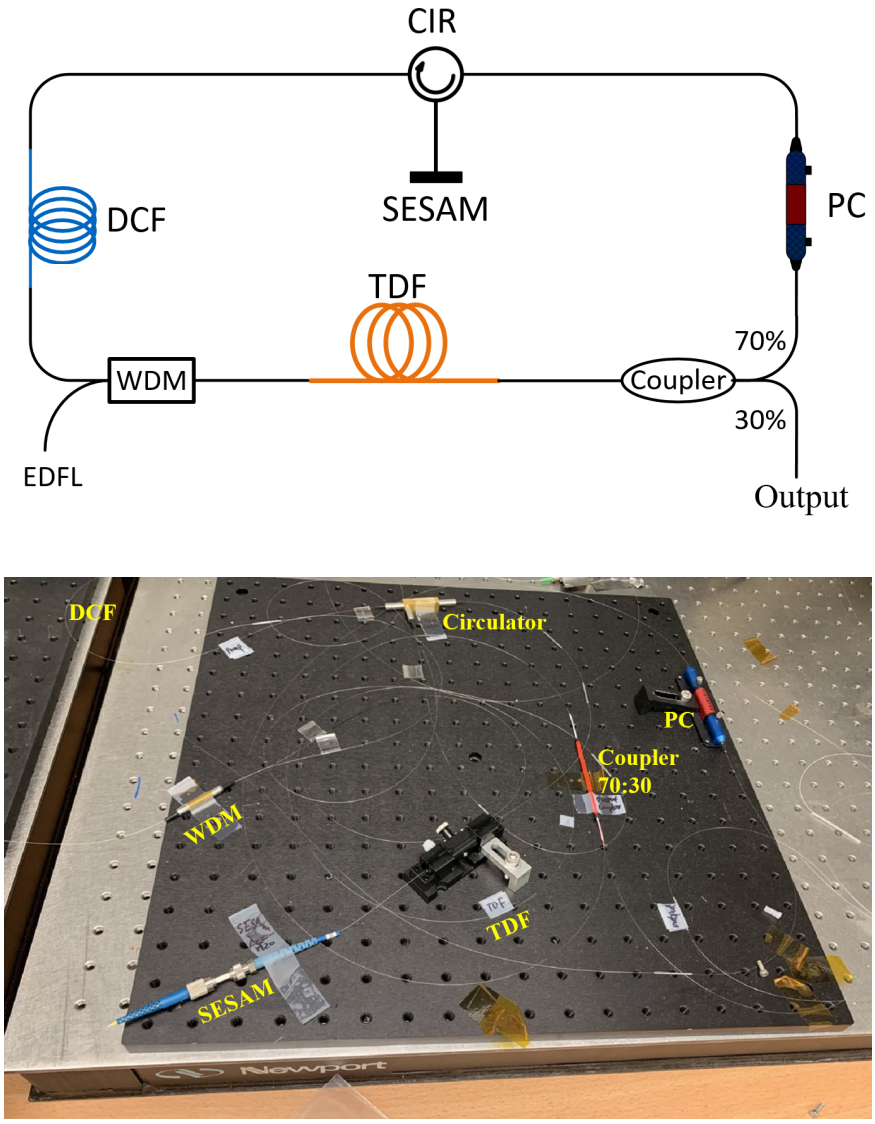

Fig. 3.6.4. Schematic of the dissipative oscillator. TDF: thulium-doped fibre; DCF: dispersion compensation fibre; SESAM: semiconductor saturable absorber mirror; WDM: wavelength division multiplexer; PC: polarization controller; CIR: circulator; EDFL: erbium doped fibre laser.

The mode-locked, uni-directional ring laser schematic is shown in Fig. 3.6.4. which incorporating a homemade 1560 nm erbium-doped fibre pump laser (EDFL) coupled to 2 meters of single-mode thulium-doped fibre (TDF) (OFS, TmDF200) with a 1560/1960 nm wavelength-division multiplexer (WDM). The TDF has ~20 dB/m absorption at 1560 nm and a group velocity dispersion of approximately -0.02 ps^2/m at 1.9 μm. A compact in-line

polarization controller (PC) (FIBERPRO PC1100) has 0.2 dB insertion loss. SESAM (SAM-1960-54-10ps) is sandwiched between two fibre ultra-physical contact (UPC) connectors for best contact with a plastic tube. I estimate that the nonlinear pulse propagation in the DCF and TDF inside the cavity during mode-locked operation gives rise to a total B-integral of ~0.8π, and the cavity circulator provides a polarization dependent loss of 0.6 dB as required to sustain nonlinear polarization rotation (NPR). Hence, as is common for dissipative soliton lasers, I used the SESAM to initiate self-starting and NPR to stabilize the pulses by appropriate adjustment of the intracavity polarization controller. The 70% port of a tap coupler was used to extract the output for subsequent amplification. A 5.2 m section of normal dispersion fibre (NDF) (Nufern Inc. UHNA4; 0.09 ps^2/m at 1900 nm) was placed between the circulator and the WDM for dispersion management [47,48]. The fibre pigtails of all the components were of Corning SMF 28 (dispersion -0.067 ps^2/m at 1900 nm). Considering the total SMF length of 6 m and the total cavity length of 13.2 m I estimate the net dispersion of the cavity to be ~0.026 ps^2.

With appropriate adjustment of the polarization controllers in the laser cavity (Fig. 3.6.4), self-starting and stable mode-locked operation was achieved at a pump power of 400 mW (used for all the CPA results shown below). The corresponding output power was 40 mW and the pulse energy was 2.5 nJ. The laser would maintain stable operation and provided increased output power of 45 mW when the pump power was increased to 420 mW, but both the pulse train on the oscilloscope and the optical spectra became unstable at higher pump powers. The measured repetition rate of 15.7 MHz shown in Fig. 3.6.5 (a) was in agreement with calculations based on the cavity length, supporting the conjecture that the oscillator operates with a single pulse per round trip. The insert in Fig. 3.6.5 (a) shows the measured autocorrelation of the positively chirped output with an inferred pulse width of 25 ps (assuming a Gaussian pulse shape). The radio-frequency (RF) spectrum (Fig. 3.7.2 (b)) exhibits a ~71 dB signal-to-noise ratio measured with a range of 10 kHz and a resolution bandwidth of 10 Hz, indicating the stability of the mode-locking. I attribute the small peaks offset by 23 kHz from the fundamental cavity frequency to be due to relaxation oscillations. The RF spectrum with a frequency span of 1 GHz is shown inset to Fig. 3.6.5 (b) with resolution bandwidth of 1 MHz.

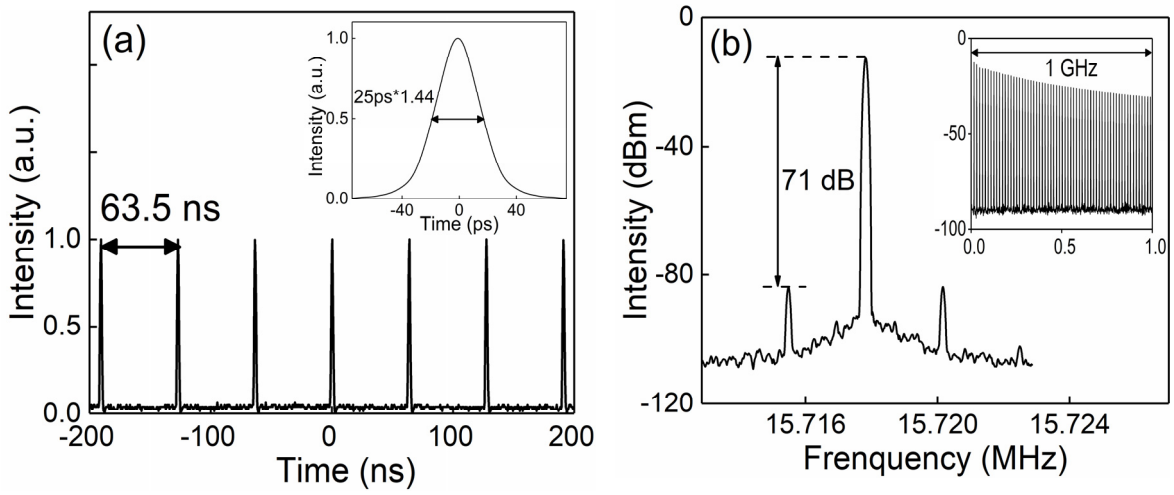

Fig. 3.6.5. (a) Oscilloscope trace of the output pulses. Inset: autocorrelation trace of the seed laser. (b) RF spectrum at the fundamental frequency of 15.7 MHz. Inset: RF spectrum with 1 GHz span.

The oscillator spectrum measured with OSA, is shown in Fig. 3.6.6. (a). The center wavelength was 1925 nm, the 3 dB width was ~40 nm and the shape had the characteristic steep spectral edges associated with dissipative soliton mode-locking. The signal was 27 dB above the ASE floor.

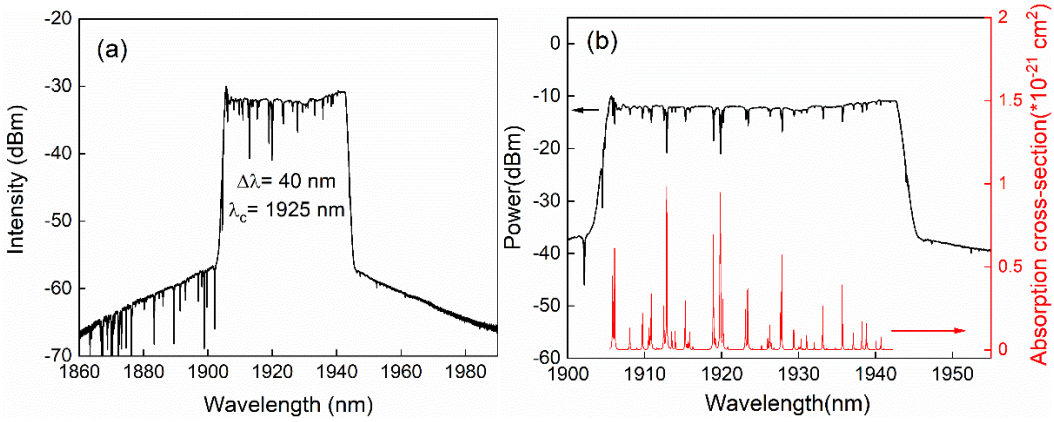

Fig. 3.6.6. (a) Measured oscillator spectrum. (b) Atmospheric gas absorption spectrum (HITRAN) Vs. measured spectrum.

The red line in Fig. 3.6.6.(b) illustrates the simulated atmospheric gas absorption cross-section (red) based on the HITRAN database (assumes mean altitude and summertime with gas mixtures of H_2O: 1.86%; CO_2: 0.033%; O_3: 0.000003%; N_2O: 0.000032%; CO: 0.000015%; CH_4: 0.00017%; O_2: 20.900001%; N_2: 77.206%). We could also see that in terms of both the wavelength and relative absorption intensity, the absorption dips on the measured experimental spectrum (Fig. 3.6.6. (b) black line) matched with the simulated

atmospheric gas absorption cross-section line. This confirms that the spectral absorption dips are caused by atmospheric gas in the OSA itself (approximately 2.8 m). Fig. 3.6.7(a) shows the calculated Fast Fourier transform (FFT) of the spectrum that was used for the oscillator. It shows it with the gas absorption line (black) and when it modified itself without the gas absorption line (red), while in the dB scale we must assume zero spectral phase shift. We could only see a 2% energy difference located in the main peak, which means that the atmospheric gas in the lab had a slight effect on the compressed pulse shape. By using a transmission grating pair (Ibsen), the autocorrelation of the compressed oscillator pulses are shown in Fig. 3.6.7(b). The pulse-width of 280 fs assumes the Gaussian pulse profile and thus the time bandwidth product (TBP) was calculated to be 0.91, which is 2.1 times the transform-limited value for a Gaussian pulse (0.44), but close to that of a transform-limited pulse with a rectangular-spectrum (0.88).

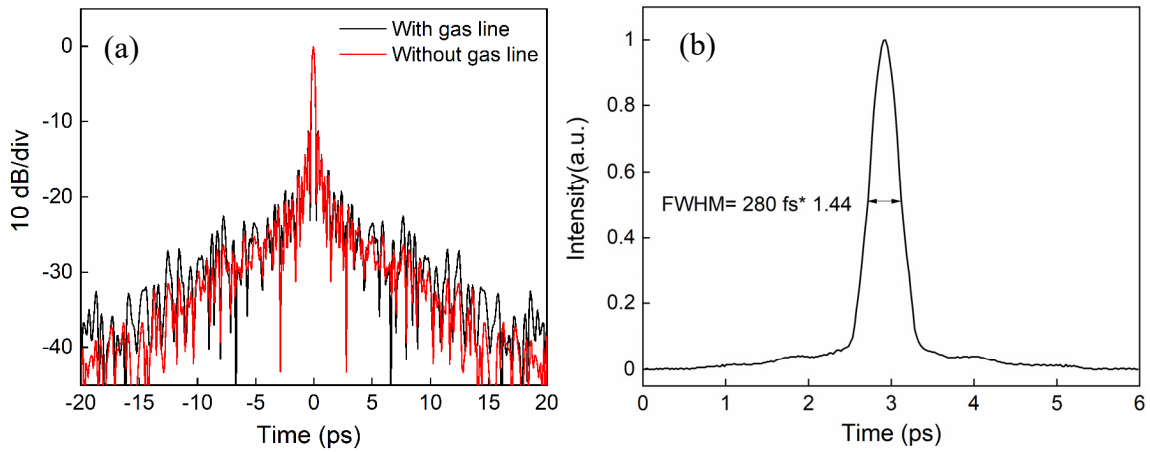

Fig. 3.6.7. (a) The FFT of the spectrum for the oscillator with gas absorption line (black) and modified itself without gas line (red). (b) Autocorrelation trace of the compressed oscillator pulses.

With the new SESAM inside the cavity and with the optimisation of the oscillator's parameters, I obtained a self-started mode-locked pulse at a pulse energy of 2.5 nJ with a central wavelength of 1925 nm and a 3 dB bandwidth of 40 nm at a repetition rate of 15.6 MHz. Benefitting from a broad bandwidth (40 nm), the chirped pulses from the oscillator (25 ps) were able to be compressed through a grating pair to 280 fs. In addition, the spectral dip lines caused by the atmospheric gas in the lab had a minor effect on the compressed pulse shape. This pulse was deemed as qualified to work as a seed source for amplification in a future CPA system.

3.7 Summary

In conclusion, this chapter explored the ideal source with large bandwidth and chirped pulse for the following CPA system in order to generate high performance output pulses properties in terms of high peak power and energy. Table 3.7 gives a summary of the mode-locked seed source output characteristics based on different saturable absorbers.

Table 3.7.1 Important characteristics of the seed source for different SAs.

	NPR	CNT	SESAM1	SESAM2
Types of pulse generation	Soliton	Dissipative soliton	Noise-like pulse	Dissipative soliton
Pulse-width	0.85 ps	14.6 ps	240 ps ~ 2 ns	25 ps
Spectral bandwidth	5.5 nm	18.3 nm	7 nm	40 nm
Limitation	Spectral sidebands	CNT physical damage	Cannot be compressed	NA

A conventional soliton mode-locked fibre laser at 1942 nm with a spectrum consisting of strong Kelly sidebands was deemed unsuitable as a seed for the intended CPA system. In addition, I found that when DCF was inserted to manage cavity dispersion, it became difficult to achieve mode-locking.

A CNT saturable absorber based two-micron dissipative soliton mode-locked fibre laser pumped by a 1560 nm single mode laser diode emitting around 1960 nm is demonstrated. Unfortunately, after a prolonged operation, the CNT deteriorated to the point whereby it could no longer produce a stable mode-lock pulse.

To obtain a long lifetime, self-start and dissipative soliton mode-locked pulse, a commercial SESAM working at 1960 nm was used. However, through this SESAM the oscillator always generated noise-like pulses that lasted a nanosecond due to its limited modulation depth (10%). I observed that the pulse-width and output power increased linearly with pump power,

a typical characteristic of noise-like pulses. However, these noise-like pulses were deemed unsuitable to seed a CPA system and so I therefore explored alternative solutions.

Finally, a dissipative soliton mode-locked fibre laser at 1925 nm was investigated using another SESAM with larger modulation depth (30%). The oscillator could generate self-started mode-locked pulses at a pulse energy of 2.5 nJ and a 3 dB bandwidth of 40 nm at a repetition rate of 15.6 MHz. The pulses were able to be compressed to 240 fs with only minor effects on the gas absorption line. In addition, chirped pulses with a duration of 25 ps were beneficial for the reduction of nonlinear accumulation in the following fibre-based segments of the CPA system. In summary, I realize this new pulse was deemed qualified for amplification in a future high performance CPA system.

Reference

[1] M. E. Fermann, and I. Hartl, “Ultrafast fiber laser technology,”. IEEE J. Sel. Top. Quantum Electron. **15**(1), 191–206 (2009).

[2] J. Jiang, C. Mohr, J. Bethge, A. Mills, W. Mefford, I. Hartl, M. E. Fermann, C.-C. Lee, S. Suzuki, T. R. Schibli, N. Leindecker, K. L. Vodopyanov, P. G. Schunemann, “500 MHz, 58 fs highly coherent Tm fiber soliton laser,” in “Conference on Lasers and Electro-Optics 2012,” (Optical Society of America, 2012), p. CTh5D.7.

[3] R. C. Sharp, D. E. Spock, N. Pan, and J. Elliot, "190-fs passively mode-locked thulium fiber laser with a low threshold," Opt. Lett. **21**(12), 881-883 (1996).

[4] J. Wang, X. Liang, G. Hu, Z. Zheng, S. Lin, D. Ouyang, X. Wu, P. Yan, S. Ruan, Z. Sun, and T. Hasan, “152 fs nanotube-mode-locked thulium-doped all-fiber laser,” Sci. Rep. **6**, 28885 (2016)..

[5] G. Sobon, J. Sotor, T. Martynkien, and K. M. Abramski, "Ultra-broadband dissipative soliton and noise-like pulse generation from a normal dispersion mode-locked Tm-doped all-fiber laser," Opt. Express **24**(6), 6156-6161 (2016).

[6] Regina Gumenyuk, Ismo Vartiainen, Hemmo Tuovinen, and Oleg G. Okhotnikov, "Dissipative dispersion-managed soliton 2 μm thulium/holmium fiber laser," Opt. Lett. **36**(5), 609-611 (2011).

[7] C. Huang, C. Wang, S. Wei, N. Yang, Y. Tang, and J. Xu, “Developing high energy dissipative soliton fiber lasers at 2 micron,” Sci. Rep. **5**, 13680 (2015).

[8] Q. Wang, J. Geng, T. Luo, and S. Jiang, "Ultrashort Pulse 2 Micron Fiber Lasers," in Advanced Solid-State Lasers Congress, M. Ebrahim-Zadeh and I. Sorokina, eds., OSA Technical Digest (online) (Optical Society of America, 2013), paper MTh1C.1.

[9] Q. Wang, T. Chen, M. Li, B. Zhang, Y. Lu and K.P. Chen, “All-fiber ultrafast thulium-doped fiber ring laser with dissipative soliton and noise-like output in normal dispersion by single-wall carbon nanotubes,” Appl. Phys. Lett. **103** (1), 011103 (2013).

[10] D. Paschotta, "passive mode locking, passively mode-locked lasers, ultrashort pulses, slow saturable absorbers", Rp-photonics.com, 2016. [Online]. Available: https://www.rp-photonics.com/passive_mode_locking.html. [Accessed: 05- Aug- 2016].

[11] Z. Liu, "FEMTOSECOND PULSE GENERATION IN FIBER OSCILLATORS AND PULSE PROPAGATION IN MULTIMODE FIBER," Cornell University (2017).

[12] V. Matsas, T. Newson, D. Richardson and D. Payne, “Selfstarting passively mode-locked fibre ring soliton laser exploiting nonlinear polarisation rotation,” Electron. Lett. **28**(15), 1391 (1992).

[13] V. Matsas, T. Newson and M. Zervas, “Self-starting passively mode-locked fibre ring laser exploiting nonlinear polarisation switching,” Opt. Commun. **92**(1-3), 61-66 (1992).

[14] U. Keller, "Recent developments in compact ultrafast lasers", Nature **424**, 831-838 (2003).

[15] F. Wang, A. Rozhin, V. Scardaci, Z. Sun, F. Hennrich, I. White, W. Milne and A. Ferrari, "Wideband-tuneable, nanotube mode-locked, fibre laser", Nature Nanotech. **3**(12), 738-742 (2008).

[16] C. S. Goh, K. Kikuchi, S. Y. Set, D. Tanaka, T. Kotake, M. Jablonski, S. Yamashita, and T. Kobayashi, “Femtosecond mode-locking of an ytterbium-doped fiber laser using a carbon-nanotube-based mode-locker with ultra-wide absorption band,” in Conference on Lasers and Electro-Optics, CThG2 (2005).

[17] J. H. Yim, W. B. Cho, S. Lee, Y. H. Ahn, K. Kim, H. Lim, G. Steinmeyer, V. Petrov, U. Griebner, and F.Rotermund, “Fabrication and characterization of ultrafast carbon nanotube saturable absorbers for solid state laser mode-locking near 1 μm,” Appl. Phys. Lett. **93**(16), 161106 (2008).

[18] S. Y. Set, H. Yaguchi, Y. Tanaka, M. Jablonski, Y. Sakakibara, A. Rozhin, M. Tokumoto, H. Kataura, Y. Achiba, and K. Kikuchi, "Mode-locked Fiber Lasers based on a Saturable Absorber Incorporating Carbon Nanotubes," in Optical Fiber Communication Conference, Technical Digest (Optical Society of America, 2003), paper PD44.

[19] M. A. Solodyankin, E. D. Obraztsova, A. S. Lobach, A. I. Chernov, A. V. Tausenev, V. I. Konov, and E. M. Dianov, "Mode-locked 1.93 μm thulium fiber laser with a carbon nanotube absorber," Opt. Lett. **33**(12), 1336-1338 (2008).
[20] Y. S. Fedotov, A.V. Ivanenko, S. M. Kobtsev, and S. V. Smirnov, "High average power mode-locked figure-eight Yb fibre master oscillator," Opt. Express **22**(25), 31379-31386 (2014).
[21] N. J. Zabusky and M. D. Kruskal, "Interaction of "Solitons" in a Collisionless Plasma and the Recurrence of Initial States," Phys. Rev. Lett. **15**(6), 240 (1965).
[22] A. Hasegawa and F. Tappert, "Transmission of stationary nonlinear optical pulses in dispersive dielectric fibers. I. Anomalous dispersion,"Appl. Phys. Lett. **23**(3), 142, (1973).
[23] L. F. Mollenauer and R. H. Stolen, "The soliton laser," Opt. Lett. **9**(1), 13-15 (1984).
[24] L. Nelson, D. Jones, K. Tamura, H. Haus and E. Ippen, "Ultrashort-pulse fiber ring lasers," Applied Physics B **65**, 277-294 (1997).
[25] N. J. Smith, K. J. Blow, and I. Andonovic, "Sideband generation through perturbations to the average soliton model," IEEE J. Lightwave Technol. **10**(10), 1329 (1992).
[26] U. Keller, "Ultrafast solid-state laser oscillators: a success story for the last 20 years with no end in sight", Applied Physics B **100**, 15-28 (2010).
[27] M. Fermann, A. Galvanauskas, G. Sucha and D. Harter, "Fiber-lasers for ultrafast optics", Applied Physics B **65**(2), 259-275 (1997).
[28] K. Tamura, E. P. Ippen, H. A. Haus, and L. E. Nelson, "77-fs pulse generation from a stretched-pulse mode-locked all-fiber ring laser," Opt. Lett. **18**(13), 1080-1082 (1993).
[29] H. A. Haus, K. Tamura, L. E. Nelson and E. P. Ippen, "Stretched-pulse additive pulse mode-locking in fiber ring lasers: theory and experiment," IEEE J. Quantum Electron. **31**(3), 591-598 (1995).
[30] P. Grelu and N. Akhmediev, "Dissipative solitons for mode-locked lasers," Nat. Photonics, **6**, 84-92 (2012).
[31] R. Gumenyuk, I. Vartiainen, H. Tuovinen and O. Okhotnikov, "Dissipative dispersion-managed soliton 2 μm thulium/holmium fiber laser", Optics Letters, **36**(5), 609 (2011).
[32] W. H. Renninger, A. Chong, and F. W. Wise, "Dissipative solitons in normal-dispersion fiber lasers," Phys. Rev. A **77**(2), 023814 (2008).
[33] W. Chang, A. Ankiewicz, J. M. Soto-Crespo, and N. Akhmediev, "Dissipative soliton resonances," Phys. Rev. A **78**(2), 023830 (2008).
[34] W. Du, H. Li, J. Li, P. Wang, S. Zhang, and Y. Liu, "Mechanism of dissipative-soliton-resonance generation in fiber laser mode-locked by real saturable absorber," Opt. Express **26**(16), 21314-21323 (2018).
[35] F. Wise, A. Chong, and W. Renninger, "High-energy femtosecond fiber lasers based on pulse propagation at normal dispersion," Laser Photonics Rev. **2**(1-2), 58 (2008).
[36] V.J. Matsas, T.P. Newson, and M.N. Zervas, "Self-starting passively mode-locked fibre ring laser exploiting nonlinear polarisation switching," Opt. Commun. **92**(1-3), 61–66 (1992).
[37] M. Horowitz, Y. Barad, and Y. Silberberg, "Noiselike pulses with a broadband spectrum generated from an erbium-doped fiber laser," Opt. Lett. **22**(11), 799–801, (1997).
[38] D.Y. Tang, L.M. Zhao, and B. Zhao, "Soliton collapse and bunched noise-like pulse generation in a passively mode-locked fiber ring laser," Opt. Express **13**(7), 2289–2294 (2005).
[39] Q.Q. Wang, T. Chen, M. Li, B. Zhang, Y. Lu, and K.P. Chen, "All-fiber ultrafast thuliumdoped fiber ring laser with dissipative soliton and noise-like output in normal dispersion by single-wall carbon nanotubes," Appl. Phys. Lett. **103**(1), 011103 (2013).
[40] F.X. Kärtner, J.A. der Au and U. Keller, "Mode-locking with slow and fast saturable absorbers–what's the difference," IEEE J Sel. Top. Quant. **4**(2), 159–168 (1998).
[41] M. E. Fermann and I. Hartl, "Ultrafast Fiber Laser Technology," IEEE J. Sel. Top. Quantum Electron. **15**(1), 191–206 (2009).
[42] Y. Wang, S. Alam, E. Obraztsova, A. Pozharov, S. Set, and S. Yamashita, "Generation of stretched pulses and dissipative solitons at 2μm from an all-fiber mode-locked laser using carbon nanotube saturable absorbers," Opt. Lett. **41**(16), 3864-3867 (2016).

[43] T. Hasan, Z. Sun, F. Wang, F. Bonaccorso, P. Tan, A. Rozhin and A. Ferrari, "Nanotubeâ Polymer Composites for Ultrafast Photonics," Adv. Mater. **21**(3839), 3874-3899 (2009).
[44] K. Kieu, W. Renninger, A. Chong and F. Wise, "Sub-100 fs pulses at watt-level powers from a dissipative-soliton fiber laser", Opt. Lett. **34**(5), 593 (2009).
[45] S. Turitsyn, B. Bale and M. Fedoruk, "Dispersion-managed solitons in fibre systems and lasers", Physics Reports **521**(4), 135-203 (2012).
[46] R. Herda and O. G. Okhotnikov, "Dispersion compensation-free fiber laser mode-locked and stabilized by high-contrast saturable absorber mirror," IEEE J. Quantum Electron. **40**(7), 893–899 (2004).
[47] P. Ciąćka, A. Rampur, A. Heidt, T. Feurer, and M. Klimczak, "Dispersion measurement of ultra-high numerical aperture fibers covering thulium, holmium, and erbium emission wavelengths," J. Opt. Soc. Am. B **35**(6), 1301-1307 (2018).

Chapter 4

Compact chirped-pulse amplification system based on Tm^{3+} doped silica fibre

4.1 Introduction

High power and high energy ultra-short-pulse fibre lasers at 2 μm are an attractive option for application in many operations, including free space optical communications, sensing, material processing and mid-IR generation [1-4]. High energy applications of the laser in the 2 μm range in particular, such as in high harmonic generation [5] and laser-driven electrons acceleration [6], would benefit from repetition-rate scaling. While ultimately this may be realised in the future using a rod-type and/or coherently combined fibre amplifiers [7-9], here I focus on developing systems with more conventional, flexible, fibre technology. This is because it is an important research target that has immediate practical applications including material processing and mid-IR light generation.

Recent demonstrations of 2 μm thulium-doped fibre laser systems based on chirped pulse amplification (CPA) have enabled fs pulse generation with μJ energies [7,10,11]. For example, using a conventional large-mode-area fibre, Sims *et al.* demonstrated 1 μJ energy and 3 MW peak power in 300 fs pulse [10]. Later, pulses with a higher 4 MW peak power and 152 W average power were achieved through the use of thulium doped photonic crystal fibre (PCF) with a 50 μm core diameter and by stretching the seed pulse much more than in the past to a duration of 400 ps [7]. The highest recorded average power (1 kW/50 MW peak) used the same PCF as discussed above and further increased the stretched pulse duration to 1 ns by using two customised chirped fibre Bragg gratings (CFBG) [12]. The use of rods compromises on compactness and generally requires free space signal coupling; something which I suggest is not ideal for many industrial settings. Following this, Hoogland *et al.* used a chirped volume Bragg grating (CVBG) as a temporal stretcher and compressor, achieving in this way pulses with 1 MW peak power at 371 fs duration based on conventional large

mode area fibre [11]. However, the use of bulk or free space optical elements to stretch the pulses, rather than using monolithically integrated pulse stretchers, compromises the systematic long-term stability [7,11]. Furthermore, systems [10,11] that use pulse-pickers to increase pulse energy have unwanted insertion losses that require the addition of more amplification stages. Therefore, systems with an all-fibre pulse pre-stretcher have been demonstrated in order to improve stability. In one case, the oscillator's output was stretched in a 50 m long normal dispersion fibre and then amplified in a two stage MOPA finally to produce 161 nJ pulses through a grating pair compressor [13]. However, in that case, the relatively small mode area of the gain fibre limited any further energy scaling due to self-phase-modulation (SPM). To keep the dispersion elements compact, pulses were stretched in a CFBG and subsequently re-compressed with a CVBG, but then a pulse-picker reduced the repetition rate to 92 kHz thus limiting the average power to just 0.64 W (4 μJ pulse energy, 2.4 MW peak power) [14].

In this chapter, I first present a simple dissipative soliton seeded CPA system based on cladding pumping a silica thulium-fibre output high peak and having average powers of 1925 nm. Using a normal-dispersion fibre-based pulse stretcher, just two amplification stages, and a high-efficiency transmission grating compressor, enabled an excellent performance to be achieved with a highly practical and compact system, when compared to those previously reported. Via careful optimisation of the seed laser and fibre amplifiers, the final system was able to generate 1.25 μJ energy, 297 fs pulses with 4.2 MW peak power, 21.5 W average power and a beam quality M^2 of 1.1 at a repetition rate of 15.7 MHz. Following this, I investigated pulse energy and peak power scaling by core pumping a shorter length of active fibre in the power amplifier. By inserting a pulse-picker, adding an extra following pre-amplifier and core pumping a thulium doped fibre that was 5 times shorter (29 cm) in the power amplifier, the CPA system was able to generate 285 fs pulses with an energy of 5.7 μJ, an average power of 2.8 W and a peak power of 20 MW.

Section 4.2 and 4.3 respectively describe the high peak power CPA system through the cladding pumping and core pumping schemes for a segment on commercial silica thulium-doped fibre. These two experiments were mainly conducted by the author. Section 4.4 summarises this chapter and gives a concluding remark. The work described in this chapter has previously been published in [15].

4.2 CPA system based on cladding pumping a silica thulium-doped fibre

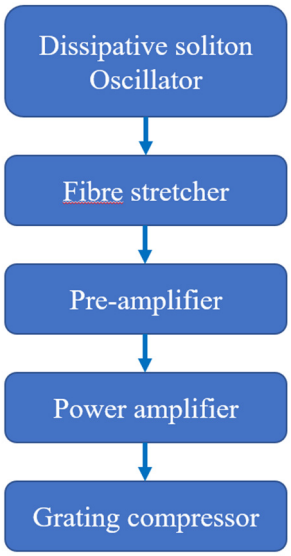

Fig. 4.2.1. Schematic of the dissipative oscillator seeded CPA system.

The structure of the compact and simple dissipative oscillator seeded silica thulium-fiber CPA system is illustrated in the Fig. 4.2.1. A normal-dispersion fibre based pulse stretcher, use of just two amplification stages (pre-amplifier and power amplifier), and a high-efficiency transmission grating compressor, enabled this performance to be achieved with a highly practical and compact system.

4.2.1 Dissipative soliton oscillator

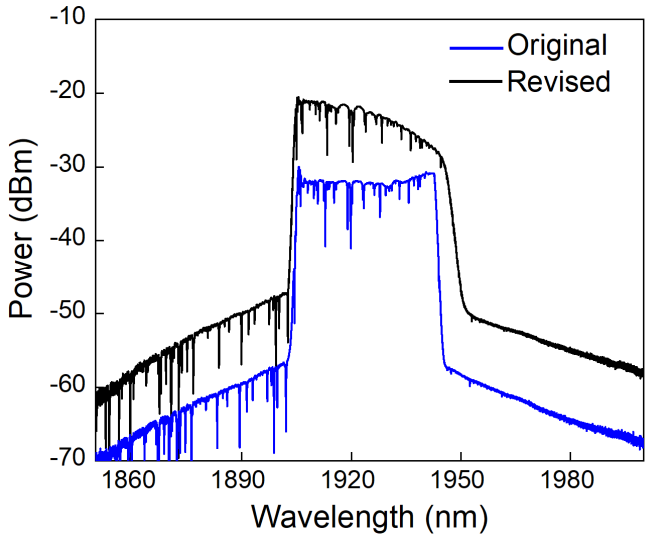

Fig. 4.2.2 The optical spectrum of the seed laser with original flat top shape (black) and the revised shape (blue).

The oscillator structure is presented in the Chapter 3.6.2 which can provide mode-locking pulses with ideal characteristics for the CPA system. Base on that, I am able to achieve a limited degree of spectral amplitude shaping from the oscillator output through precise adjustment of the PC. This was used to pre-compensate the low gain at shorter wavelengths in the intentionally under-length power amplifier due to the signal reabsorption is prominent at shorter wavelength.

The revised oscillator spectrum used for the flowing amplifier configuration, measured with a resolution of 0.05 nm, is shown in Fig. 4.2.2 (blue line). Compared with the original spectrum with relatively flat top shape over ~40 nm range (Fig. 4.2.2 black line), the revised spectrum has higher intensity at short wavelength and the intensity is gradually decreased toward long wavelength part. This spectral tilt was realized by precisely adjust the polarization controller inside the cavity and helps to compensate the lower gain of the power amplifier at shorter wavelength over the pulse spectrum. The revised spectral center wavelength was 1925 nm, the 10 dB width was ~40 nm and the shape had the characteristic steep spectral edges associated with dissipative soliton mode-locking. The signal was 27 dB above the ASE floor.

4.2.2 Fibre stretcher

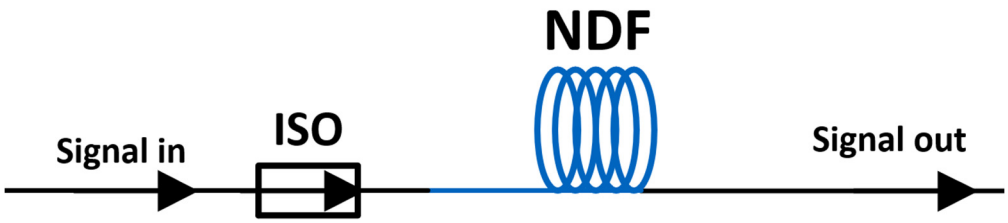

Fig. 4.2.3 Schematic of the stretcher part. ISO: isolator, NDF: normal dispersion fibre.

After the oscillator, the stretcher includes 58 m NDF (Nufern Inc. UHNA7) (with dispersion of 0.046 ps^2/m) and 25 m of UHNA4 (with dispersion of 0.09 ps^2/m) were coiled as Fig.4.2.4 shown, which can provide total dispersion of 4.9 ps^2. The combination of UHNA4 and UHNA7 enabled better compression results than a single fibre type due to their opposite sign of third order dispersion [16].

Fig. 4.2.4 Photo of the normal dispersion fibre coils. Top: Nufern UHNA4, Bottom: UHNA7.

Due to the small core size of the UHNA4 (2.2μm) and UHNA7 (2.2μm), conventionally common splicing program of SMF28 - SMF28 with central splicing position for Fujikura fsm-100p splicer will cause relatively large splicing loss for the SMF28 and UHNA fibre. An offset-arc splicing technique (offsetting the arc position from the splicing location towards SMF28 100 μm) was used to decrease the splice loss to 0.5 dB. This result can be further reduced to 0.15 dB by using a filament fusion splicer (e.g. Vytran FFS2000WS) to control the thermal profile of the splice and fire polish reported in [17].

To reduce the nonlinear phase shift in the 83 m long stretcher fibre, the power was decreased to 4 mW with an attenuator at the stretcher input. After the fibre stretcher, the pulse-width is broadening from 25 ps (Fig. 4.2.5 inset) to ~105 ps which is measured by an extended InGaAs photodetector (EOT, ET-5000F, bandwidth >12.5 GHz) and an oscilloscope (Tektronix, CSA 803A, with 50 GHz bandwidth), as depicted in Fig. 4.2.5. The speed of the detection system was high enough to measure the pulse duration over 60 ps when using a commercial 500 fs mode-locked laser to test. The theoretically calculated pulse-width after the fibre stretcher is ~103 ps through the eq. 2.65, which is very close to the experimental result.

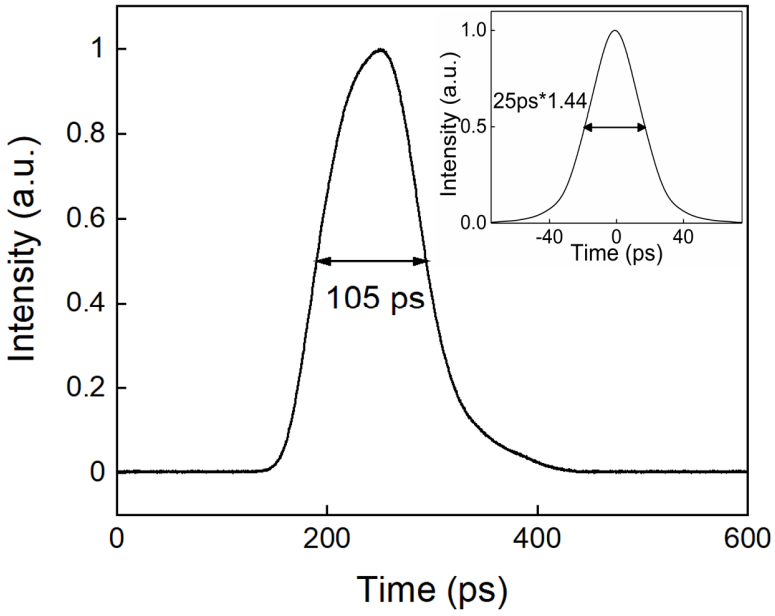

Fig. 4.2.5 Output of the pulses after fibre stretcher in time domain. Inset: the pulse width of the oscillator.

4.2.3 Pre-amplifier

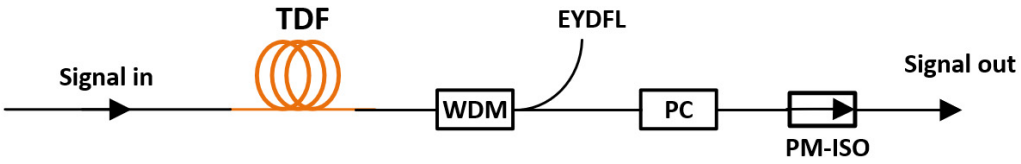

Fig. 4.2.6 Schematic of the pre-amplifier. TDF: thulium-doped fibre; WDM: wavelength division multiplexer; EYDFL: erbium/ytterbium doped fibre laser; PC: polarization controller; PM: polarization maintaining.

Fig. 4.2.6 shows the schematic of the pre-amplifier. An erbium/ytterbium doped fibre laser (EYDFL) was built to core-pump the pre-amplifiers at 1563 nm. Fig. 4.2.7 (left) shows the schematic of the EYDFL. This pump laser had a 4 m Er/Yb doped fibre (Nufern) with a core/clad diameter of 12/130 μm and core/first cladding NA of 0.2/0.46 pumped by two 915 nm laser diodes. The HR FBG (OF-LINK Ltd.) had a very high reflectivity of over 99% at 1563 nm with a FWHM of 2 nm whereas the LR FBG as an output coupler had a reflectivity of 10% at 1563 nm with a FWHM of 1.2 nm. This pump laser can provide adequate pump power with maximum of 3 W in the pre-amplifier. The spectrum shows a centre wavelength of 1563 nm with an OSNR over ~60 dB as shown in the Fig. 4.2.7 (right).

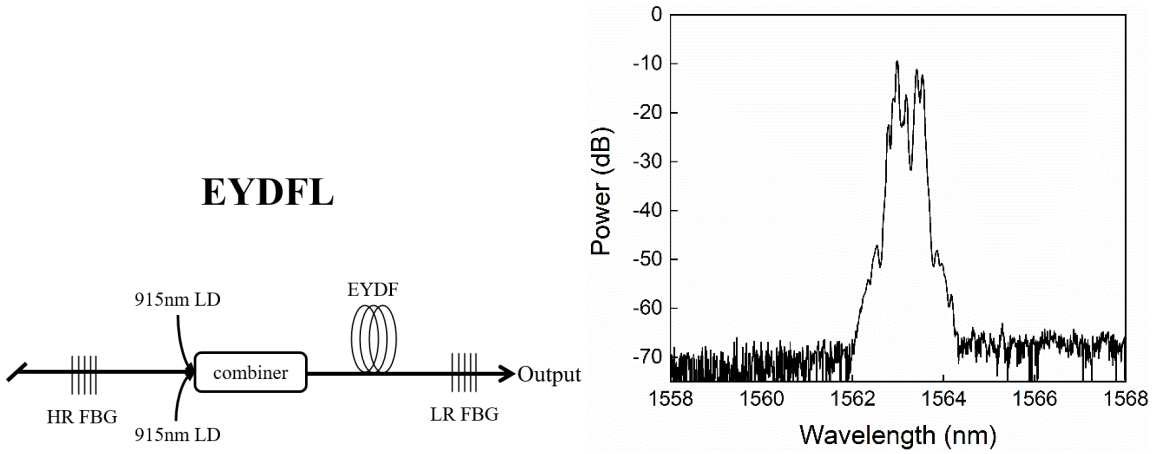

Fig. 4.2.7 (left) Schematic of the EYDFL. (right) output spectrum of the EYDFL.

A commercial thulium doped fibre from OFS (TmDF200) was used, with a 5-μm MFD at 1700 nm, a 125-μm cladding and NA of 0.26. This fibre had a measured absorption of ~20 dB/m at 1563 nm. In order to minimize the nonlinearity phase shift, the active fibre was backward pumped to short the effective fibre length compared with forward pumping scheme. A non-PM pre-amplifier was used due to short term component availability, this would ideally be upgraded in due course to provide a fully PM system - however this did not compromise the current experiments.

The signal was amplified to an average power of 180 mW in the pre-amplifier. This power was chosen to avoid unnecessary non-linear phase yet to still have sufficient signal power to saturate the subsequent power amplifier. A second PC is incorporated after the pre-amplifier to orient the polarization of the pulses to the transmission axis of the PM isolator, generating pulses with linear polarization to obtain optimum transmission ratio through the compression gratings. After adjustment of the PC before the the fast-axis blocking isolator between the pre- and power-amplifier the spectrum was as shown in Fig. 4.2.8 (blue line), which keep similar as the oscillator (Fig. 4.2.8 black line). The average power at the input of the final amplifier reduced to 120 mW because some degree of depolarization in the long length of non-PM stretcher fibre led to an excessive the isolator insertion loss.

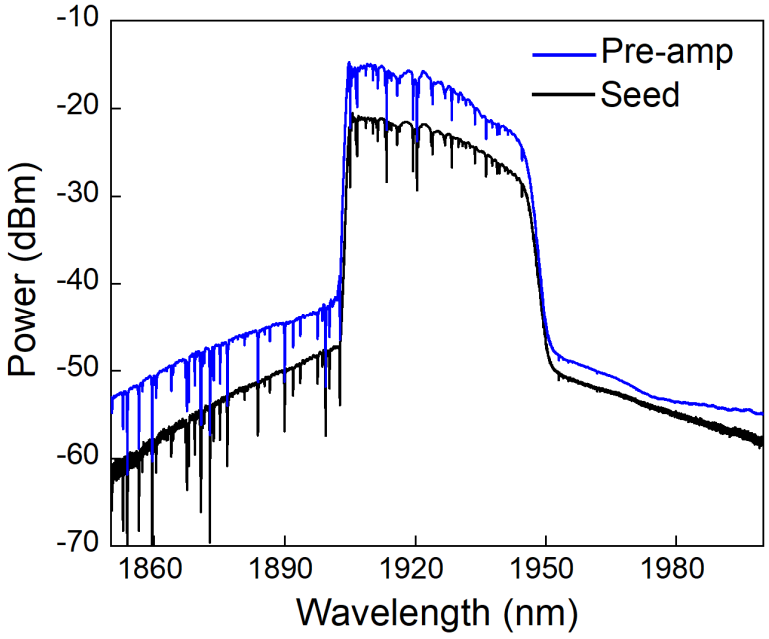

Fig. 4.2.8. The optical spectrum of the oscillator (black) and the pre-amplified (blue).

4.2.4 Power amplifier and grating compressor

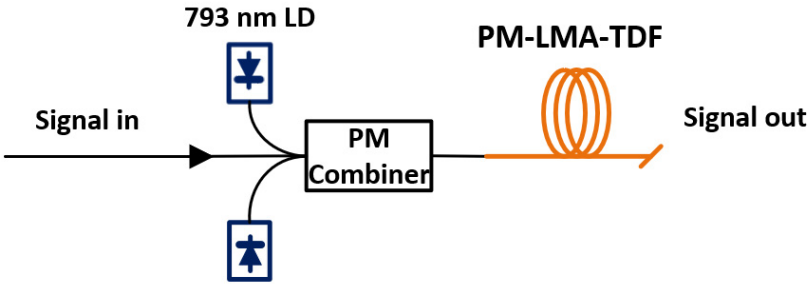

Fig. 4.2.9 Schematic of the power amplifier (forward pumping).

The power amplifier comprises a polarization maintaining large-mode-area (LMA) thulium doped fibre (Nufern PLMA-TDF-25P/400-HE) having a core / cladding diameter of 25 µm / 400 µm and NA of 0.09 / 0.46, with a length of 1.5 m and a cladding pump absorption of ~6 dB/m at 793nm. The pump diode (BWT Ltd.), mounted on a water-cooled aluminium base and monitored by a thermoelectric cooler (TEC), can provide a pump power of up to 30 W. Spectral and power characteristics of the pump diode are plotted in Fig.4.2.10. The pump laser emitted at 793 nm with a FWHM of 1 nm.

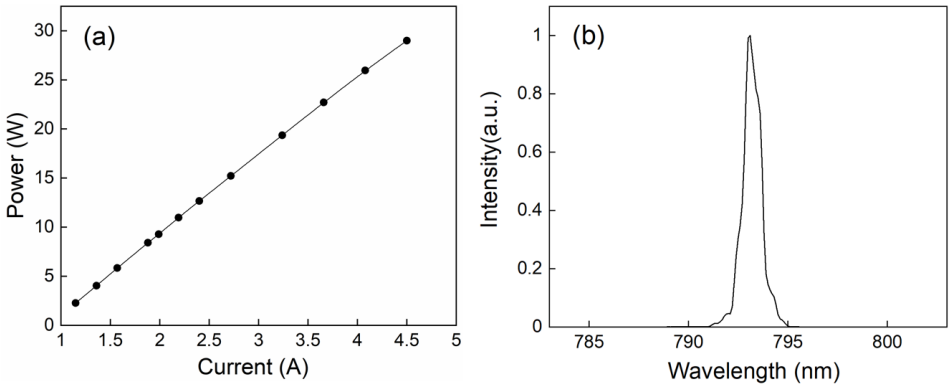

Fig. 4.2.10 (a) 793nm pump diode power and (b) spectral characteristics.

This thulium doped fibre has largest core size available commercially with V number of 3.5 (＞2.4), which means it works at a few modes area rather than single mode. It is well known that LMA fibers can support multiple transverse modes. Each one of the modes has a different bend loss. In general, higher order modes have higher bend loss than lower order modes at a specific bending diameter. In order to achieve improved output laser beam quality and suppress the gain in the higher order modes, proper coiling of the fiber is required to obtain fundamental mode operation by properly choosing the bending diameter of the fiber to introduce differential bend losses to different fiber modes. The mode-specific bend loss has been calculated by the “Rsoft” software. The Fig. 4.2.11 (left) presents the calculated LP_{01} and LP_{11} bend losses at 1925 nm vs. coil diameter for the Nufern PLMA-TDF-25P/400-HE fibre. In order to ensure high loss for the LP_{11} mode (＞10 dB/m) while keep extremely low loss for the LP_{01} mode (＜0.01dB/m) and cool the heat generation from the gain fibre, the LMA-TDF fibre was wrapped and cooled by a water-cooling cylinder with radius of 4 cm and a fixed temperature of 17°C as shown in the Fig. 4.2.11 (right). The free end of the LMA-TDF was terminated with an angle-polished core-less endcap (4°) to avoid signal feedback and to allow for signal beam expansion and reduction of peak intensity at the glass/air interface. The endcap was purged by nitrogen to lower its temperature and hence to resist potential thermal damage.

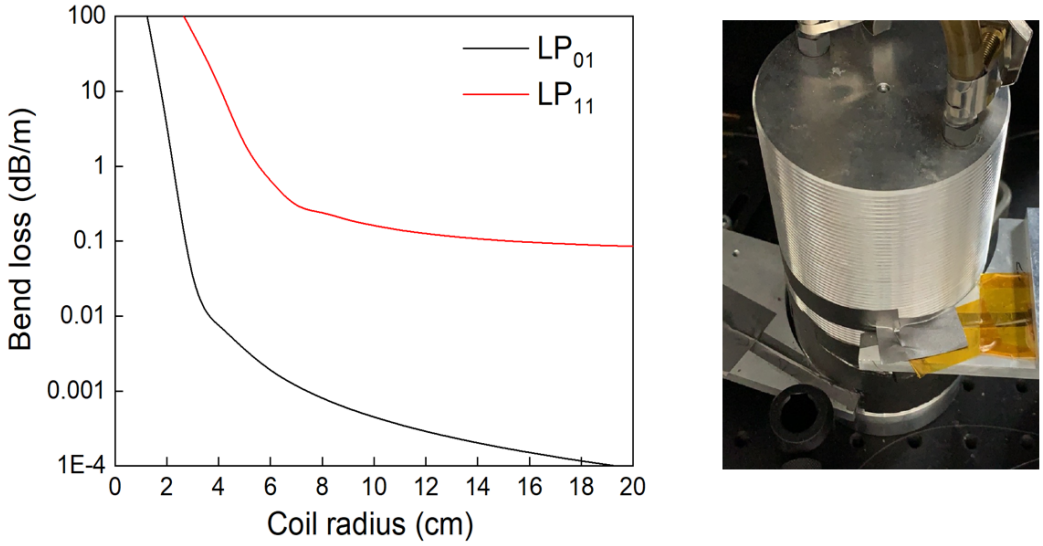

Fig. 4.2.11 (left) LP_{01} and LP_{11} bend losses vs. coil diameter for Nufern PLMA-TDF-25P/400-HE fibre. (right) Photo of the water cooling cylinder with radius of 4 cm.

I then tested a free-space reverse-pumped amplifier which both reduced the effective nonlinear length [18,19] and, as a bonus, shifted the gain peak to more closely align with that of the seed pulse spectrum. The Fig.4.2.12 provides the schematic of the power amplifier for backward version. Compared with forward pumping power amplifier, the input of this backward pumping power amplifier has a commercial mode filed adaptor (MFA) (AFR) to connect between PM1550 fibre (9 μm core) and LMA double-clad thulium doped fibre (25 μm core). A pair of lens was used to collimate and focus the pump laser beam into the doped fibre. A high transmission at 793 nm and high reflectivity at 1925 nm dichroic mirror (DM) was placed in between the lenses to separate the output signal beam and the residual pump laser beam.

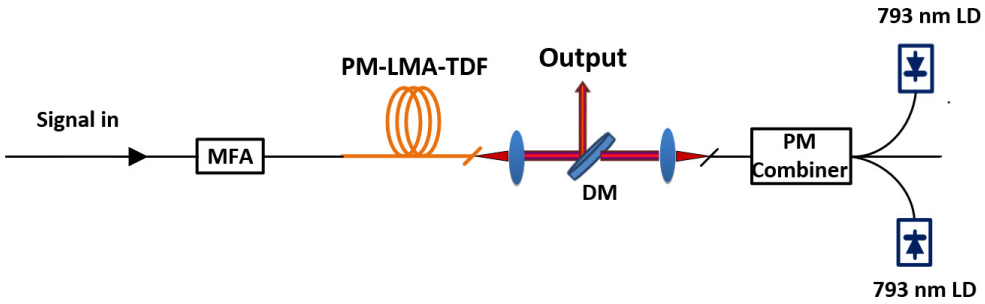

Fig. 4.2.12 Schematic of the power amplifier (backward pumping). MFA: mode field adaptor. DM: dichroic mirror.

The amplified pulses were collimated by a calcium fluoride lens (f=15 mm) and compressed by a pair of fused silica transmission gratings (Ibsen Photonics A/S) with 560 lines/mm and single pass transmission efficiency 94% across the 1900-2100 nm wavelength range. The width of the grating governs the maximum delay between short and long wavelength components, and for the pulses with 40 nm spectral bandwidth the 25 mm wide transmission grating can provide maximum -6.4 ps^2 of dispersion in the double pass setup. Through the eq.2.64, I calculated the distance between the two gratings should be 1.2 m in order to compress the chirped pulse from 105 ps to pulse-width of the transform limited pulse.

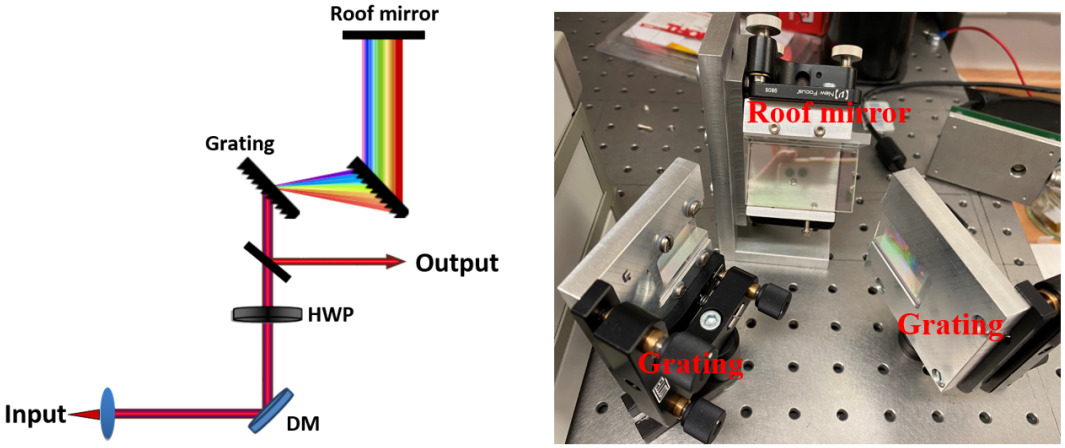

Fig. 4.2.13 (left) Schematic of the compressor. (right) Photo of the gratings and a roof mirror. DM: dichroic mirror; HWP: half-wave plate.

4.2.5 Experimental results and discussion

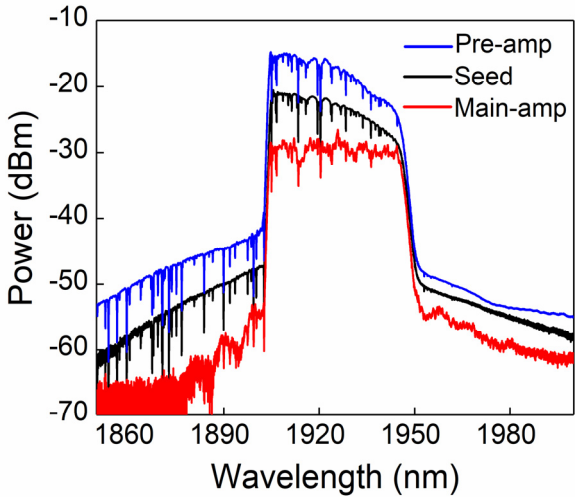

Fig. 4.2.14. The optical spectrum of the seed laser (black) and the pre-amplified (blue), main amplified pulses (red) at the maximum output power obtained with the forward pumped version of the power amplifier.

The stretched pulses were measured to have a deconvolved duration of 105 ps and were amplified to an average power of 180 mW in the pre-amplifier. The slope on the pre-amplifier spectrum was then compensated by the gain of the power amplification stage, giving the flat compressed output spectrum shown by the red line in Fig. 4.2.14. The peak voltage vs. the voltage of the background signal between pulses measured directly from the oscillator, pre-amplifier and the power amplifier using a 12.5 GHz photodetector (EOT ET-5000F) and our 1 GHz bandwidth analog oscilloscope (Tektronix 7104) was always greater than 28 dB (measurement limited by the dynamic range of the oscilloscope and detector dark current). With forward pumping, the power amplifier boosted the power to 28 W (17 kW peak power) using the full 104 W of available pump. The slope efficiency was 28% with respect to coupled pump power, as shown in Fig. 4.2.15(a). The residual pump at the fibre output when operating at the maximum power in this forward pump configuration was 13 W.

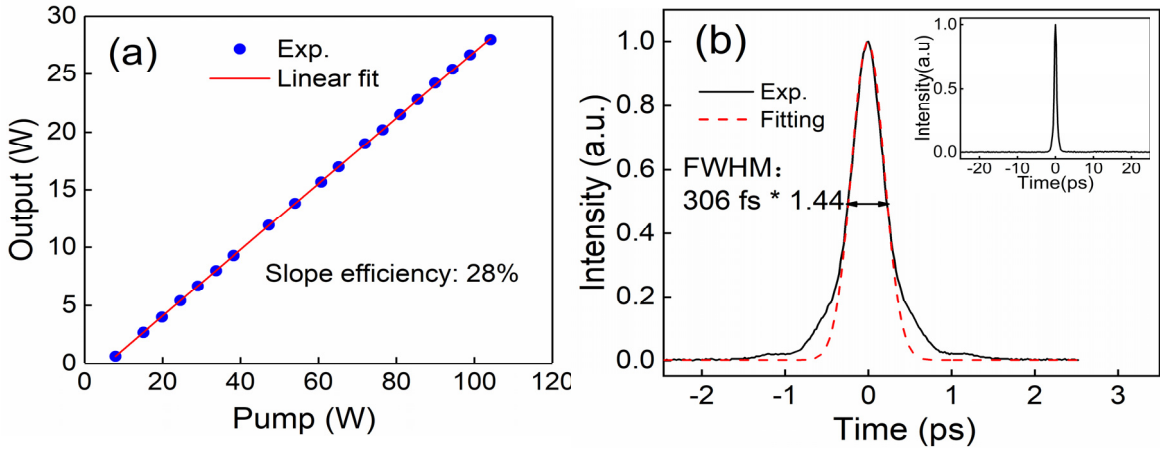

Fig. 4.2.15. Forward pumped amplifier results: (a) Amplified power (black dot) vs. incident pump power. (b) Autocorrelation trace for the pulse after compression at maximum compressed average power of 20 W. Inset: 50 ps span.

The total B-integral was calculated to be 1.85π (made up of 0.2π, 0.2π and 1.45π from fibre stretcher, pre-amplifier and power amplifier, respectively) through the eq. 2.55. By appropriate adjustment of the compressor grating separation, 306 fs duration pulses were obtained at the maximum compressed output power of 20 W (71.5% compressor transmission efficiency). The autocorrelation of the 1.27 μJ compressed pulses is shown in Fig. 4.2.15(b). The time bandwidth product (TBP) was calculated to be 0.99, which is 2.3 times the transform-limited value for a Gaussian pulse (0.44), but close to that of a transform-limited pulse with a rectangular-spectrum (0.88). It is worth noting that the TBP is nearly the same as when I recompressed the pulses emerging directly from the seed laser, indicating

both the excellent dispersion balance between the stretcher and compressor and the minimal impact from nonlinearity in the amplifier. Based on the autocorrelation data, I calculate that 82% of the pulse energy resides in the main peak, implying a pulse energy of 1.04 μJ and a peak power of 3.4 MW at the centre of the pulse.

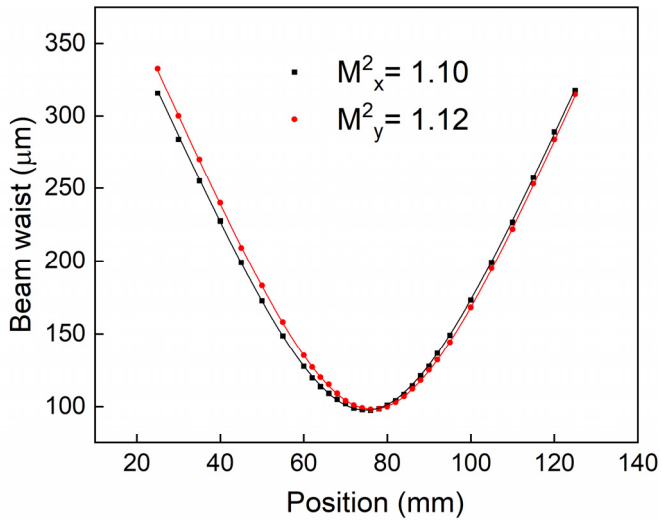

Fig. 4.2.16. Beam quality measurement of the compressor at maximum output power of 20 W.

I next investigated backward pumping which reduces the effective nonlinear length. Fig. 4.2.17(a) shows the spectral output from the oscillator, pre-amplifier and main amplifier. An output power of 30 W (shown in Fig. 4.2.17(b)) was achieved at the maximum pump power of 100 W, at a slope efficiency of 32% with respect to the incident pump power. This was somewhat higher than the 28% achieved with forward pumping because the gain peak was shifted to shorter wavelengths with backward pumping. The measured fibre output had M_x^2 and M_y^2 of 1.09 and 1.12. In addition, the spatial mode out of the compressor was measured to have M_x^2 and M_y^2 of 1.10 and 1.12 (as shown in Fig. 4.2.16), respectively. which indicates close to a pure-single-mode was achieved from the system.

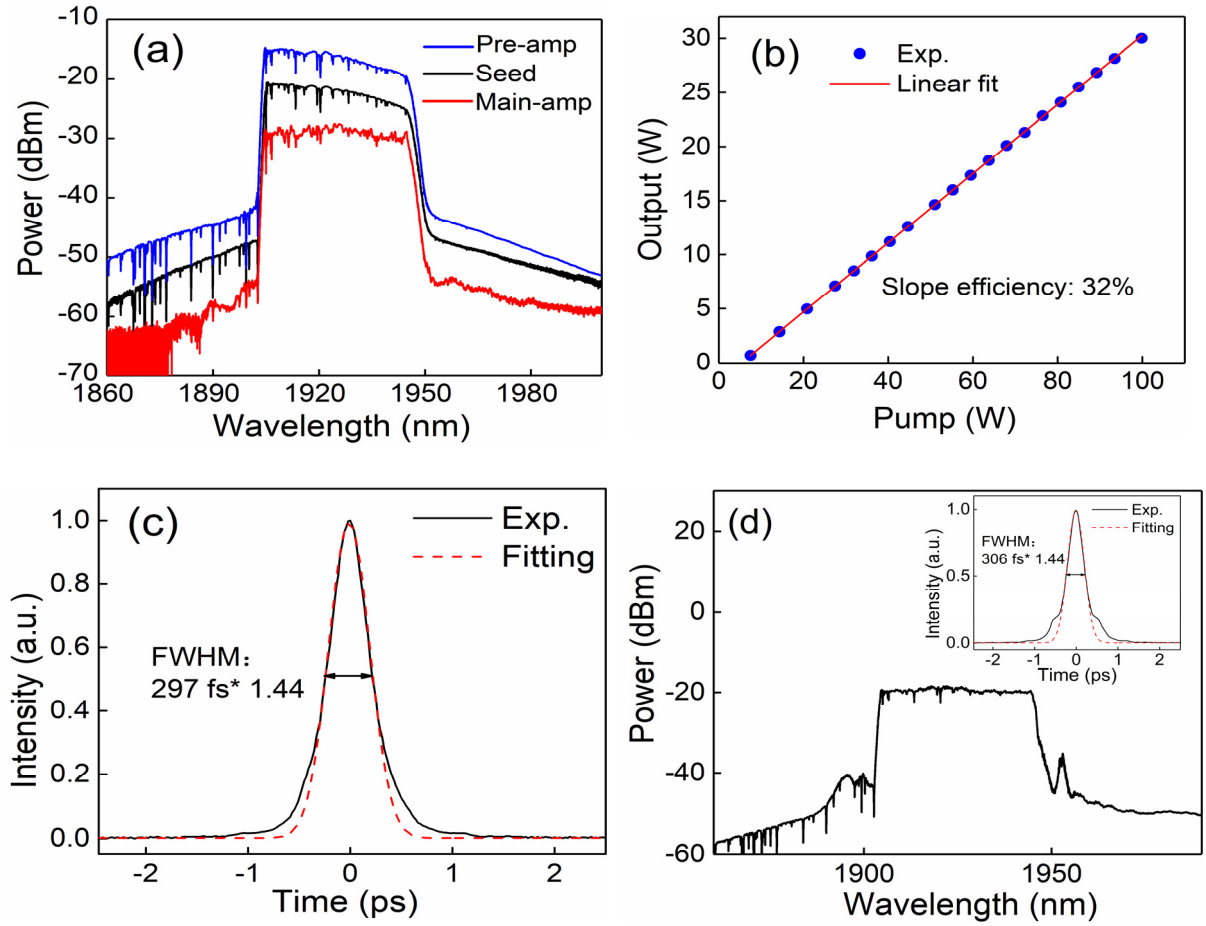

Fig. 4.2.17. Reverse pumping results. (a) Optical spectra after the oscillator (black), pre-amplifier (blue) and final amplifier amplified pulses (red) at the maximum output power using backward pumping. (b) Power (blue dot) from final amplifier vs. incident pump power. (c) Autocorrelation trace at maximum compressed average power of 21.5 W. (d) Optical spectrum with sidebands over nonlinear peak power threshold; inset shows corresponding compression pulse autocorrelation trace.

The pedestal on the AC due to nonlinear distortions when running at the maximum power is less pronounced with backward pumping (comparing Fig. 4.2.15(c) with Fig. 4.2.17(b)) and 91% of the energy remained in the main peak even though the power actually increased compared to forward pumping. The 21.5 W compressor output resulted in a corresponding pulse energy of 1.25 μJ and a peak power of 4.2 MW in the main peak, with a pulse duration of 297 fs, as shown in Fig. 4.2.17(c). The TBP of 0.96 is similar to the forward pumped result. The total B-integral of the system was calculated to have reduced to 1.15π (0.75π from the power amplifier) through eq. 2.55. OH absorption peaks are clearly observable in the spectra shown in Fig. 4.2.14 and Fig. 4.2.17. These originate from free space propagation

in air within the compressor (2.5 m total path length), and indeed within the OSA itself. However, autocorrelation trace data after the compressor indicates that the atmospheric gas absorption peaks do not severely affect the temporal pulse quality. Obviously, these absorption peaks could be avoided if desired by suitably controlling the gas environment in the compressor.

The maximum pulse energy in the system was limited by the available pump power not by nonlinear effects. In order to explore the nonlinearity threshold (i.e. maximum pulse energy before spectral distortions were observed). I therefore inserted a pulse picker followed by an extra pre-amplifier stage before the power amplifier to scale the peak power. The nonlinear peak power threshold of the power amplifier, estimated the appearance of spectral wings (shown in the inset to Fig. 4.2.17 (d)) on the pulses emerging directly from the fibre was 21 kW in the forward pumping embodiment and increased to 43 kW in the backward pumping scheme. This indicates that the theoretical maximum output peak-power of the compressed pulses from my system would be increased by a factor of ~2 to reach at 8.4 MW peak power after the compressor when using the backward pumping scheme. Further peak-power scaling beyond 10 MW would be enabled by employing a larger stretcher element in order to reduce the nonlinearity in the amplifiers at any given pulse energy. For example, this could be achieved with a longer stretcher fibre length; or using a double pass of the existing stretcher fibre; or by switching to a dispersion-tailored CFBG, and the new stretcher could be matched by e.g. a larger transverse dimension transmission grating pair or a CVBG compressor (Extending to those additional components was beyond my currently available resources).

4.3 CPA system based on core pumping a silica thulium-doped fibre

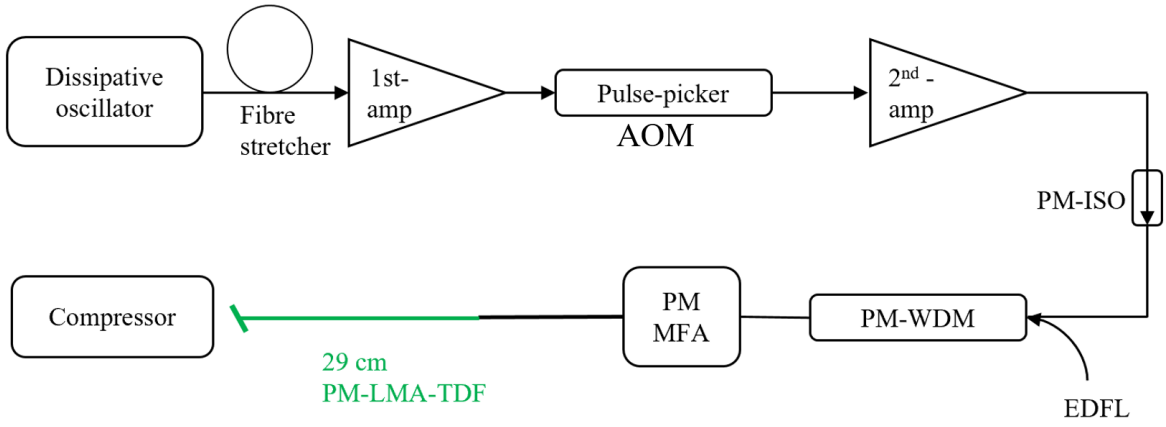

Fig. 4.3.1. Schematic of the CPA system based on core pumped thulium-doped fibre. AOM: acousto-optic modulator; Amp: amplifier; PM-ISO: polarization maintaining isolator; EDFL: erbium doped fibre laser; PM-WDM: polarization maintaining wavelength-division multiplexer; PM-MFA: polarization maintaining mode field adaptor; PM-LAM-TDF: polarization maintaining- large mode area-thulium doped fibre.

The core pumped CPA system is schematically illustrated in Fig. 4.3.1 while the dissipative soliton fibre oscillator, normal dispersion fibre-based stretcher and 1st pre-amplifier have all been described previously. Fig. 4.3.2 (black line) shows the spectrum of the dissipative oscillator with a centre wavelength of 1923 nm and a bandwidth of ~47 nm. It is worth noting that I optimised the oscillator's spectral shape to match with the flat gain profile in the following amplifiers. A fibre coupled polarisation dependent acousto-optic modulator (AOM) (G&H, T-M250-0.3C16Z-3-F2P) with a 4 dB insertion loss (1.5 mW output) and over 50 dB extinction ratio play the role of pulse-picker to reduce the repetition rate from 15.7 MHz to 0.39 MHz.

In Fig. 4.3.2 (blue), spectral modulation after AOM can be seen due to the degree of depolarisation in the long length of non-PM stretcher fibre. In addition, a second pre-amplifier was needed to boost the power into the final amplifier. The use of a 1560 nm core pumped 30 cm long PM Tm-silica fibre with a 10 μm core diameter (Nufern) minimised the nonlinear effects and resulted in an average power of 50 mW (Fig. 4.3.2 (red)). In order to core pump a 29 cm PM double-clad (DC) TDF with a 25 μm core diameter in the final amplifier, a mode field adaptor (AFR) was inserted after the PM-WDM (Lightcomm). The 1565 nm EDFL pump laser (SPI) had a maximum power of 10 W.

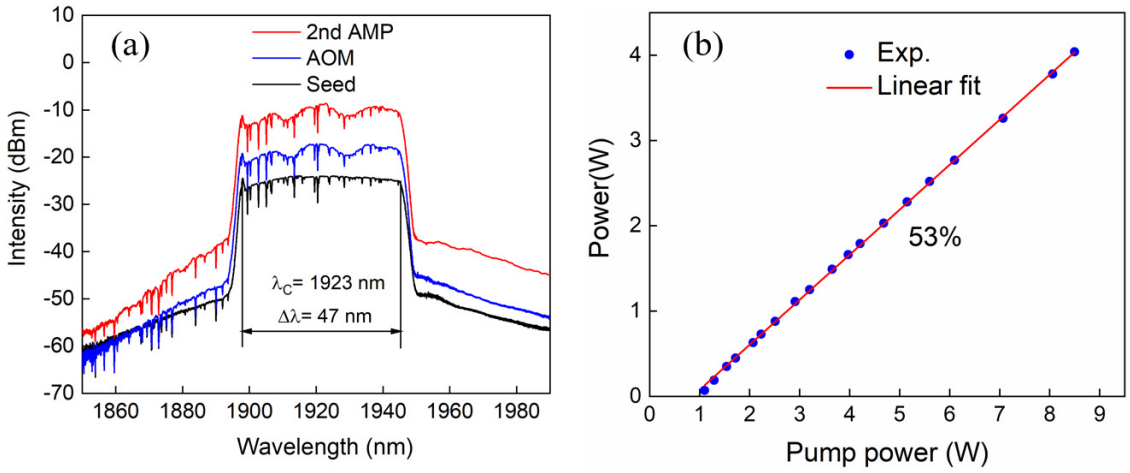

Fig. 4.3.2 (a) The optical spectrum of the seed laser (black) and the AOM (red), 2nd amplifier pulses (blue). (b) Power (blue dot) from final amplifier vs. incident pump power

Fig. 4.3.3(a) describes the amplified pulses spectra in the power amplifier for different average output powers, from 4 to 4.6 W. As can be seen, the spectral side wings broadening induced by nonlinear effects (mainly from modulation instability) limited the maximum average output power to 4 W when at a pump power of 8.5 W with a launched pump slope efficiency of 53% (Fig. 4.3.2 (b)). Even when at a 4.9 W output power, there is no indication of a Raman peak for the amplified pulses, as is shown in Fig. 4.3.3(b).

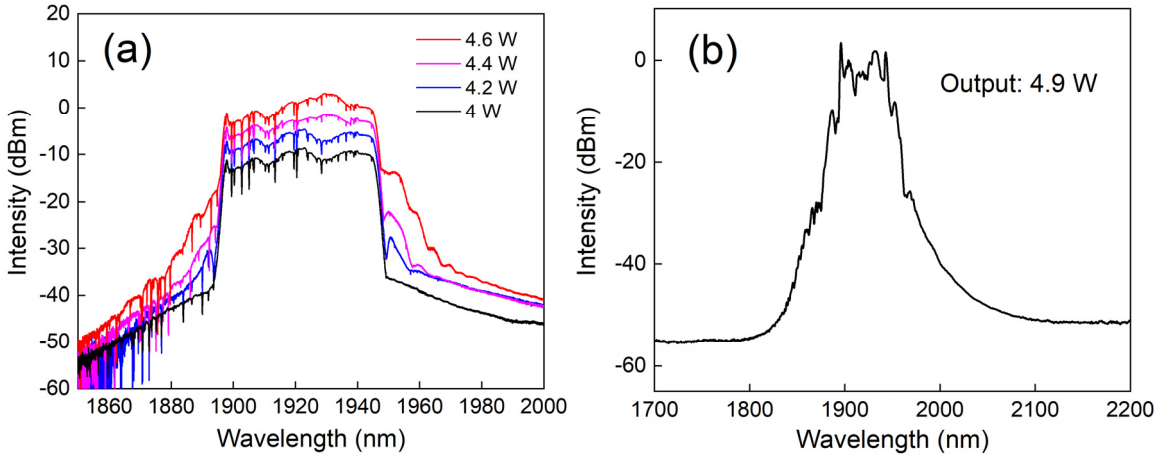

Fig. 4.3.3. Pulses spectra in the power amplifier for different output power. (a) 4W(black), 4.2W(blue) 4.4W(pink) and 4.6W(red). (b) 4.9W at broaden scanning range.

With the appropriate grating separation, the compressed pulse duration was measured with a SHG autocorrelator (APE Pulse-check) and shown to reach 285 fs at the maximum compressed output power of 2.8 W (71% compressor transmission efficiency), as shown in

Fig. 4.3.4. In addition, the time bandwidth product (TBP) was calculated to be 1.04, which is slightly higher than the cladding pump version (0.99). Based on the autocorrelation data, I calculate that 80% of the pulse energy resides in the main peak, implying a pulse energy of 5.7 μJ and a peak power of 20 MW at the centre of the pulse. This peak power value is the highest number for this type of CPA system based on simple conventional fibre.

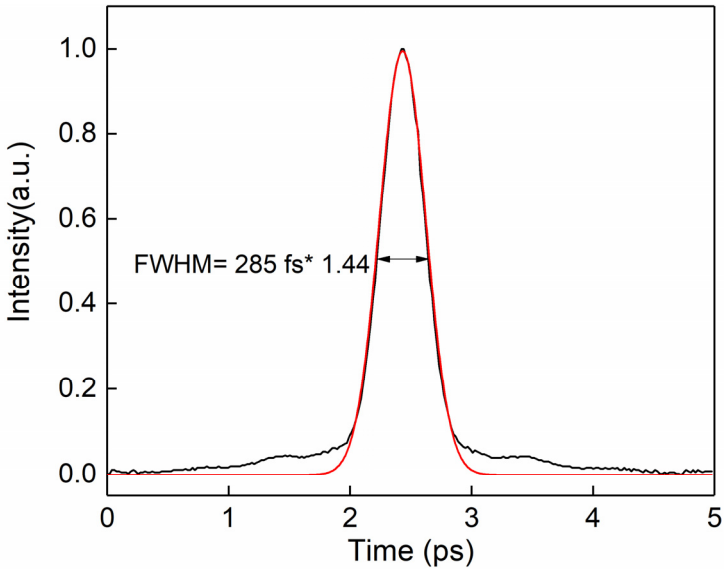

Fig. 4.3.4. Core pumped CPA autocorrelation at maximum power of 2.8W.

4.4 Summary

In conclusion, I have demonstrated a high-peak-power, high energy silica thulium-doped fibre CPA system through both the cladding and core pumping schemes. The output results were shown in the table 4.4.1.

Cladding pumping a 1.5 m TDF produced 297 fs compressed pulses with an average power of 21.5 W and a peak power of 4.2 MW at a repetition rate of 15.7 MHz. The chirped 25 ps pulses from the seed laser helped to reduce the nonlinear phase accumulation in the fibre-based stretcher. After using the reverse pumped final amplifier configuration to amplify the pulses, I found that it was when using the forward pumped final amplifier configuration that there was a significant increase in energy, reaching in fact the maximum energy obtainable. In addition, backward pumping improved the compressed pulse quality, increasing the fraction of the energy in the main peak from 82% to 91%. Tests at lower repetition rates also showed that further significant pulse energy scaling was achievable before the nonlinear effects would strongly distort the pulses.

Core pumping a 29 cm TDF produced 285 fs pulses with an average power of 2.8 W and a peak power of 20 MW at a repetition rate of 0.39 MHz. Compared with the cladding pump scheme, core pumping a length of fibre that is 5 times shorter than that used in the cladding pumping leads to a significantly improved pulse peak power, increasing from 4.2 MW to 20 MW (~ 5 times) but sacrificing compactness, cost and repetition rate (average power).

Currently, peak power scaling is limited in my case, by the nonlinearity (modulation instability) from the power amplifier. There are two general methods to minimise the nonlinearity accumulation in the active fibre, these are to shorten the fibre length and increase the mode area. However, in terms of the simple fibre, the thulium doped fibre used in my power amplifier has the largest mode area and the highest doping concentration among commercial, and unfortunately, there is not a lot of room for scaling pulse peak power in these types of fibres. Therefore, the next chapter will address the nonlinearity issues by using an in-house highly doped germanate TDF to shorten the fibre length.

Table 4.4.1 CPA results of the cladding and core pumped silica TDF in the power amplifier

	Cladding pumped version	Core pumped version
Average power	21.5 W	2.8 W
Peak power	4.2 MW	20 MW
Repetition rate	15.7 MHz	0.39 MHz
Pulse energy	1.25 μJ	5.7 μJ
Pulse-width	297 fs	285 fs
Length of the gain fibre	1.5 m	0.29 m
Amplifier stages	2	3

Reference

[1] R. G. Frehlich, S. M. Hannon, and S. W. Henderson, “Performance of a 2-μm coherent Doppler lidar for wind measurements,” J. Atmos. Ocean. Technol., **11**(6), 1517–1528 (1994).

[2] W. Shi, E. Petersen, N. Moor, A. Chavez-Pirson, and N. Peyghambarian "All fiber-based single-frequency Q-switched laser pulses at 2 μm for lidar and remote sensing applications," Proc. SPIE 8164, 81640M (2011).

[3] V. Konov, “Laser in micro and nanoprocessing of diamond materials,” Laser & Photon. Rev. **6**(6), 739-766 (2012).

[4] Q. Fu, L. Xu, S. Liang, D. P. Shepherd, D. J. Richardson and S. Alam, "Widely Tunable, Narrow-Linewidth, High-Peak-Power, Picosecond Midinfrared Optical Parametric Amplifier," IEEE J. Quantum Electron, **24**(5), 1-6 (2018).

[5] M. P. Arpin, T. Popmintchev, M. Gerrity, B. Zhang, M. Seaberg, D. Popmintchev, M. M. Murnane, and H. C. Kapteyn, “Bright, coherent, ultrafast soft X-ray harmonics spanning the water window from a tabletop light source,” Phys. Rev. Lett., **105**(17), 173901 (2010).

[6] E. A. Peralta, K. Soong, R. J. England, E. R. Colby, Z. Wu, B. Montazeri, C. McGuinness, J. McNeur, K. J. Leedle, D. Walz, E. B. Sozer, B. Cowan, B. Schwartz, G. Travish, and R. L. Byer, “Demonstration of electron acceleration in a laser-driven dielectric microstructure,” Nature **503**(7474), 91–94 (2013).

[7] F. Stutzki, C. Gaida, M. Gebhardt, F. Jansen, A. Wienke, U. Zeitner, F. Fuchs, C. Jauregui, D. Wandt, D. Kracht, J. Limpert and A. Tünnermann, "152 W average power Tm-doped fiber CPA system," Opt. Lett. **39**(16), 4671-4674 (2014).

[8] A. Klenke, S. Breitkopf, M. Kienel, T. Gottschall, T. Eidam, S. Hädrich, J. Rothhardt, J. Limpert, and A. Tünnermann, “530 W, 1.3 mJ, four-channel coherently combined femtosecond fiber chirped-pulse amplification system,” Opt. Lett. **38**(13), 2283–2285 (2013).

[9] A. Klenke, M. Müller, H. Stark, F. Stutzki, C. Hupel, T. Schreiber, A. Tünnermann, and J. Limpert, "Coherently combined 16-channel multicore fiber laser system," Opt. Lett. **43**(7), 1519-1522 (2018).

[10] R. A. Sims, P. Kadwani, A. L. Shah and M. Richardson, "1 μJ, sub-500 fs chirped pulse amplification in a Tm-doped fiber system," Opt. Lett. **38**(2), 121-123 (2013).

[11] H. Hoogland and R. Holzwarth, "Compact polarization-maintaining 2.05-μm fiber laser at 1-MHz and 1-MW peak power," Opt. Lett. **40**(15), 3520-3523 (2015).

[12] C. Gaida, M. Gebhardt, T. Heuermann, F. Stutzki, C. Jauregui, and J. Limpert, "Ultrafast thulium fiber laser system emitting more than 1 kW of average power", Opt. Lett. **43**(23), 5853-5856 (2018).

[13] F. Tan, H. Shi, P. Wang, J. Liu, P. Wang, "Chirped pulse amplification of a dissipative soliton thulium-doped fiber laser," Proc. SPIE 9728, 97280Y (2016).

[14] D. Gaponov, L. Lavoute, S. Février, A. Hideur, and N. Ducros, "2μm all-fiber dissipative soliton master oscillator power amplifier," Proc. SPIE 9728, 972834 (2016).

[15] Z. Ren, Q. Fu, L. Xu, J. H. V. Price, S. Alam, and D. J. Richardson, “Compact, high repetition rate, 4.2 MW peak power, 1925 nm, thulium-doped fiber chirped-pulse amplification system with dissipative soliton seed laser,” Optics Express, **27** (25), 36741-36749 (2019).

[16] P. Elahi, H. Kalaycioğlu, Ö. Akçaalan, Ç. Şenel, and F. Ö. Ilday, "Burst-mode thulium all-fiber laser delivering femtosecond pulses at a 1 GHz intra-burst repetition rate," Opt. Lett. **42**(19), 3808-3811 (2017).

[17] P. Yin, J. Serafini, Z. Su, R. Shiue, E. Timurdogan, M. Fanto, and S. Preble, "Low connector-to-connector loss through silicon photonic chips using ultra-low loss splicing of SMF-28 to high numerical aperture fibers," Opt. Express **27**, 24188-24193 (2019).

[18] S. Liang, L. Xu, Q. Fu, Y. Jung, D. P. Shepherd, D. J. Richardson, and S.-U. Alam, “295-kW peak power picosecond pulses from a thulium-doped-fiber MOPA and the generation of watt-level >2.5-octave supercontinuum extending up to 5 μm,” Opt. Express **26**(6), 6490–6498 (2018).

[19] G. J. Spühler, T. Südmeyer, R. Paschotta, M. Moser, K. J. Weingarten, and U. Keller, “Passively mode-locked high-power Nd:YAG lasers with multiple laser heads,” Appl. Phys. B **71**(1), 19–25 (2000).

[20] C. Hönninger, R. Paschotta, F. Morier-Genoud, M. Moser, and U. Keller, “Q-switching stability limits of continuous-wave passive mode locking,” J. Opt. Soc. Am. B **16**(1), 46–56 (1999).

[21] A. Chong, J. Buckley, W. Renninger, and F. Wise, "All-normal-dispersion femtosecond fiber laser," Opt. Express **14**(21), 10095-10100 (2006).

Chapter 5

Compact chirped- pulse amplification systems based on highly Tm3+ doped germanate fibre

5.1 Introduction

High power ultra-short pulse laser sources in the 2 μm wavelength range are gaining more and more attention for use in applications including free space optical communications [1], sensing [2], material processing [3] and mid-IR generation [4]. They are also proving promising for fundamental research in fields such as high harmonic generation [5] and laser-driven electron acceleration [6]. Rod-type Tm-doped fibres [7,8] have been used to achieve the highest pulse energies (mJ level), peak/average powers (GW/kW) to date. However, many important practical applications, including material processing and power scaling of mid-IR light generation, do not require such levels of performance and consequently there is appreciable commercial interest in more practical, compact sources based around more conventional flexible fibre technology with relatively simple physical configurations.

The current performance records for compact, high power Tm-based ultrafast fibre laser systems have been set by using conventional silica fibres. For example, Wan et al. demonstrated a CPA system, which achieved an output average power of 32 W by using 650 meters of fibre stretcher and 4.5 m LMA fibre [9]. The generation of 0.15 μJ energy, 0.5 MW peak power, 256 fs pulses was demonstrated by Haxsen et al. using a 2.8 m LMA fibre [10]. By increasing the stretched pulse duration to 160 ps, Sims et al. used a 3.3 m LMA fibre to achieve 1 μJ, 3 MW peak power pulses [11]. Hoogland et al. demonstrated a compact CPA system, which generated pulses with 1 MW peak power and 371 fs duration with a 3.4 m LMA fibre amplifier [12]. All these silica fibre based results required active fibre lengths above 1 m, which resulted in limited pulse-energy/peak-power scaling due to the appearance

of detrimental nonlinear effects including modulation instability and spectral broadening from self-phase modulation (SPM).

Although silica glass is clearly both the dominant and most technologically developed host material for fibre lasers, due largely to its combination of favorable mechanical and glass-drawing characteristics, it has low rare-earth ion solubility, which limits the scope for reducing the lengths of active fibre in lasers and amplifiers. The maximum Tm3+ doping concentration in pure silica fibre is 10^{18} - 10^{19} ions/cm^3 [13]. Higher doping levels (10^{20} ions/cm^3) can be realized through the addition of co-dopants such as aluminum or phosphorous [14], but these substantially increase the core refractive index relative to a pure-silica cladding, so cores with a surrounding pedestal structure are required to create the low index step needed in LMA designs. The need for this refractive index pedestal makes fabrication more complex [15]. In contrast, heavy metal oxide glasses such as germanate and fluoride have much higher Tm^{3+} solubility with concentrations of 10^{21} ions/cm^3 being readily achievable without the addition of co-dopants. The resulting promise of shorter device lengths should reduce the impact of detrimental nonlinearities in pulsed laser systems. Germanate and fluoride glasses systems can be easily and directly index-matched to pure cladding glasses enabling simplified LMA fibre design and fabrication. Here I focus on germanate glass, which has a nonlinear index approximately twice that of pure silica, so a reduction in device length by approximately that factor is required to compete with silica devices.

The other concern with silica glass is its high phonon energy of ~1100 cm^{-1}, which results in fast multiphonon relaxation in the mid-IR, where it becomes opaque, and can also lead to a low cross-relaxation rate and thus reduction in quantum efficiency when pumping thulium at 793 nm [16]. Fluoride glasses have very low phonon energy of around 500 cm^{-1} but are not widely used in high power lasers due to their low mechanical strength, low damage threshold and the difficulty of splicing such fibres to silica fibres. In contrast, germanate glasses possess a relatively low phonon energy of ~ 845 cm^{-1} and offer better mechanical strength than fluoride glasses. Hence germanate fibre is attractive for laser transitions at long wavelengths that would not be useable in a silica glass host fibre. The outstanding challenges for realizing practical germanate fibres are in the fabrication of a glass with the lowest possible levels of impurities and in the preparation of a preform and fibre that do not suffer

from crystallization so as to minimize propagation losses and achieve optimal laser performance.

Some good laser results with germanate fibres have already been achieved. Wen et al. demonstrated a single-frequency fibre laser at 1.95 μm using just 1.6 cm of a highly Tm doped ($7.6*10^{20}$ ions/cm^3) barium gallo-germanate (BGG) single mode (SM) fibre but with a low output power (35 mW) and even moving to a length of 10 cm for multi-longitudinal-mode laser operation only 165 mW of output power was achieved with a moderate slope efficiency (17%) [17]. Fang et al. demonstrated a nanosecond-pulsed 2 μm single frequency master oscillator power amplifier (MOPA) using 41 cm of large core (30 μm) Tm-doped germanate fibre, obtaining a record output average power of 16 W and peak power of 73 kW [18]. However, their amplification slope efficiency of 17% was again low due to a high background loss of 5 dB/m in their fibre.

In this chapter, I first present the fabrication of a 1st generation dual cladding large mode area (LMA) thulium doped germanate fibre (TDGF), the fibre design and fabrication work was mainly carried out my colleague Dr. Fedia. The fibre has a core diameter of 20 μm, a high Tm^{3+} ion concentration of $3\times10^{20}/cm^3$ and a hexagonal inner-cladding to enhance pump absorption when cladding pumped. Using the short length of TDGF, I demonstrated a record combination of peak and average power in a compact 300 fs chirped-pulse amplification (CPA) system operating at 1925 nm. By cladding pumping a 65 cm length of TDGF, I produced an average power of 14.1 W (limited by thermally induced damage) and a peak-power of 2.55 MW at a pulse repetition rate of 15.7 MHz. Core pumping a 19 cm length of TDGF meanwhile, produced an average power of 2.3 W and 17 MW peak-power pulses at a repetition rate of 0.39 MHz. At this stage, the performance was already comparable to the state-of-the-art performances achieved with flexible silica fibres. I next investigated the pulse energy and peak power scaling results from core pumping a shorter length (9.5 cm) of 2nd generation TDGF in the power amplifier. The system was able to generate 240 fs pulses with an energy of 12 μJ, an average power of 1.9 W and a peak power of 42 MW. Cladding pumping a 30 cm length of TDGF meanwhile, produced an average power of 2.8 W and peak-power pulses of 0.156 MW.

Section 5.2 and 5.3 describe the respective compact high-power cladding/core pumping CPA system through 1st and 2nd generation TDGF in the power amplifier. Finally, section 5.4

summarises this chapter and gives a concluding remark. The work described in this chapter has previously been published in [19].

5.2 CPA system based on 1st generation of Tm^{3+} germanate doped fibre

5.2.1 1st generation of germanate Tm^{3+} doped fibre

For the development of TDGF, the germanate core glass (Ge-01) and cladding glass (Ge-02) were both made in-house using the melt-quenching technique from the chemical composition of $58GeO_2$-14.4PbO-13ZnO-$4Nb_2O_5$-$7Na_2O$-$1.5SiO_2$-$1.5Al_2O_3$-$0.6Tm_2O_3$ (core glass) and $58GeO_2$-15PbO-13ZnO-$4Nb_2O_5$-$7Na_2O$-$1.5SiO_2$-$1.5Al_2O_3$ (cladding glass) [19]. The combination provided the low refractive index contrast necessary for single mode LMA fibre operation and compatibility, in terms of the thermo-mechanical properties needed for successful fibre drawing. We achieved a high Tm^{3+} concentration of $3*10^{20}$ ions/cm^3, a large core diameter of 20 µm and low numerical aperture (NA =0.07) which, together, enabled a robust SM operation (LP01 mode) at 1925 nm with cut off wavelength of 1830 nm. The fabrication processes for the germanate glasses and TDGF were similar to the process described in our report on a TDGF with a circular inner-cladding [20].

As the table 5.2.1 shows, thanks to the fact that the compositions of PbO, ZnO and Nb_2O_5 have large normal material dispersion parameters at 2µm, and the major composition of GeO_2 has zero dispersion at 1.73 µm and -29.8 fs^2/mm at 2 µm, the material dispersion of our fibre is estimated to have normal dispersion with 2.54 fs^2/mm.

Table 5.2.1 Composition of the TDGF dispersion at 2µm [100]

Chemical composition in the glass	**Dispersion (fs^2/mm)**
GeO_2	-29.8
PbO	140
ZnO	68
Nb_2O_5	100
Na_2O	21
SiO_2	-100
Al_2O_3	-122
Tm_2O_3	100

In addition, the calculated waveguide dispersion of TDGF is 2 fs^2/mm at 2μm through "Rsoft". Therefore, the GVD of the fibre (material dispersion plus waveguide dispersion) is estimated to be 4.54 fs^2/mm at 2μm.

To create the hexagonal cladding, a Ge-02 glass billet was extruded from a hexagonal tube of 9.5 mm outer diameter (across 2 opposite angles) and 1.8 mm inner diameter using the same extrusion process described in our previous work [19]. A hexagonal inner cladding shape was chosen to break the symmetry of the inner cladding and to facilitate low-loss splicing to passive fibre having a circular cross section. Separately, a 120 mm long and 11.5 mm diameter Tm-doped Ge-01 glass rod was pre-drawn into a cane of 1.3 mm diameter before insertion into the hexagonal cladding glass tube. The Ge-01 cane and Ge-02 hexagonal glass tube were then co-drawn into an optical fibre using a rod-in-tube technique (Fig. 5.2.1 left). The fiber core and cladding diameters were 20±0.5 μm and 126±1 μm (across 2 opposite angles), respectively. The fibre had estimated nonlinear index of $n_2=5.5\times10^{-20}$ $m^2\cdot W^{-1}$ with nonlinear parameters of $\gamma = 0.69$ ($W^{-1}\cdot km^{-1}$) which is 2.3 times higher than the commercial silica based thulium doped fiber ($\gamma = 0.3$ ($W^{-1}\cdot km^{-1}$)) used in chapter 4 [21].

As shown in Fig. 5.2.1 right, there are no signs of residual stresses or bubbles at the interface between the core and cladding, which demonstrates the excellent quality of the drawing process. A UV curable low index acrylate polymer coating around the hexagonal cladding was added to provide mechanical protection and to allow the fibre to be cladding pumped by confining the pump power in the inner cladding. The fibre propagation loss was measured to be ~1dB/m at 980 nm using the cut-back method, matching the lowest loss achieved for germanate glass fibre we reported earlier [20] and confirming the good reproducibility we have achieved in fabricating the high quality germanate glass material and the excellent control we have of the fibre fabrication process.

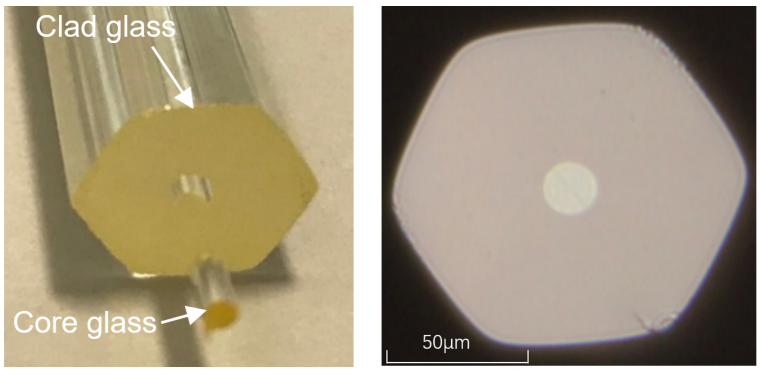

Fig. 5.2.1. (left) Cross sectional view of the extruded hexagonal inner cladding with the core rod extending outwards from the front face. (right) Optical microscope image of the fabricated Tm doped germanate LMA single mode fibre.

5.2.2 Experimental results and discussion

5.2.2.1 Cladding pumping for 1st generation of TDGF

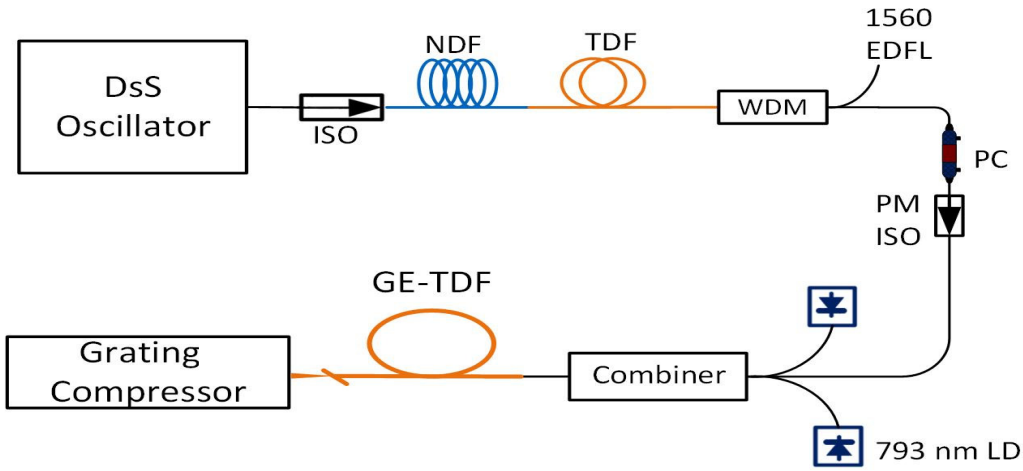

Fig. 5.2.2. Schematic diagram of the CPA system. DsS-dissipative soliton, NDF-normal dispersion fibre, WDM-wavelength-division multiplexer, PC-polarization controller, EDFL-Er doped fibre laser.

The cladding pumped CPA system is illustrated schematically in Fig. 5.2.2. It comprises a fibre oscillator, fibre stretcher, two amplifier stages and a bulk grating-based compressor. The dissipative soliton fibre oscillator was described in the last chapter and provides chirped laser output pulses with a width of 25 ps, at a central wavelength of 1925 nm (39 nm bandwidth) and at a repetition rate of 15.7 MHz. The average power output power was 40 mW (corresponding to a pulse peak power of 102 W). The pulses were attenuated to an average power of 3 mW to minimise the nonlinearity in the stretcher, which consisted of 58 m of UHNA7 (Nufern) and 25 m of UHNA4 (Nufern) fibres. This combination of fibre

lengths was chosen to cancel the overall third order dispersion and to produce stretched pulses with a duration of 140 ps [21]. These were amplified to an average power of 150 mW in a 1.5 m Tm doped silica fibre (OFS, TmDF200) which was then backward core-pumped with a power of 400 mW at 1560 nm so as to minimise the effective nonlinear length [22,23]. To obtain the single polarisation required for our transmission grating-based compressor, I used a polarisation maintaining (PM) fast-axis blocking isolator preceded by an in-line polarisation controller (FIBERPRO PC1100) between the pre- and power-amplifier stages. Due to a slight depolarisation in the fibre stretcher the power reduced from 150 mW to 110 mW, even following a precise adjustment of the PC. The final power amplifier was comprised of a 65 cm TDGF which was cladding pumped by two 30 W multimode-diodes (BWT) at 793 nm through a 130 µm cladding-diameter silica fibre-based combiner (Lightcomm) with a 10 µm core-throughput. The cladding absorption was 20 dB/m at 793 nm and the TDGF length was chosen to obtain a suitably centred spectral gain profile and good amplifier efficiency. The TDGF's mode field diameter at 1925 nm was 22.6 µm. It is worth noting that germanate fibre with normal dispersion is beneficial for nonlinearity management in the amplifier. The measured splicing losses between the TDGF and the combiner fibre were <1.2 dB (due to the mode field diameter mismatch) and 0.2 dB, respectively, for the core and cladding. In addition, as germanate fibres have a lower melting temperature than silica glass, an offset-arc splicing technique (i.e., offsetting the arc position from the splicing location) was used. The splice was then re-coated with low index polymer (Fig.5.2.3 left), the TDGF was mounted onto a water-cooled plate and graphite sheets (Fig.5.2.3 right) were applied to assist in the overall thermal management.

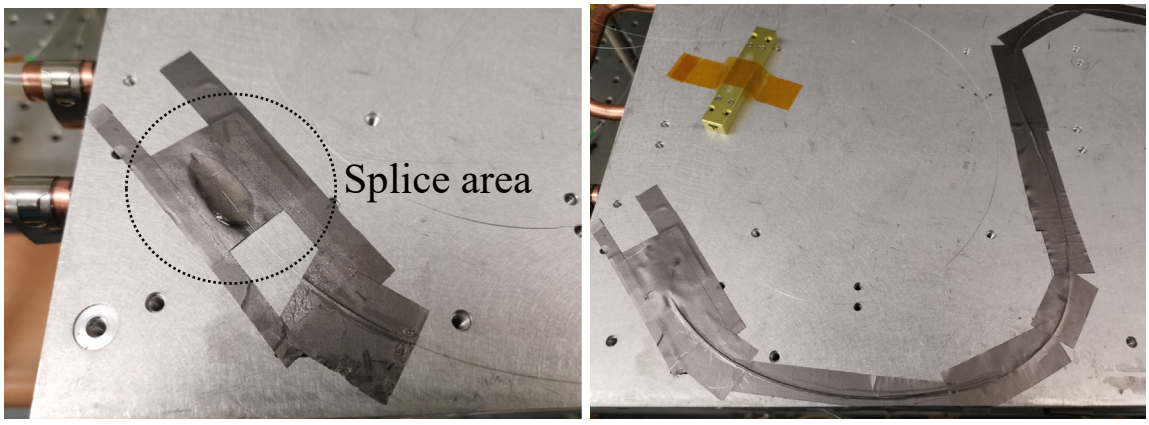

Fig. 5.2.3. (left) Photo of the splicing point was re-coated with low index polymer. (right) Photo of the TDGF was covered with graphite sheets and water-cooled plate.

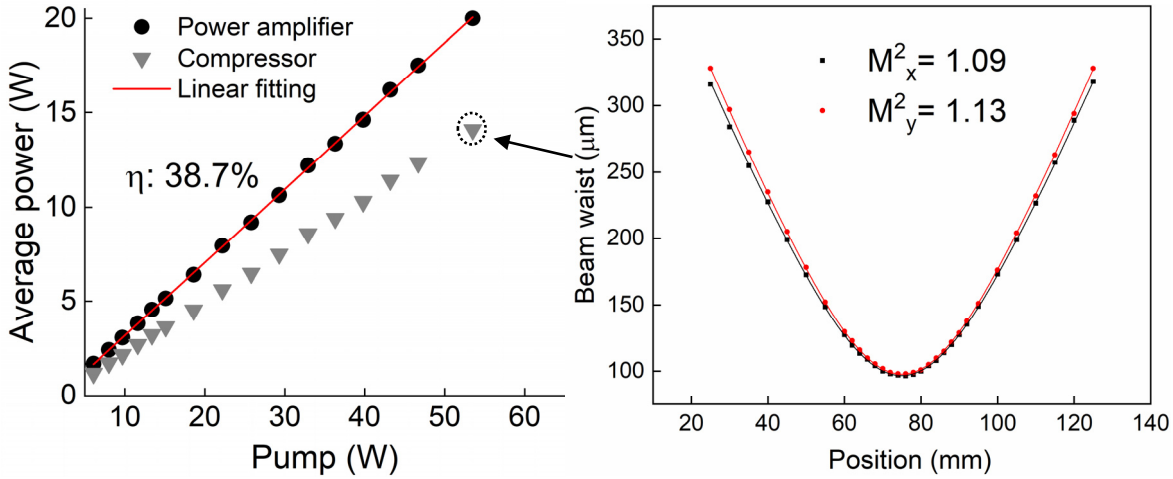

Fig. 5.2.4. (left) Measured average output power after the power amplifier and compressor gratings versus launched pump power. (right) Measured beam quality at the maximum output power of 14.1 W (after the compressor).

Although the available pump power was 60 W, the TDGF fibre became damaged (points closed to the pump facets ~ 1 cm) when reaching pump powers above 53 W (I observed this on 5 separate occasions when reaching the ~50W power level). I also saw the same effect when the pulsed seed was replaced with a cw-seed laser and I therefore concluded that this was due to thermal damage rather than self-pulses lasing. In order to analyze the heat load of the TDGF, the temperature distribution of our fibre (fibre length=65 cm) is simulated using a COMSOL Multiphysics at cladding pump power of 50 W. As shown in the Fig.5.2.5, the fibre coating temperature is already close to 103°C, which limits the further power scaling in the experiment. The accumulated head load in the core and cladding is estimated to be ~47.2 W/m and ~10.7 W/m, respectively. Improved cooling arrangements may therefore enable further power scaling, which for the cladding pump power could even increase over 4 times [22], but I am not yet to investigated this. The maximum amplifier output was consequently limited to 20 W and the slope efficiency was 38.7 % (see Fig. 5.2.4 (left)), which was well above the 32 % I achieved using the same basic set up and a commercial Tm-doped silica fibre in earlier work [20]. The total B-integral of the system was calculated to be 1.4π (made up of 0.2π, 0.2π, 1π from fibre stretcher, pre-amplifier and power amplifier, respectively). The corresponding spectrum is shown in Fig. 5.2.7(a). I tested another fresh fibre in an amplifier which was then seeded by a 1953nm CW laser for a period of 6 hours per time, as shown in Fig.5.2.6. In addition, no degradation was observed in the CPA experiment over the total 20 hours of experimentation, and hence there was no photodarkening effect recorded for this fibre during the test time.

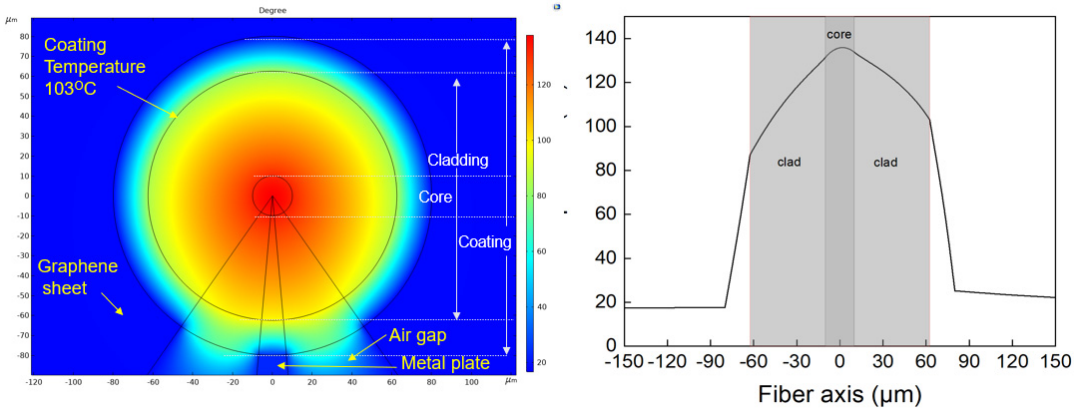

Fig. 5.2.5. 1953nm CW laser seeded power-stability test of the germanate fibre amplifier at the highest output under 50 W cladding pump power over 6 hours for every 30 seconds.

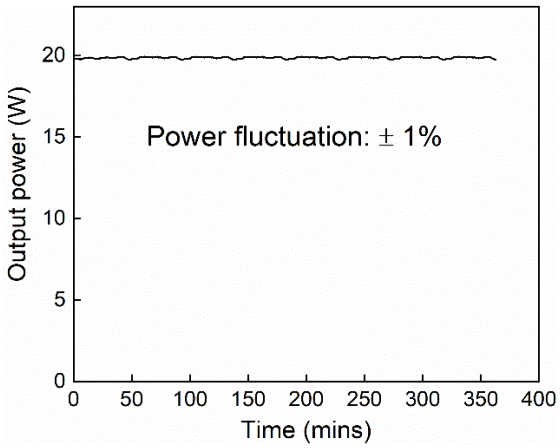

Fig. 5.2.6. 1953nm CW laser seeded power-stability test of the germanate fibre amplifier at the highest output under 50 W cladding pump power over 6 hours for every 30 seconds.

The pulses were then recompressed using a pair of fused silica transmission gratings (Ibsen Photonics A/S) with a single pass transmission efficiency of 94% when in the 1900 nm to 2100 nm range. The polarisation of the pulses incident to the gratings was controlled using bulk waveplates at the fibre output (a maximum incident PER of 16 dB was achieved). The overall double-pass compressor throughput was 14.1 W (70.5 % measured efficiency). With an appropriate grating separation, a minimum compressed pulse duration of 310 fs was achieved, as measured with a SHG autocorrelator (APE Pulse-check) (see Fig. 5.2.6(b)). The estimated time bandwidth product (TBP) of 0.98 is 2.2 times the transform-limited value for a Gaussian pulse (0.44), but close to that of a transform-limited pulse with a rectangular-spectrum (0.88). I calculated the Fourier transform of the spectrum and estimated that 75% of the energy was in the main peak, yielding an estimated peak power of 2.17 MW. The

different depth levels of the gas line shown in Fig. 5.2.7 (a), and (c) are due to the different measurement resolution of the OSA. As shown in Fig. 5.2.4 (right), the spatial mode out of the compressor was measured as having a respective M_x^2 and M_y^2 of 1.09 and 1.13, indicating close-to pure-single-mode operation and confirming that the desired fundamental mode guidance was achieved in the TDGF.

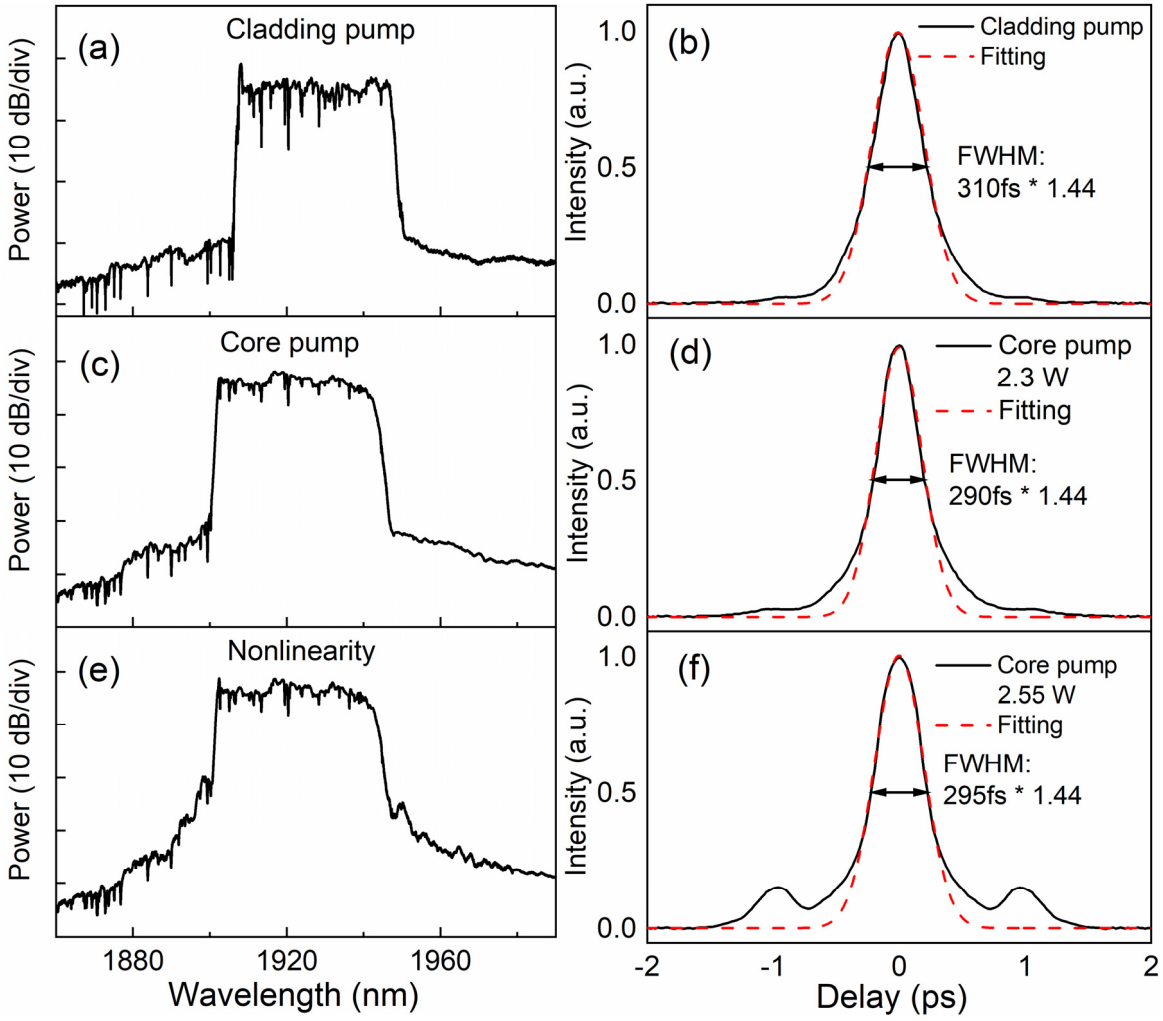

Fig. 5.2.7. Output spectra from the power amplifier and autocorrelation traces after the compressor. (a) and (c), Spectra at the maximum amplifier output power of 20W and 3.2W for cladding pumping and core pumping respectively. (b) and (d), Autocorrelation trace at the maximum output power of 14.1W and 2.3W after the compressor for cladding pumping and core pumping respectively. (e) Spectrum at a higher amplifier output power of 3.6W for core pumping. (f) Autocorrelation trace at an output power of 2.55W after the compressor for core pumping illustrating the deleterious impact of nonlinearity in the final stage amplifier.

5.2.2.2 Core pumping for 1st generation of TDGF

I next investigated core pumping a shorter length of TDGF (19 cm) in the power amplifier for pulse energy and peak power scaling. As Fig.5.2.8 shows, a fibre coupled polarisation

dependent pulse-picker (AOM) was inserted after the pre-amplifier in order to reduce the repetition rate from 15.7 MHz to 0.39 MHz. After the insertion of the pulse picker, the other polarisation maintaining pre-amplifier consisted of 30 cm of PM Tm-doped fibre with a core diameter of 10 μm (Nufern PM-TDF-10P/130-HE). It was then core pumped at 1560 nm to boost the power into the final amplifier from 0.8 mW to 40 mW.

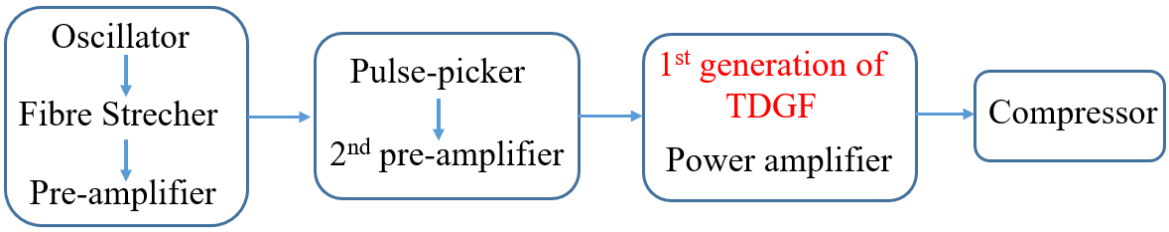

Fig.5.2.8 Schematic diagram of the CPA system based on core pumping 1st generation of TDGF in the main amplifier.

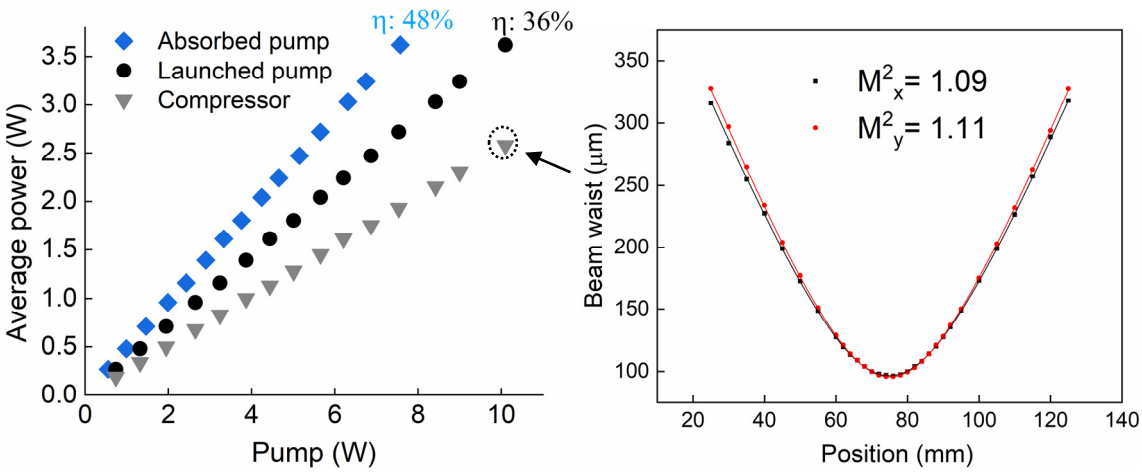

Fig. 5.2.9. (left) Measured average output power after power amplifier stage versus launched pump power and absorbed pump power. (right) Measured beam quality at maximum output power of 2.3 W (after the compressor).

The 19 cm TDGF power amplifier was core-pumped via a 1565 nm EDFL pump laser (SPI Lasers) with a maximum power of 10 W through a PM-WDM coupler (Lightcomm). The splicing loss between the TDGF and pigtail fibre of the silica fibre-based PM-WDM was similar to that in the cladding pumped case (<1.2 dB). Fig. 5.2.7 (c) shows the signal spectrum at its maximum average output power of 3.2 W for a pump power of 9 W, which is the highest output power achieved in germanate fibres when using in-band core pumping (corresponding to a slope efficiency of 36% with respect to launched pump power) (Fig. 5.2.9 (left)). Accounting for a careful cut-back measured splice loss of 1.2 dB for the launched pump, the slope efficiency power was 48% with respect to the absorbed pump (Fig.

5.2.9 (left)), which is comparable to the value I reported from a similar system that incorporated a Tm-doped silica fibre amplifier [19]. The corresponding autocorrelation trace of the compressed pulse is shown in Fig. 5.2.7 (d) and shows a pulse duration of 290 fs. The TBP of 0.94 is similar to the cladding pumped result. I calculated that 85% of the energy was in the body of the pulse, so with the recompressed average power of 2.3 W, the pulse energy was estimated to be 5 μJ and the peak power 17 MW. In addition, excellent spatial mode quality was evidenced by the M_x^2 and M_y^2 values of 1.09 and 1.11 respectively, as shown in Fig.5.2.9 (right).

The maximum pulse energy was limited in these experiments by the appearance of spectral wings induced by nonlinear effects, as shown in Fig. 5.2.7(e) (data taken at a pump power of 10 W and an amplifier output power of 3.55W). Furthermore, the corresponding compressed autocorrelation trace shown in Fig.5.2.7 (f) indicates the formation of significant satellite-pulses.

In conclusion, I have fabricated a novel, highly doped, Tm-doped germanate fibre with a hexagonal inner cladding for highly efficient cladding pumping. In-house glass melting, preform glass extrusion and fibre drawing were used to achieve a background loss of just 1 dB/m, matching our earlier result. The table 5.2.2 presented the CPA results for both core and cladding pumped version based on this fibre. Cladding pumping of a 65 cm length of TDGF produced pulses with an average power of 14.1 W and a peak power of 2.55 MW at the output of the CPA system. Core pumping a 19 cm TDGF produced pulses with an average power of 2.3 W and a peak power of 17 MW. These results represent a combination of the highest average and peak powers achieved in the fs regime from a Tm-doped germanate fibre CPA system with high beam quality (M^2 ~1.11). However, the maximum average power was actually limited by fibre damage while the maximum peak power was limited by nonlinear effects distorting the recompressed pulses. The results are already comparable with my record peak/average powers from a very similar femtosecond conventional/flexible-fibre thulium doped silica fibre CPA system [18]. In the next section, I will therefore explore the possibility of further peak-power scaling by shortening the fibre length with a newly developed LMA germanate glass fibre that has a higher Tm^{3+} doping concentration ($8.5*10^{20}$ ions/cm^3), for which the luminescence intensity reaches its maximum at 1.8 um [25].

Table 5.2.2 CPA results of the cladding and core pumped 1st generation of TDGF in the power amplifier

	Cladding pumped version	Core pumped version
Average power	14.1 W	2.3 W
Peak power	2.55 MW	17 MW
Repetition rate	15.7 MHz	0.39 MHz
Pulse energy	0.67 μJ	5 μJ
Pulse-width	310 fs	290 fs
Length of the gain fibre	0.65 m	0.19 m
Amplifier stages	2	3

5.3 CPA system based on 2nd generation of Tm^{3+} germanate doped fibre

5.3.1 2nd generation of Tm^{3+} germanate doped fibre

Based on the 1st generation TDGF results, we developed the 2nd generation TDGF with a higher doping concentration. The design and fabrication work of the updated fibre was mainly performed by my colleague Dr. Fedia as well. During this process, we did the measurement together for the optimization of the glass doping concentration. This updated higher doping fibre was used for minimise the length of the main amplifier and so decrease nonlinearity and the pulses energy/peak power scaling in the main amplifier of the CPA system.

The core glass chemical composition was changed to $58GeO_2$-13.3PbO-13ZnO-$4Nb_2O_5$-$7Na_2O$-$1.5SiO_2$-$1.5Al_2O_3$-$1.7Tm_2O_3$ and the cladding glass keep the same as 1st generation TDGF with $58GeO_2$-15PbO-13ZnO-$4Nb_2O_5$-$7Na_2O$-$1.5SiO_2$-$1.5Al_2O_3$. Fig. 5.3.1 (a) depicts the absorption spectra of these glass samples in the wavelength range from 200 to 2000 nm using a UV-VIS-NIR double beam Varian Cary 500 spectrometer. As can be seen, there is no obvious change in the position of the Tm^{3+} absorption peaks, but the absorption

peaks increase in proportion to the amount of Tm_2O_3 used in the glass preparation. The good linearity between the Tm^{3+} concentration and the peak intensities reveals the excellent solubility of the Tm ions in the developed germanate glass composition. Thanks to this high solubility we have measured pump absorptions at 1700 nm of over 1500 dB/m, which should enable amplifiers of lengths of ~10 cm or less – ideal for many short pulse applications. Fig.5.3.1 (b) shows the emission spectra from 1500 to 2050 nm of the four germanates glasses doped with different Tm^{3+} concentrations. The emission was measured at room temperature under 793 nm pump laser excitation through a multimode silica glass fibre (200 µm core diameter and 0.22 NA). As can be seen, by increasing the Tm_2O_3 content the 1.8 µm emission from the $^3F_4 \rightarrow {}^3H_6$ transition increases gradually. This phenomenon can be explained by the reduced distance between Tm^{3+} ions, which increases the cross-relaxation energy transfer probability ($^3F_4 \rightarrow {}^3H_6 \rightarrow {}^3F_4 \rightarrow {}^3F_4$) before attaining a maximum value at a Tm^{3+}concentration of 8.5×10^{20} ions/cm^3. The integral area of the emission intensity from 1600 nm to 2050 nm for Tm^{3+} concentration of 3×10^{20} ions/cm^3 and 6×10^{20} ions/cm^3 account for 60% and 78% respectively with maximum value at a Tm^{3+}concentration of 8.5×10^{20} ions/cm^3. The 1.8 µm emission intensity decreases (53% of the maximum value) with further addition of Tm_2O_3 content which may be explained by the enhanced energy transfer rate from $^3F_4$ to OH^- or impurities. It is worth to mention that OH^- is related to the glass composition and glass preparation process. The glasses were prepared in an open melting furnace. We could further reduce the OH- content if we used a controlled dry atmosphere like a glove box with added metal halides in the glass composition like chlorides and fluorides. The halides help to effectively remove water from the glass but we could not use it on the open furnace as theses chemical produce toxic gases which should only be used in a controlled dry atmosphere (glove box). The inset of Fig.5.3.1 (b) shows the lifetime of the Tm^{3+} at $^3F_4$ level in the core glass measured at room temperature using a 793 nm laser diode modulated with a 10-ms-duration square pulse. The fluorescence decay from the glass was collected using a multimode fibre connected to an oscilloscope equipped with an InGaAs photodetector (PDA10D-EC 1200 nm-2600 nm). The setup of the lifetime measurement is illustrated in Fig. 5.3.2. It was measured to be 1.5 ms with the Tm^{3+} doping concentration of 8.5×10^{20} ions/cm^3 showing a good fit with a single exponential decay function.

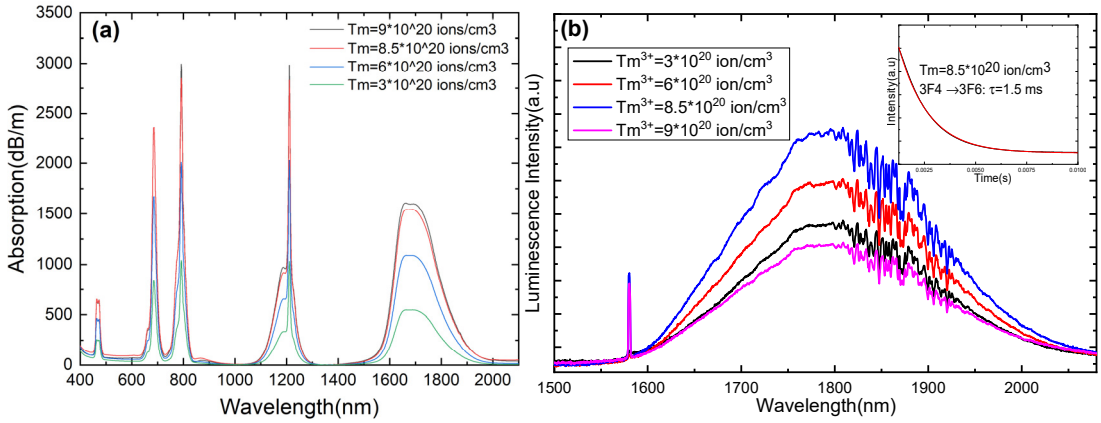

Fig. 5.3.1 (a) Absorption spectra of germanates glasses doped with different Tm^{3+} concentration. (b) Emission spectra of germanate glasses doped with different Tm^{3+} concentrations upon excitation using a 793nm LD. The inset shows the fluorescence decay curve of 1.8 μm emission from the core glass.

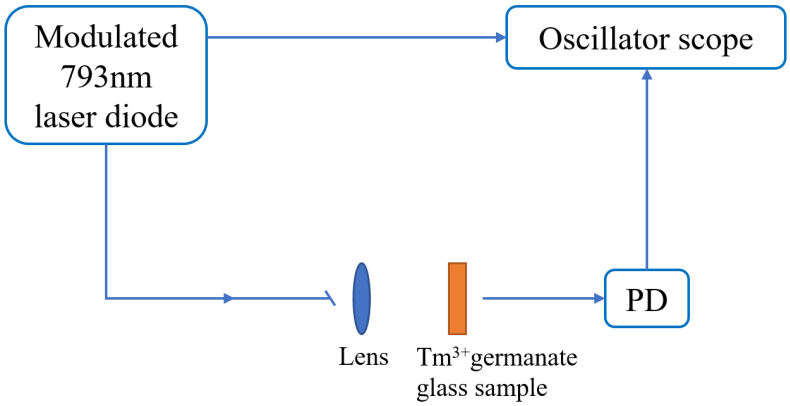

Fig. 5.3.2 Home-fabricated thulium doped germanate glass lifetime measurement setup. PD: Photodiode.

The core and cladding glasses (labelled as Ge-01 and Ge-02, respectively) were then produced and the core glass was doped with Tm^{3+} ions at the optimal concentration of 8.5×10^{20} ions/cm^3. For the fabrication of Tm^{3+} doped germanate LMA fibre, the Ge-01 glass rod (120 mm long and 11.5 mm in diameter) was first drawn into a cane of 1.3 mm diameter. The Ge-02 glass billet was then extruded into an hexagonal tube of 9.5 mm outer diameter (vs 2 opposites angles) and 1.8 mm inner diameter. Note that we have chosen a hexagonal shape for our double clad fibre to facilitate pump mode mixing as needed to achieve a high pump absorption, and to provide for lower loss splicing to other centrally symmetric (e.g. circular cross section) fibres. To extrude the cladding glass, a speed of 0.1 mm/min was used and the temperature was around 575-615°C in order to have a force of 1.1-2.5 kN. Both speed and temperatures were chosen to avoid bending. The Ge-01 glass rod and Ge-02 glass tube were then co-drawn into an optical fibre using a rod-in-tube technique. The fibre core

and cladding diameters were 17 ± 0.5 µm and 120 ± 1 µm, respectively. An outer cladding made by a UV curable low index acrylate polymer was also added to provide mechanical protection and to allow cladding pumping. The fibre loss was measured to be ~1.2 dB/m at 980 nm by a cut-back method over a length of 5.3 m. This is substantially lower than that of previously reported Tm^{3+} doped lead silicate glass (7 dB/m) [13] and germanate glass (3 dB/m) [14] fibres, and it confirms the absence of crystallization during the fibre fabrication.

Highly Tm^{3+} doped germanates glass SM fibres with a core diameter of 17 µm and a hexagonal inner cladding (diameter of 120 µm) were designed and fabricated by the rod-in-tube technique. As a result of paying careful attention to the optimisation of the glass material quality and to the control of the fibre fabrication process, a background fibre loss of ~1.2 dB/m was achieved - one of the lowest values reported to date for a germanate fibre. This loss value was also comparable with our 1st generation TDGF (1 dB/m). A Tm^{3+} doping concentration of 8.5×10^{20} ions/cm^3 was also achieved, which to the best of our knowledge, is the highest Tm^{3+} doping concentration reported to date in germanate glass fibres. Compared with the 1st generation TDGF mentioned in the last section, with a 3×10^{20} ions/cm^3 doping concentration, the shorter length usage of the amplifier through the 2nd generation TDGF means at least 2 times the pulses energy/peak power scaling.

5.3.2 Experimental results and discussion

5.3.2.1 Core pumping for 2nd generation of TDGF

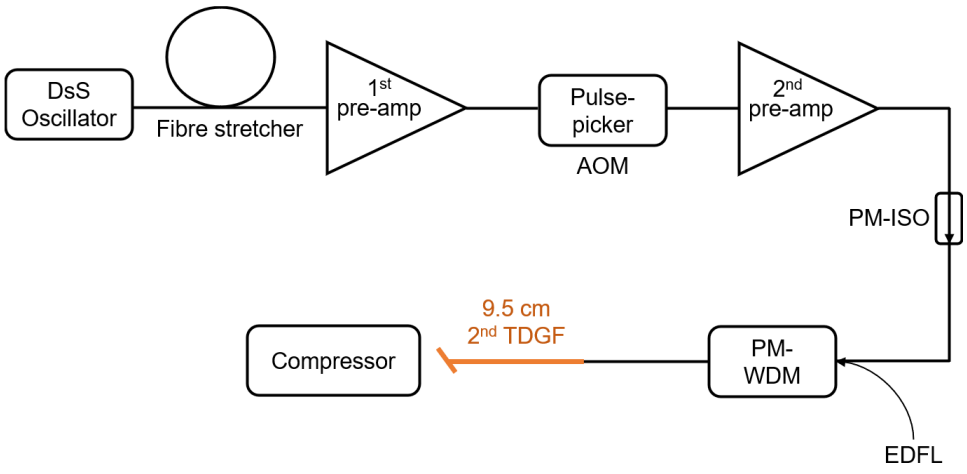

Fig.5.3.3. Schematic of the CPA system based on core pumped 2nd generation of TDGF. DsS: Dissipative soliton; AOM: acousto-optic modulator; Amp: amplifier; PM-ISO: polarization maintaining isolator; EDFL: erbium doped fibre laser; PM-WDM: polarization maintaining wavelength-division multiplexer;

I explored the CPA system through core pumping the 2nd generation TDGF in the power amplifier. Fig.5.3.3 illustrates the experimental structure of the core pump CPA system based on the 2nd generation TDGF, which was a modified version of the setup presented in Fig. 5.2.8. The only difference between the two is a 19 cm section of 1st generation TDGF was replaced by a 9.5 cm 2nd generation TDGF. Note that the core splicing loss between the 2nd generation TDGF and the pigtail fibre of the silica fibre-based PM-WDM was 0.8 dB, which is better than in the 1st generation TDGF case (1.2 dB) as it has a smaller core size mismatch loss and improved splicer parameters. The pulses of the oscillator (Fig. 5.3.4 left, black) were amplified to 160 mW in the pre-amplifier (Fig. 5.3.4 left, blue) at a pump power of 400 mW. Then, the pulses' repetition rate was decreased to 0.156 MHz (1/100) through an AOM pulse-picker with an average power of 0.5 mW. After that, the second PM core-pumped pre-amplifier (Fig. 5.3.4 left, green) increased the signal power to 50 mW for the following TDGF power amplifier.

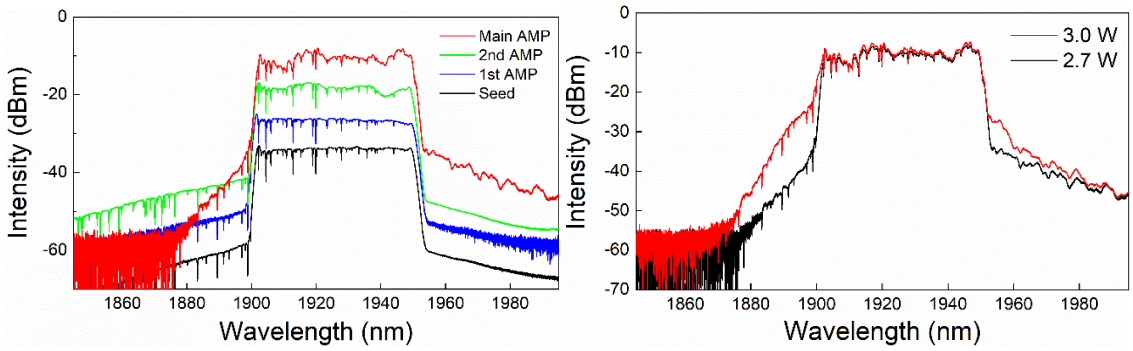

Fig.5.3.4 (left) Optical spectra after the oscillator (black), 1st pre-amplifier (blue), 2nd pre-amplifier (green) and final amplifier amplified pulses (red) at the 2.7 W output power. (right) Spectrum after main power amplifier for output power of 3 W (red) and 2.7 W (black).

Compared with the 1st generation TDGF in the power amplifier, the 2nd generation TDGF suffered from a heavy thermal issue due to having a doping concentration that was 2.8 times higher than the 1st generation TDGF and a fibre length that was 2 times shorter. During a CW source seeded test, fibre damage occurred on four separate occasions when the core pump power reached 6.5 W. This damage happened at a random point inside the fibre and close to the pump launch end. Fig. 5.3.4 (left, red) shows the spectrum in the power amplifier with an output power of 2.7 W under 5.5 W pump power. With pump power further increasing to 6.2 W, the pulse boosted to 3 W (Fig. 5.3.4 right, red) while also starting spectral sides broadening generation due to nonlinearity. Fig. 5.3.5(a) illustrates that the

slope efficiency in the power amplifier was 54% with respect to incident pump power, which is higher than the 1st generation TDGF based CPA system (36%). After compression and when at the maximum compressed output power of 1.9 W, 240 fs duration pulses were obtained (71% compressor transmission efficiency). The autocorrelation of the 12 μJ compressed pulses is shown in Fig. 5.3.5(b). The time bandwidth product (TBP) was calculated to be 0.93, which is similar to the 1st generation TDGF system (0.94). Based on the autocorrelation data, I calculate that 84% of the pulse energy resides in the main peak, implying a pulse energy of 10 μJ and a peak power of 42 MW at the centre of the pulse. The out of the compressor was measured to have a respective M_x^2 and M_y^2 of 1.12 and 1.16 (as shown in Fig. 5.3.6). These are slightly worse than those from the 1st generation TDGF system (M_x^2 :1.09; M_y^2: 1.11) but it was still a good single spatial mode operation.

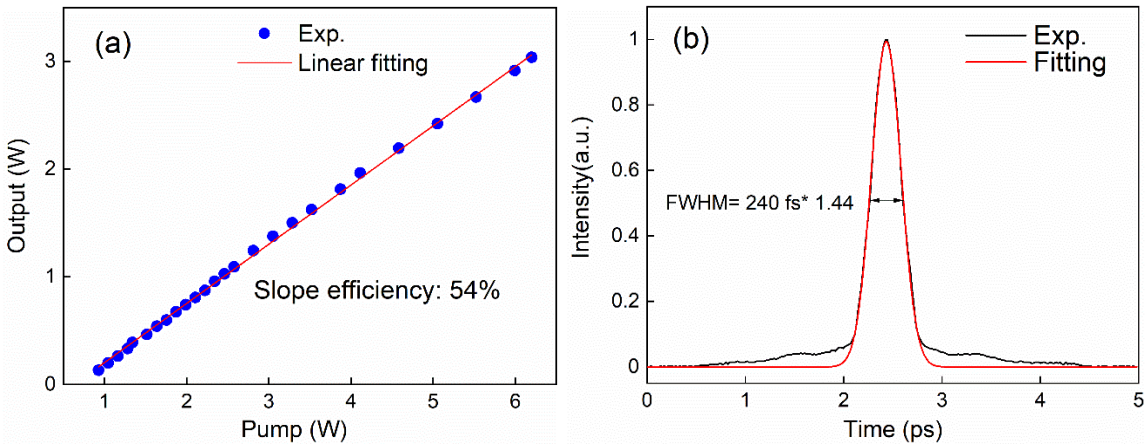

Fig.5.3.5 (a) Power (blue dot) from final amplifier vs. incident pump power. (b) Autocorrelation trace at compressed average power of 1.9 W.

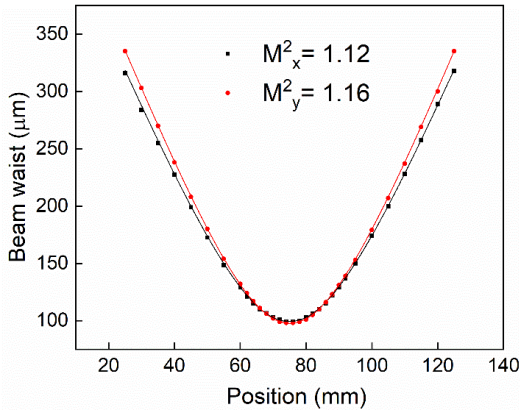

Fig.5.3.6 Measured beam quality at maximum output power of 1.9 W after the compressor.

5.3.2.2 Cladding pumping for 2nd generation of TDGF

I next investigated the cladding pumping CPA system performance for the 2nd generation TDGF. The Fig. 5.3.7 shows the schematic diagram of the system. When compared with the cladding pumping scheme of the 1st generation TDGF in Fig. 5.2.2, the only difference between the two was that the 65 cm 1st generation TDGF in the power amplifier was replaced by a 30 cm 2nd generation TDGF. Note that the core and clad splice loss between the 2nd generation TDGF and the pigtail fibre of the silica fibre-based PM-Combiner was 0.8 dB and 0.2 dB respectively, which is better than the 1st generation TDGF's case in terms of core splice loss. The reason for this was mentioned previously in the core pumping schematic.

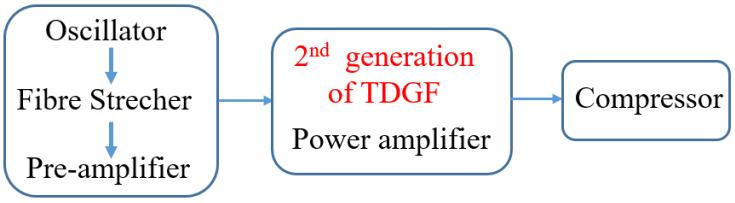

Fig.5.3.7 Schematic diagram of the CPA system based on cladding pumping 2nd generation of TDGF of the power amplifier.

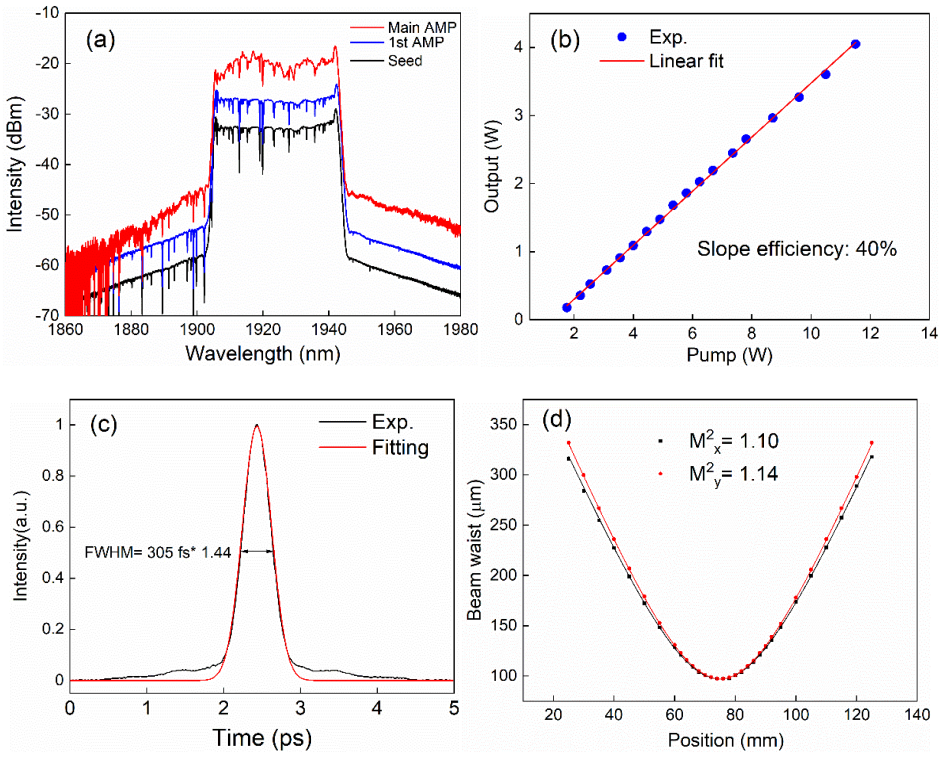

Fig.5.3.8 (a) Optical spectra after the oscillator (black), pre-amplifier (blue) and power amplifier amplified pulses (red) at the maximum output power of 4W. (b) Power (blue dot) from final amplifier vs. incident clad pump power. (c) Autocorrelation trace at maximum compressed average power of 2.8 W. (d) Measured beam quality at maximum output power of 2.8 W after the compressor.

Fig. 5.3.8 (a) shows the spectral output from the oscillator, pre-amplifier and main amplifier. An output power of 4 W (shown in Fig. 5.3.8 (b)) was achieved at a maximum pump power of 11.5 W. This maximum pump power was set in order to protect the fibre from the thermal damage that occurred when the pump power surpassed 12 W, at a slope efficiency of 40% with respect to the incident pump power. This was somewhat higher than the 36% achieved with the 1st generation TDGF version. The total B-integral of the system was calculated to have reduced to 0.5π (0.1π from the power amplifier) due to the low pulse energy and short length of fibre. Around 86% of the energy remained in the main peak. The 2.8 W compressor output resulted in a corresponding pulse energy of 0.18 μJ and a peak power of 0.59 MW in the main peak, with a pulse duration of 305 fs, as shown in Fig. 5.3.8 (c). The TBP of 0.91 is similar to the core pumped result (0.94). The measured compressed output had a beam quality of M^2= 1.12 (M_x^2: 1.10; M_y^2: 1.14), as shown in Fig. 5.3.8(d), which indicates that the system achieved close to a pure-single-mode.

In conclusion, we have developed a higher doped ($8.5*10^{20}$ ions/cm^3), 2nd generation of Tm-doped germanate fibre for power scaling. At the output of the CPA system, results were shown in the table 5.3.1 for both of the core pumped and cladding pumped version. Core pumping of a 9.5 cm length of TDGF produced pulses with a launched slope efficiency of 54%, an average power of 1.9 W and a peak power of 42 MW. These results represent the highest peak powers achieved in the fs regime from a conventional Tm-doped germanate fibre CPA system with good beam quality (M^2 ~1.14). The maximum peak power was limited by nonlinear effects spectrum broadening. Cladding pumping a 30 cm TDGF meanwhile, produced pulses with an average power of 2.8 W and a peak power of 0.59 MW at a launched power slope efficiency of 40%. Compared with the 1st generation of TDGF, both the core pump and cladding pump schemes had a higher amplification efficiency. The 2nd generation TDGF can provide over 2 times the peak power when in the core pump version due to having a shorter power amplifier. However, the higher doping and shorter length result in a reduction in the fibre thermal damage that was inflicted on the threshold pump power in the core (6.5 W) and cladding (12 W). There was considerably less damage than in the 1st generation TDGF, which induced an average power scaling limitation. The results are comparable with the average powers and beat the peak power that was produced from the very similar femtosecond conventional/flexible-fibre thulium doped silica fibre CPA system mentioned in chapter 4. This therefore confirms that the highly Tm^{3+} doped germanate glass

single mode fibre can be used as an alternative to the silica-based fibre for the generation of 2 μm high energy/peak power pulses.

Table 5.3.1 CPA results of the cladding and core pumped 2nd generation of TDGF in the power amplifier

	Cladding pumped version	Core pumped version
Average power	2.8 W	1.9 W
Peak power	2.55 MW	17 MW
Repetition rate	15.7 MHz	0.39 MHz
Pulse energy	0.67 μJ	5 μJ
Pulse-width	310 fs	290 fs
Length of the gain fibre	0.65 m	0.19 m
Amplifier stages	2	3

5.4 Summary

In conclusion, I have demonstrated a high-peak-power, high energy germanate thulium-doped fibre CPA system using both 1st generation fibre (3×10^{20} ions/cm^3 doping) and 2nd generation fibre (8.5×10^{20} ions/cm^3 doping). Both methods were investigated for the core and cladding pumping schemes.

First, for the 1st generation of TDGF, cladding pumping of a 65 cm length of TDGF was found to produce pulses with an average power of 14.1 W and a peak power of 2.55 MW at the output of the CPA system. Core pumping a 19 cm TDGF meanwhile, produced pulses with an average power of 2.3 W and a peak power of 17 MW. Then, with the development of the 2nd generation higher doping TDGF, core pumping of a 9.5 cm length of TDGF produced pulses with an average power of 1.9 W and a peak power of 42 MW at the output of the CPA system. Pulses with a 2.8 W average power and 0.59 MW peak power were

obtained. The 2nd generation TDGF with higher doping was able to produce pulses that had a higher peak power but less average power.

Our 1st generation TDGF had comparable results, in terms of peak/average power, to the silica fibre-based CPA system mentioned in chapter 4. Our 2nd generation TDGF meanwhile, can produce a higher peak power (42 MW vs. 25 MW). This confirms that the highly Tm^{3+} doped germanate glass single mode fibre can be used as an alternative to silica-based fibre for the generation of 2 μm high energy/peak power pulses. Given the rapid ongoing progress in our fibre development processes, this fibre technology should ultimately be capable of achieving higher peak powers and similar, or possibly even higher, average powers in the future. Thus, the next steps for our research are to optimise the fibre fabrication and temperature management so as to enable power scaling. In the next chapter, I will summarise the thesis and share the future prospects.

Reference

[1] R. G. Frehlich, S. M. Hannon, and S. W. Henderson, “Performance of a 2-μm coherent Doppler lidar for wind measurements,” J. Atmos. Ocean. Technol. **11**(6), 1517–1528 (1994).

[2] W. Shi, E. Petersen, N. Moor, A. Chavez-Pirson, and N. Peyghambarian "All fiber-based single-frequency Q-switched laser pulses at 2 μm for lidar and remote sensing applications," Proc. SPIE 8164, 81640M (2011).

[3] V. Konov, “Laser in micro and nanoprocessing of diamond materials,” Laser & Photon. Rev. **6**(6), 739-766 (2012).

[4] Q. Fu, L. Xu, S. Liang, D. P. Shepherd, D. J. Richardson and S. Alam, "Widely Tunable, Narrow-Linewidth, High-Peak-Power, Picosecond Midinfrared Optical Parametric Amplifier," IEEE J. Quantum Electron. **24**(5), 1-6 (2018).

[5] M. P. Arpin, T. Popmintchev, M. Gerrity, B. Zhang, M. Seaberg, D. Popmintchev, M. M. Murnane, and H. C. Kapteyn, “Bright, coherent, ultrafast soft X-ray harmonics spanning the water window from a tabletop light source,” Phys. Rev. Lett. **105**(17), 173901 (2010).

[6] E. A. Peralta, K. Soong, R. J. England, E. R. Colby, Z. Wu, B. Montazeri, C. McGuinness, J. McNeur, K. J. Leedle, D. Walz, E. B. Sozer, B. Cowan, B. Schwartz, G. Travish, and R. L. Byer, “Demonstration of electron acceleration in a laser-driven dielectric microstructure,” Nature **503**(7474), 91–94 (2013).

[7] A. Klenke, S. Breitkopf, M. Kienel, T. Gottschall, T. Eidam, S. Hädrich, J. Rothhardt, J. Limpert, and A. Tünnermann, “530 W, 1.3 mJ, four-channel coherently combined femtosecond fiber chirped-pulse amplification system,” Opt. Lett. **38**(13), 2283–2285 (2013).

[8] C. Gaida, M. Gebhardt, T. Heuermann, F. Stutzki, C. Jauregui, and J. Limpert, "Ultrafast thulium fiber laser system emitting more than 1 kW of average power", Opt. Lett. **43**(23), 5853-5856 (2018).

[9] C. Gaida, M. Gebhardt, F. Stutzki, C. Jauregui, J. Limpert, and A. Tünnermann, “Thulium-doped fiber chirped-pulse amplification system with 2 GW of peak power,” Opt. Lett. **41**(17), 4130–4133 (2016).

[10] F. Haxsen, D. Wandt, U. Morgner, J. Neumann, and D. Kracht, "Pulse energy of 151 nJ from ultrafast thulium-doped chirped-pulse fiber amplifier," Opt. Lett. **35**(17), 2991-2993 (2010)

[11] R. A. Sims, P. Kadwani, A. L. Shah and M. Richardson, "1 μJ, sub-500 fs chirped pulse amplification in a Tm-doped fiber system," Opt. Lett. **38**(2), 121-123 (2013).

[12] H. Hoogland and R. Holzwarth, "Compact polarization-maintaining 2.05-μm fiber laser at 1-MHz and 1-MW peak power," Opt. Lett. **40**(15), 3520-3523 (2015).

[13] F. Auzel and P. Goldner, “Towards rare-earth clustering control in doped glasses,” Opt. Mater. **16**(1-2), 93–103 (2001).

[14] R. Tumminelli, V. Petit, A. Carter, A. Hemming, N. Simakov, and J. Hob, “Highly doped and highly eÿcient Tm doped fiber laser,” Proc. SPIE 10512, 105120M (2018).

[15] J.Wu, Z.Yao, J.Zong and S.Jiang,“Highly efficient high-power thulium-doped germanate glass fiber laser,” Opt. Lett. **32**(6), 638-640 (2007).

[16] S.D. Jackson,” Cross relaxation and energy transfer upconversion processes relevant to the functioning of 2 μm Tm3+-doped silica fibre lasers”, Opt. Commum. **230**(1-3),197-203 (2004).

[17] X. Wen, G. Tang, Q. Yang, X. Chen, Q. Qian, Q. Zhang, and Z. Yang, “Highly Tm3+ doped germanate glass and its single mode fiber for 2.0 μm laser,” Sci. Rep. **6**(1), 20344 (2016).

[18] Qiang Fang, Wei Shi, Khanh Kieu, Eliot Petersen, Arturo Chavez-Pirson, and Nasser Peyghambarian, "High power and high energy monolithic single frequency 2 μm nanosecond pulsed fiber laser by using large core Tm-doped germanate fibers: experiment and modeling," Opt. Express **20**(15), 16410-16420 (2012)..

[19] Z. Ren, F. B. Slimen, J. Lousteau, N. White, Y. Jung, Xu, J. H. V. Price, D. J. Richardson and F. Poletti, “Compact chirped- pulse amplification systems based on highly Tm3+ doped germanate fiber” Opt. Letters, **46**(13), 3013-3016 (2021)..

[20] F. B. Slimen, S. Chen, J. Lousteau, Y. Jung, N. White, S. Alam, D. J. Richardson, and F. Poletti, "Highly efficient -Tm3+ doped germanate large mode area single mode fiber laser," Opt. Mater. Express **9**(10), 4115-4125 (2019).

[21] A. Wada, S. Okude, T. Sakai, and R. Yamauchi, "GeO2 concentration dependence of nonlinear refractive index coefficients of silica-based optical fibers," Electron. Commun. Jpn. Part Commun. **79**(11), 12–19 (1996).]

[22] J. Daniel, N. Simakov, A. Hemming, W. Clarkson, and J. Haub, "Metal clad active fibres for power scaling and thermal management at kW power levels," Opt. Express **24**(16), 18592-18606 (2016).

Chapter 6

2 µm Mamyshev oscillator

6.1 Introduction

Recently, the Mamyshev oscillator (MO) has gained lots of attention thanks to the generation of mode-locked pulses with a broad bandwidth (>100 nm), high pulse energy (µJ level) and an ultra-short duration (tens of a femtosecond). The combination of the pulses' spectral broadening due to the self-phase modulation (SPM) in the fibres and the following offset spectra band pass filters in two arms, play the role of artificial saturable absorber with a tunable modulation depth and high damage threshold.

Liu *et al.* theoretically and experimentally investigated (in 2017) the pulse propagation in a Mamyshev oscillator [1]. Limited by pump power, they experimentally demonstrated pulses with an energy of 50 nJ and a duration of 40 fs through Yb-doped fibre with a core size of 6 µm. Then, in 2018 their group developed a self-seeded and easy-starting Mamyshev oscillator by simply flipping a mirror to engage a starting arm [2], which generated 35-fs and 190-nJ pulses, for 3 MW peak power pulses. After that, in 2019 Wu *et al.* utilised Yb-doped LMA-PCF fibres (29 µm core) to produce energy pulses of 1.1 µJ with 41 fs and a peak power of 13 MW [3], which are the highest single-pulse energy and peak power values obtained by a single-stage, mode-locked fibre oscillator. In March 2020, with few commercially available components at 1 µm, Etienne *et al.* created an all-fibre MO structure [4]. Soon afterward, Vincent *et al*. presented an all-fibre MO at 1550 nm which was based on chirped fibre Bragg gratings with a Gaussian reflectivity profile [5].

Currently, most MO related research focuses on the 1µm and 1.5 µm wavelength range. Conventional silica base thulium doped fibre has a relatively large anomalous dispersion at 2 µm with the value of -0.03 ps^2/m, thus would suffer from modulation instability rather than

self-phase-modulation, which limits the output energy scaling and spectral bandwidth broadening [6]. There is a limited number of references about MO at 2 μm due to the lack of gain fibres with normal dispersion, which are necessary for the formation of linearly chirped parabolic pulses. There was only one group that had experimentally demonstrated MO through TDF with anomalous dispersion in 2020 [7]. They demonstrated a MO through the combination of the TDF with anomalous dispersion and subsequent normal dispersion fibre (NDF), producing pulses with an energy of 3.55 nJ and a spectral bandwidth of 48 nm. These results were much lower than MOs achieved in 1μm and 1.5 μm waveband. Further power scaling was limited by modulation instability due to the TDF with anomalous dispersion.

Owing to our germanate thulium doped fibre, which had an estimated normal dispersion around the 2μm wavelength range, I intended to investigate the Mamyshev oscillator based on our in-house 1st generation of TDGF, mentioned in Chapter 5.2.1. I firstly created a modelling of the MO based on the "RP FIBER POWER" software to explore the guidance of the cavity design and theoretical maximal output pulse characteristics, e.g., pulse energy, bandwidth, peak power, pulse-width etc. Then, an experimental setup of the MO was built and preliminarily results were investigated with a single output pulse that had a 107 nm bandwidth and 147 nJ.

6.2 Simulation

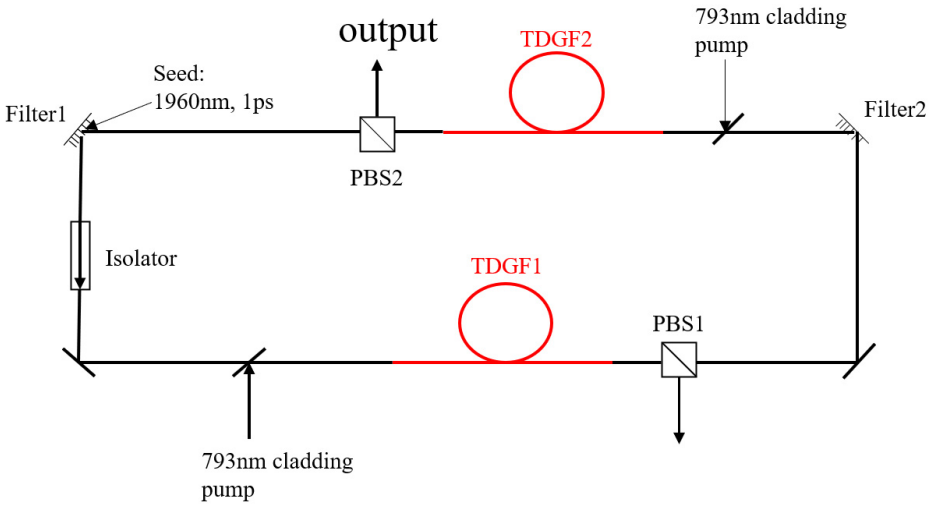

Fig.6.2.1 Schematic of the simulated ring Mamyshev oscillator. PBS: polarizing beam splitter.

The simulated configuration of the oscillator is schematically illustrated in Fig.6.2.1 using the accurate fibre parameters shown in Table 6.2.1. The simulation includes the Kerr nonlinearity, stimulated Raman scattering and second order dispersion. Polarisation is not considered in the simulation. The oscillator was seeded using initial pulses with 1 ps at 1960 nm.

Table. 6.2.1. Components' parameters used in simulated Mamyshev oscillator.

Components	Length (m)	BW (nm)	WL (nm)	OC (ratio)	GVD (ps^2/m)	MFD (μm)	Loss (ratio)
Filter1		3	1955				30%
TDGF1	1.2			2.3	0.005	20	
PBS1				20%			
Filter2		3	1965				30%
TDGF2	1.2	5.7	0.67	5	0.005	20	
PBS2				90%			
Optical length	30						

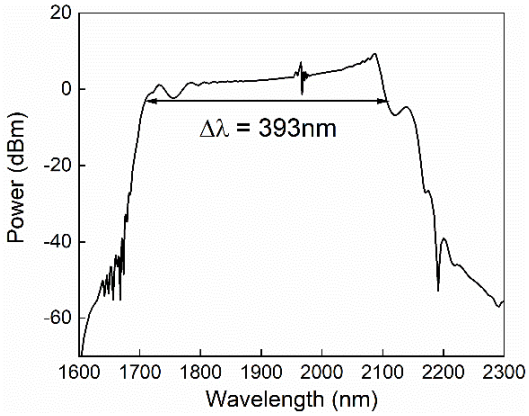

Fig. 6.2.2 Simulated spectrum of the MO.

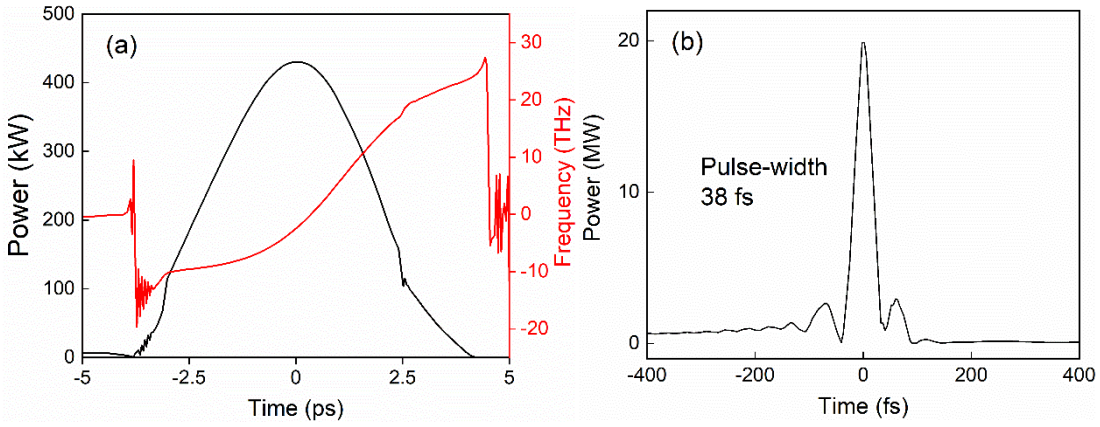

Fig. 6.2.3 (a) Simulated output pulses from MO in time domain (black) and its frequency. (b) Simulated compressed pulse shape of MO.

The model predicted that the MO can generate pulses with maximum bandwidth of up to 393 nm, as shown in Fig. 6.2.2. The corresponding pulse shape in the time domain from the oscillator and compressor are illustrated in Fig. 6.2.3(a) and (b) respectively. The pulses had a parabolic shape with a near linear chirp and can be compressed to a 38 fs pulse-width. The maximal pulse energy was 1.8 μJ with a peak power of 20 MW, which is limited by deviations in the pulse from a parabolic shape would then caused wave breaking.

6.3 Preliminarily experimental results and discussion

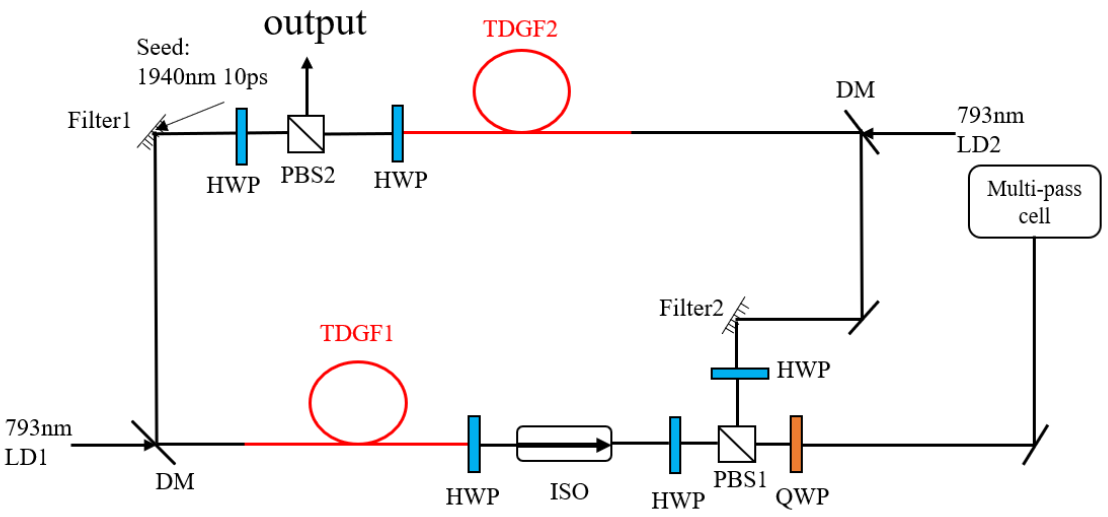

Fig.6.3.1. Schematic diagram of experimental ring MO cavity. LD: laser diode; ISO: isolator; TDGF: thulium doped germanate fibre; HWP: half wave-plate; QWP: quarter wave-plate; DM: dichroic mirror; PBS: polarization beam spliter.

The setup of the experimental Mamyshev oscillator was illustrated in Fig.6.3.1, including two amplification arms with the 1st generation of thulium doped germinated fibre that was presented in Chapter 5.2. It is worth to mention that the whole experimental setup used free space optics rather than full fiberized optical elements, this was because commercially available fibre base components (e.g. fibre combiner, fibre isolator, fibre coupler) which have large anomalous dispersion at 2 μm (-0.1 ps^2/m) and would generate modulation instability rather than self-phase-modulation during energy scaling process, thus to limit output energy and broad bandwidth. Both the TDGFs with a length of 1 m and 20 μm core size in two arms were cladding pumped via 793 nm LDs (BWT), which provided a maximum 30 W pump power for each arm. The fibre had 20 dB clad absorption at 793 nm and normal

dispersion after 1.738 μm. All fibre ends were 8° angle polished (without endcaps) to reduce the parasitic oscillation. Waveplates were used to adjust the coupling efficiency for the related components. In addition, following the isolator, which provided a uni-direction operation, a multi-pass cell was inserted to elongate the cavity and reduce the repetition rate in order to overcome the pump power limitation and the TDGF's potential thermal issue for pulse energy scaling. Both bandpass gaussian filters had around a 2.5 nm spectral bandwidth which were reflective diffraction gratings with grooves of 600 lines/mm (Thorlabs GR25-0616). Filter1 and Filter2 were set to 1936 nm and 1943 nm respectively, with a separation of 7 nm so as to easily initiate mode-locking.

In order to start mode-locking, external seed pulses were required. The seed laser was a commercial mode-locked fibre laser (AdValue Photonics) with a 7 nm spectral bandwidth at a central wavelength of 1943 nm and energy pulses of 0.3 nJ. The pulse power can be weak as long as the bandwidth of the seed covers the central wavelength of Filter2 so as to circulate the whole first round-trip. With a fixed coupling ratio of PBS2 and adequate pump power, the multi-pulses mode-locking can be easily started. Then by gradually increasing the output coupling ratio of the PBS2 and decreasing the pump power, the oscillator can work at a single pulse operation. Once the single pulse operation is realised, the pulse output power can be enhanced through an increasement of the LD2 pump's power and PBS2 output coupling.

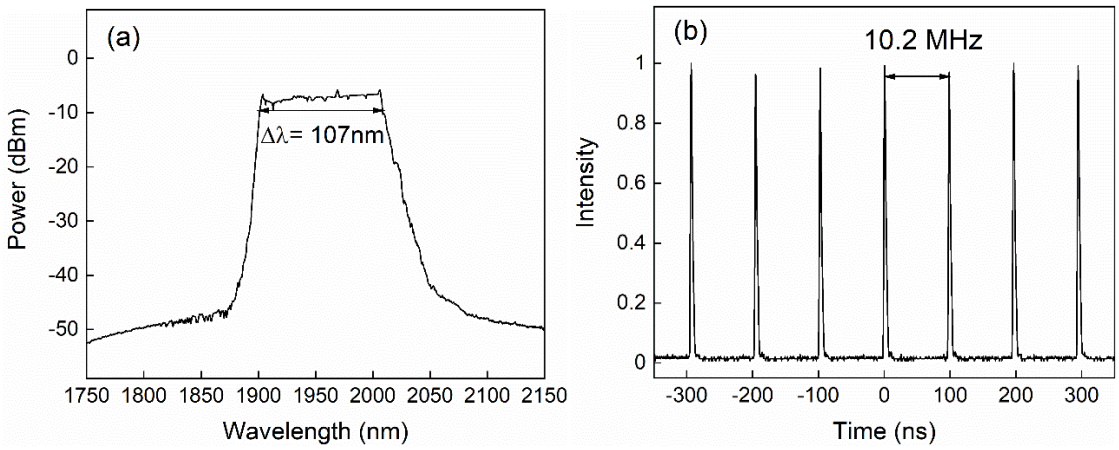

Fig. 6.3.2 (a) Measured spectrum from MO at maximal output power of 1.5 W. (b) Measured oscilloscope trace from MO at maximal output power of 1.5 W.

Fig. 6.3.2 (a) and (b) present the respective spectrum and oscilloscope trace characteristics of the pulses at a maximal output power of 1.5 W under the pump power of 10 W for both of two pump LDs. The pulses had a broad bandwidth of 107 nm, which indicates that the

Fourier transform's pulse-width was 52 femtoseconds, if we assume the Gaussian profile. The measured repetition rate of 10.2 MHz was well matched with the calculations based on the cavity length, supporting thus that the oscillator operated with a single pulse per round trip, which corresponded to a pulse energy of 147 nJ. As the table 6.3.1 shows, this result was 40 times larger than the previous best 2 μm Mamyshev oscillator, which was limited by modulation instability from the anomalous dispersion of TDF [9]. Our germanate TDF with normal dispersion had the intrinsic advantage of avoiding the modulation instability to generate much higher theoretically output pulse energy and broad spectral bandwidth through self-phase-modulation.

Table 6.3.1 MO output results comparison

	Latest research [9]	**My result**	**My simulation**
Pulse energy	3.55 nJ	147 nJ	1.8 μJ
Spectral bandwidth	48 nm	107 nm	393 nm
Limitation	Modulation instability	Available optics shortage	

Although my results had much higher pulse energy than literature, there was room for energy scaling through the simulation results (1.8 μJ). As I further increased pump power for energy scaling, the fibre closed to the output end was damaged and the MO mode-locking disappeared, which was then followed by the starting of CW lasing. There were two main reason for this:

i) The fibre ends without endcap can suffer from higher Fresnel reflection issues compared with silica fibre due to their relatively higher refractive index (~1.7).
ii) Components close to the fibre output ends were not 2 μm AR-coated (e.g., all collimation lens, and two PBSs), thus had relatively highly reflection.

6.4 Summary

In conclusion, I have explored Mamyshev oscillator at 2μm through home-fabricated germanate thulium doped fibre both through simulations and a preliminary experiment. The

simulation showed a maximum output pulse energy of 1.8μJ with spectral bandwidth of 393 nm. For the experimental part, I demonstrated a high pulse energy of 147 nJ and broad spectral bandwidth of 107 nm, which is 40 times larger than the latest research in terms of pulse energy. The further energy scaling was limited by high Fresnel reflection at fibre and optics.

Future plan will focus on solving the above two issues by adding endcaps for all fibre ends and replacing components with AR-coated ones in order to stabilise output pulses and systematically characterise pulses in terms of optical spectrum, oscillation trace, radio frequency spectrum, compression autocorrelation trace, etc. Following this, I will increase the separation of the two bandpass filters (10 nm – 20 nm) to obtain a higher pulse-energy/peak power from the 2μm MO.

References

[1] Z. Liu, Z. M. Ziegler, L. G. Wright, and F. W. Wise, "Megawatt peak power from a Mamyshev oscillator," Optica **4**(6), 649-654 (2017)

[2] P. Sidorenko, W. Fu, L. G. Wright, M.Olivier, and F. W. Wise, "Self-seeded, multi-megawatt, Mamyshev oscillator," Opt. Lett. **43**(11), 2672-2675 (2018).

[3] W. Liu, R. Liao, J. Zhao, J. Cui, Y. Song, C. Wang, and M. Hu, "Femtosecond Mamyshev oscillator with 10-MW-level peak power," Optica **6**(2), 194-197 (2019).

[4] E. Poeydebat, F. Scol, O. Vanvincq, G. Bouwmans, and E. Hugonnot, "All-fiber Mamyshev oscillator with high average power and harmonic mode-locking," Opt. Lett. **45**(6), 1395-1398 (2020).

[5] V. Boulanger, M. Olivier, F. Trépanier, M. Bernier, and M. Piché, "Efficient all-PM-fiber Mamyshev oscillator based on fiber Bragg gratings," in Laser Congress 2020 (ASSL, LAC),

[6] P. Wang, S. Yao, P. Grelu, X. Xiao, and C. Yang, "Pattern formation in 2-μm Tm Mamyshev oscillators associated with the dissipative Faraday instability," Photon. Res. **7**(11), 1287-1295 (2019).

[7] P. Repgen, B. Schuhbauer, M. Hinkelmann, D. Wandt, A. Wienke, U. Morgner, J. Neumann, and D. Kracht, "Mode-locked pulses from a Thulium-doped fiber Mamyshev oscillator," Opt. Express **28**(9), 13837-13844 (2020).

Chapter 7

Conclusion

7.1 Introduction

This thesis concerned the study and development of the thulium-doped mode-locked fibre laser based on various types of mode-locking mechanisms as a seed source for the CPA system. The compact CPA systems based on silica and germanate thulium doped fibre, which were seeded by the above mentioned mode-locked oscillators, were fully investigated for both core and cladding pumping schemes. In this chapter, I will summarise the main results and conclusions of this thesis (section 7.2) and then share the future prospects for the work (section 7.3).

7.2 Summary of results

The experimental work in this thesis includes the systematic investigation of the thulium-doped mode-locked fibre laser based on three mode-locked (ML) mechanisms – carbon nanotube (CNT), nonlinear polarisation rotation (NPR), and the semiconductor saturable absorber mirror (SESAM). Each of these offer different output pulse characteristics. The ML oscillator based on CNT (Chapter 3.2) had self-started, stable, chirped pulses that operated at around 1960 nm, as well as having a related large bandwidth (18 nm). These were suitable for the seeded CPA system but deteriorated over time. I then chose pure NPR which consists of two polarisation controllers and a PM-isolator for mode-locking generation (Chapter 3.3). This could only produce conventional soliton pulses with strong Kelly sidebands which were not suitable for my CPA system. After that, a commercial SESAM (1) was used to replace the NPR version for ML generation (Chapter 3.4). However, this SESAM (1) had an output from the oscillator of noise-like pulses with a nanosecond pulse-width. These could not be compressed and so this SESAM could not work as a seed source for the CPA system. Finally, with a new SESAM (2) placed inside the cavity and cavity's parameters (Chapter 3.5), the

desired seed pulses for the CPA system were obtained. The self-started, pre-chirped pulses from this SESAM, with an energy of 2.5 nJ at a central wavelength of 1925 nm and a 3-dB bandwidth of 40 nm, can be compressed through a grating pair to 280 fs.

Chapter 4 and Chapter 5 systematically investigate the compact CPA system based on silica and germanate fibre through both core and cladding pump schemes. The key output pulse characteristics of the CPA systems are summarised in Table 7.2.1. Benefitting from the mode-locked source with the broad bandwidth developed in Chapter 3, these six types of CPA systems can generate around 300 fs (shortest 240 fs) ultra-fast pulses with high peak power. These will be very useful for body tissue surgery, material processing, and supercontinuum generation. In addition, the pulses with a high repletion rate generated by the cladding pump scheme would be beneficial for high harmonic generation and laser-driven electrons acceleration.

Table. 7.2.1. A summary of key experimental results for various of CPA systems.

	Silica fibre		**1st germanate fibre**		**2nd germanate fibre**	
Pumping	Cladding	Core	Cladding	Core	Cladding	Core
Average power (W)	21.5	2.8	14.1	2.3	2.8	1.9
Peak power (MW)	4.2	20	2.17	17	0.59	42
Repetition rate (MHz)	15.7	0.39	15.7	0.39	15.7	0.157
Pulse Energy (μJ)	1.25	5.7	0.67	5	0.18	12
Pulse duration (fs)	297	285	310	290	305	240
TBP	0.96	0.99	0.98	0.94	0.91	0.93
Amplifier stages	2	3	2	3	2	3
Length of the main amplifier (cm)	150	29	65	19	30	9.5

Chapter 6 preliminarily explored the Mamyshev oscillator based on 1st generation of home-fabricated germanate thulium doped fibre. Own to the normal dispersion of fibre, the MO can generate output pulse energy of 157 nJ and bandwidth of 107 nm. The output pulse energy is 40 times higher than the latest research. However, , the further energy scaling was

limited by optics shortage due to the lack of optical elements at 2 μm in terms of coating and endcap glass with match refractive index.

7.2 Future work

7.2.1 Nonlinear compression pulses

In order to obtain 2 μm pulses with higher peak power which would be attractive in a number of fields, including attosecond science, strong field physics, time-resolved spectroscopy, and nonlinear optics [1–4], one effective way is to achieve shorter pulse duration, while my compact CPA system with spectral bandwidth of ~40 nm had a transform-limited pulse of ~300 fs which limits the peak power. The Mamyshev oscillator in chapter 6 had a potentially simulated compressed pulse-width of 38 fs owning to 397nm spectral bandwidth. External nonlinear pulse compression allows for the combination of the high pulse energy of CPA system (chapter 4 &5) with few cycle pulse duration generation. The nonlinear compression relies on seeded pulses with nonlinear spectral broadening via self-phase modulation by the Kerr effect and subsequent linear chirp removal to form shorter transform-limited pulses.

Nonlinear pulse compression within silica fibres [5,6] can easily generate sub-20 fs pulse durations while the peak power is limited to a few MW, corresponding to pulse energy of μJ because the onset of catastrophic self-focusing. C. Gaida et al. reported that self-compression of pulses in a silica fibre attained pulses of 38 fs duration with average power of 24.6 W around 2 μm [7]. Higher pulse energies can be handled using noble gases as the nonlinear medium, because of the much higher (three orders of magnitude) self-focusing threshold [8]. M. Gehbhardt et al. have demonstrated a nonlinear pulse compression system with a pulse peak power of 4 GW with a sub-50 fs pulse duration (seven optical cylcles) and 15.4 W average power at 2 μm wavelength, which was enabled by a high-repetition rate PCF based CPA system and a gas-based hollow core fibre (HCF) [9]. Then have also reported the generation of ultra-short pulses of 13 fs duration and 1.4 GW peak power around 2 μm from a thulium-doped fibre laser by using a gas filled anti-resonant hollow core fibre [10].

However, the mentioned above nonlinear pulse compression system with few-cycle duration used table-top, large-scale free space CPA system as the seed pulses. There is still a lot of room for investigation of the few-cycle pulse generation through nonlinear compression based on my compact and practical CPA system.

7.2.2 Mid-infrared supercontinuum generation

Broadband mid-infrared supercontinuum (MIR-SC) sources get a lot of attention due to attractive applications including spectroscopy, environmental sensing, standoff detection, and imaging [11]. Although MIR-SC generation is possible under the pump of nanosecond and picosecond pulsed sources at 2μm [11-14], these SC systems inherently lack the shot-to-shot coherence. A number of systems have been demonstrated for SC generation in the MIR using femtosecond pump lasers [15–18], which could in principle provide the shot-to-shot coherence. However, most of the existing demonstrations rely on femtosecond pump sources with many free space optics that are relatively large and usually operated at low repetition rates (~kHz level). In particular, the low repetition rate makes these sources unsuitable for frequency comb spectroscopy in the molecular fingerprint region, as the comb spacing is given by the pump repetition rate. Therefore, there is a need for developing MIR-SC sources that are pumped using high repetition rate (tens of MHz), femtosecond fiber lasers with lower size, complexity, and cost, allowing it to be field-deployable for environmental sensing applications. In short, my compact and practical CPA system with 15MHz high repetition rate has great potential in the coherent supercontinuum generation.

References

[1] T. Brabec and F. Krausz, “Intense few-cycle laser fields: Frontiers of nonlinear optics,” Rev. Mod. Phys. **72**(2), 545–591 (2000).

[2] E. Goulielmakis, M. Schultze, M. Hofstetter, V. S. Yakovlev, J. Gagnon, M. Uiberacker, A. L. Aquila, E. M. Gullikson, D. T. Attwood, R. Kienberger, F. Krausz, and U. Kleineberg, “Single-Cycle Nonlinear Optics,” Science **320**(5883), 1614–1617 (2008).

[3] L. He, Q. Zhang, P. Lan, W. Cao, X. Zhu, C. Zhai, F. Wang, W. Shi, M. Li, X.-B. Bian, and P. Lu, “Monitoring ultrafast vibrational dynamics of isotopic molecules with frequency modulation of high-order harmonics,” Nat. Commun. **9**(1), 1108 (2018).

[4] H. Xie, M. Li, S. Luo, Y. Li, J. Tan, Y. Zhou, W. Cao, and P. Lu, "Photoelectron holography and forward scattering in atomic ionization by elliptically polarized laser pulses," Opt. Lett. **43**(14), 3220-3223 (2018).

[5] M. Hornung, R. Bödefeld, M. Siebold, M. Schnepp, J. Hein, R. Sauerbrey, and M. Kaluza, "Alignment of a tiled-grating compressor in a high-power chirped-pulse amplification laser system," Appl. Opt. **46**(30), 7432-7435 (2007).

[6] Z. Li, S. Li, C. Wang, Y. Xu, F. Wu, Y. Li, and Y. Leng, "Stable and near Fourier-transform-limit 30fs pulse compression with a tiled grating compressor scheme," Opt. Express **23**(26), 33386-33395 (2015).

[7] C. Gaida, M. Gebhardt, F. Stutzki, C. Jauregui, J. Limpert, and A. Tünnermann, “Self-compression in a solid fiber to 24 MW peak power with few-cycle pulses at 2 um wavelength,” Opt. Lett. **40**(22), 5160–5163 (2015).

[8] D. A. Korobko, O. G. Okhotnikov, D. A. Stoliarov, A. A. Sysoliatin, and I. O. Zolotovskii, “Highly nonlinear dispersion increasing fiber for femtosecond pulse generation”, J. Light. Technol. **33**(17), 3643-3648 (2015).

[9] M. Gebhardt, C. Gaida, F. Stutzki, S. Hädrich, C. Jauregui, J. Limpert, and A. Tünnermann, " Nonlinear pulse compression to 43 W GW-class few-cycle pulses at 2 μm wavelength," Opt. Lett. **42**(20), 747-750 (2017).

[10] M. Gebhardt, C. Gaida, T. Heuermann, F. Stutzki, C. Jauregui, J. Antonio-Lopez, A. Schulzgen, R. Amezcua-Correa, J. Limpert, and A. Tünnermann, "Nonlinear pulse compression to 43 W GW-class few-cycle pulses at 2 μm wavelength," Opt. Lett. **42**(20), 4179-4182 (2017).

[11] O. P. Kulkarni, V. V. Alexander, M. Kumar, M. J. Freeman, M. N. Islam, F. L. Terry, Jr., M. Neelakandan, and A. Chan, “Supercontinuum generation from ~1.9 to 4.5 μm in ZBLAN fiber with high average power generation beyond 3.8 μm using a thulium-doped fiber amplifier,” J. Opt. Soc. Am. B **28**(10), 2486–2498 (2011).

[12] A. M. Heidt, J. H. V. Price, C. Baskiotis, J. S. Feehan, Z. Li, S. U. Alam, and D. J. Richardson, “Mid-infrared ZBLAN fiber supercontinuum source using picosecond diode-pumping at 2 μm,” Opt. Express **21**(20), 24281– 24287 (2013).

[13] R. Thapa, D. Rhonehouse, D. Nguyen, K. Wiersma, C. Smith, J. Zong, and A. Chavez-Pirson, “Mid-IR supercontinuum generation in ultra-low loss, dispersion-zero shifted tellurite glass fiber with extended coverage beyond 4.5 μm,” Proc. SPIE 8898, 889808 (2013).

[14] J. Swiderski, M. Michalska, C. Kieleck, M. Eichhorn, and G. Maze, “High power supercontinuum generation in fluoride fibers pumped by 2μm pulses,” IEEE Photonics Technol. Lett. **26**(2), 150–153 (2014).

[15] F. Théberge, J.-F. Daigle, D. Vincent, P. Mathieu, J. Fortin, B. E. Schmidt, N. Thiré,

and F. Légaré, “Midinfrared supercontinuum generation in fluoroindate fiber,” Opt. Lett. **38**(22), 4683–4685 (2013).

[16] P. Domachuk, N. A. Wolchover, M. Cronin-Golomb, A. Wang, A. K. George, C. M. B. Cordeiro, J. C. Knight, and F. G. Omenetto, “Over 4000 nm bandwidth of mid-IR supercontinuum generation in sub-centimeter segments of highly nonlinear tellurite PCFs,” Opt. Express **16**(10), 7161–7168 (2008).

[17] U. Møller, Y. Yu, I. Kubat, C. R. Petersen, X. Gai, L. Brilland, D. Méchin, C. Caillaud, J. Troles, B. LutherDavies, and O. Bang, “Multi-milliwatt mid-infrared supercontinuum generation in a suspended core chalcogenide fiber,” Opt. Express **23**(3), 3282–3291 (2015).

[18] O. Mouawad, J. Picot-Clémente, F. Amrani, C. Strutynski, J. Fatome, B. Kibler, F. Désévédavy, G. Gadret, J.-C. Jules, D. Deng, Y. Ohishi, and F. Smektala, “Multioctave midinfrared supercontinuum generation in suspendedcore chalcogenide fibers,” Opt. Lett. **39**(9), 2684–2687 (2014).

List of Publications

Journals

- **Z. Ren**, F. B. Slimen, J. Lousteau, N. White, Y. Jung, Xu, J. H. V. Price, D. J. Richardson and F. Poletti, "Compact chirped- pulse amplification systems based on highly Tm^{3+} doped germanate fiber," ***Optics Letters***, 46, 3013-3016 (2021).
- **Z. Ren**, Q. Fu, L. Xu, J. H. V. Price, S. Alam, and D. J. Richardson, "Compact, high repetition rate, 4.2 MW peak power, 1925 nm, thulium-doped fiber chirped-pulse amplification system with dissipative soliton seed laser," ***Optics Express***, 27 (25), 36741-36749 (2019).
- W. Cao, S. Liu, C. Littlejohns, D. Thomson, M. Nedeljkovic, W. Zhang, K. Li, M. Banakar, Y. Tran, X. Yan, H. Du, **Z. Ren**, F. Gardes, G. Reed, and G. Mashanovich, "High-speed silicon Michelson interferometer modulator and streamlined IMDD PAM-4 transmission of Mach-Zehnder modulators for the 2 μm wavelength band," ***Optics Express,*** 29 (10), 14438-14451 (2021).

Conferences

- **Z.Ren**, *et al.*, "Robust, high peak power, thulium-doped fiber chirped-pulse amplification system using a dissipative soliton seed laser," in ***Conference on Lasers and Electro-Optics,*** San Jose, pp. STh1E.3, 2019.
- D. Kong, **Z. Ren** et. al, "100 Gbit/s PAM-16 Transmission in the 2-μm Band over a 1.15-km Hollow-Core Fiber," in ***Optical Fiber Communication***, accepted, 2021.
- F. Ben Slimen, **Z. Ren** et. al, "Highly-Tm3+ doped Hexagonal Clad Germanate Fiber and associated CPA system for 2 μm Pulsed Fiber Lasers and Amplifiers," in ***Advanced Photonics Congress,*** pp. 3409383, 2020.
- F. Ben Slimen, **Z. Ren** et. al, "Highly Tm3+ doped germanate glass and associated double clad fiber for 2 um lasers and amplifiers," in ***Proc. SPIE 11206,*** 1120609-1, 2019.
- A.Karvounis, **Z.Ren** et.al, "Nano-opto-mechanical Metamaterial Q-switches infrared fibre laser," in ***Conference on Lasers and Electro-Optics*/Europe**, pp. EH-5.1, 2019.
- D. Kong, Y. Liu, **Z. Ren** et. al, "2-μm-band Coherent Transmission of Nyquist-WDM 16-QAM Signal by On-chip Spectral Translation," in ***Post deadline at Conference on Lasers and Electro-Optics***, accepted, 2021.
- Y. Liu, D. Kong, **Z. Ren** et. al, "Generation and heterodyne detection of a 2-μm-band 16-QAM signal based on inter-band wavelength conversion," in ***Conference on Lasers and Electro-Optics***, pp. SF2L.1, 2020.
- D. Kong, Y. Liu, **Z. Ren** et. al, "Generation and Coherent Detection of 2-μm-band WDM-QPSK Signals by On-chip Spectral Translation," in ***Optical Fiber Communication***, pp. M1I.4, 2020.
- D. Lin, D. Xu, J. Xu, Y. Feng, **Z. Ren** et. al, "Generation of ~625nJ Pulses from a Mamyshev Oscillator with a few-mode LMA Yb-doped Fiber," in ***Conference on Lasers and Electro-Optics/Europe-EQEC***, accepted, 2021.

◆ W. Cao, M. Nedeljkovic, S. Liu, C. Littlejohns, D. Thomson, F. Gardes, **Z. Ren** et. al, “25 Gbit/s silicon based modulators for the 2 μm wavelength band,” in ***Optical Fiber Communication Conference***, pp. M2B.4. 2020.